



## Satellite gravimetry: Methods, products, applications, and future trends

Mehdi Eshagh<sup>a,\*</sup>, Shuanggen Jin<sup>b,c</sup>, Roland Pail<sup>d</sup>, Riccardo Barzaghi<sup>e</sup>, Dimitrios Tsoulis<sup>f</sup>, Robert Tenzer<sup>g</sup>, Pavel Novák<sup>a</sup>

<sup>a</sup> University of West Bohemia, 30100 Pilsen, Czech Republic

<sup>b</sup> School of Surveying and Land Information Engineering, Henan Polytechnic University, Jiaozuo 454003, China

<sup>c</sup> Shanghai Astronomical Observatory, Chinese Academy of Sciences, Shanghai 200030, China

<sup>d</sup> Technical University of Munich, Munich, Germany

<sup>e</sup> Politecnico di Milano, Milan, Italy

<sup>f</sup> Aristotle University of Thessaloniki, Thessaloniki, Greece

<sup>g</sup> Hong Kong Polytechnic University, Hong Kong, China

### ARTICLE INFO

#### Keywords:

Gravitational field  
Geodesy  
Satellite gravimetry  
Temporal variations

### ABSTRACT

The gravitational field of the Earth reflects Earth's surface mass redistribution and its inner structure and dynamics. Satellite gravimetry techniques have been used to observe the Earth's external gravitational field and its temporal variations on a global scale. The global gravitational models from satellite gravimetry, typically in terms of spherical harmonic coefficients, are crucial in geodetic, geodynamic, geophysical, hydrological, glaciological, oceanographic, and many other geoscience applications. In this paper, we provide a comprehensive overview of theoretical definitions describing relationships between the spherical harmonic coefficients and different satellite gravimetry observables such as orbital perturbations in terms of satellite positions, velocities, and accelerations; satellite-to-satellite range rates; and gravitational gradients. Products and applications of the Earth's static global gravitational models are presented and discussed in the context of determination of the gravimetric geoid and physical heights, gravimetric and isostatic crustal thickness, bathymetric depths, glacier bedrock relief, sediment thickness, geostrophic and eddy currents, Earth's inertia tensor and dipole, precession and nutation parameters of the Earth's rotation, and prediction of the satellite orbital geometry. Furthermore, applications and advances of the Earth's time-variable gravitational models for monitoring large earthquakes, hydrological mass transport, Earth's rotation parameters, and vertical crustal motions (due to the glacial isostatic adjustment and other phenomena) are presented. Finally, future trends and prospects in the satellite gravimetry are discussed.

### 1. Introduction

The Earth's gravitational field provides insights into its surface mass transport or inner structure, while its spatio-temporal variations reveal planet's dynamic processes. Gravimetry, an experimental method providing data about this potential field, utilises terrestrial, airborne, shipborne, and satellite sensors. The former three primarily capture local gravity data. In contrast, satellite gravimetry delivers almost globally distributed data. Nevertheless, practical constraints, stemming from various factors, limit the accuracy, and temporal and spatial resolutions of data provided by satellite sensors in mapping the Earth's gravitational field. Additionally, satellite orbital perturbations and measurements do not directly yield gravitational field parameters,

necessitating their complex processing. This study provides a comprehensive overview of the mathematical foundations of satellite gravimetry, elucidating the relationships between various satellite observables and the spherical harmonic coefficients describing the Earth's external gravitational field.

The Keplerian law states that satellites orbit the Earth along ellipses with one epicentre being the centre of mass of the Earth. Newton's law of gravitation, generalising the description of motion (and Kepler's laws), can be used. Several methods exist for modelling the Earth's gravitational field based on orbital perturbations. Kaula (1966) introduced a gravitational potential representation in terms of orbital elements, subsequently applied for the Earth's gravity field modelling, as demonstrated by Visser (1992). Rosborough (1986) proposed an

\* Corresponding author.

E-mail address: [eshagh@ntis.zcu.cz](mailto:eshagh@ntis.zcu.cz) (M. Eshagh).

<https://doi.org/10.1016/j.earscirev.2024.104783>

Received 28 October 2023; Received in revised form 2 April 2024; Accepted 17 April 2024

Available online 22 April 2024

0012-8252/© 2024 Elsevier B.V. All rights reserved.

alternative approach linking orbital variations to perturbations in satellite's along-track, cross-track, and radial directions. Gaussian equations (Moulton, 1914) have also been employed to describe the gravitational field's variations in these directions. Schrama (1986) established functional relationships that connected orbital perturbations with satellite's acceleration vector. These methods can be used to analyse satellite orbital perturbations to recover the gravitational field.

The velocity (Jekeli, 1999) and acceleration (Ditmar and van der Sluijs Eck, 2004; Guo et al., 2017) vectors of satellites have also been utilised for this purpose. Orbital analyses of missions like the Challenging Minisatellite Payload (CHAMP) (Reigber et al., 2002) have contributed to the gravitational field modelling. Theoretical foundations of modelling the Earth's gravitational field and its temporal variations using inter-satellite range rates of two satellites along similar orbits were introduced by Schwarz (1970), Kryński and Schwarz (1977), Fischell and Pisacane (1978), Kryński (1979). Rummel (1980) developed a corresponding functional model for line-of-sight measurements, which has been practically applied to process data from missions like the Gravity field and Climate Experiment (GRACE) (Tapley et al., 2004) and the GRACE Follow-On (GRACE-FO) mission (Kornfeld et al., 2019). Gravity gradiometry, measuring second-order derivatives of the gravitational potential using differential accelerometry (Reed, 1973; Kryński and Schwarz, 1977; Koop, 1993), provided the most detailed information about the Earth's external gravitational field to date, primarily through data collected by the Gravity field and steady-state Ocean Circulation Explorer (GOCE) mission (Drinkwater et al., 2003).

In their comprehensive review, Flechtner et al. (2021) chronicle the evolution of satellite gravimetry. Initially reliant on analysis of satellites' orbital perturbations, this approach faced challenges due to disparities in observatory distribution, measurement inaccuracies, and model limitations in creating global Earth gravitational models (EGMs). A substantial progress was achieved in the late 20th century with the introduction of gravity-dedicated satellite missions equipped with specialised sensors. The Flechtner et al. (2021) review explores the historical context, mission objectives, and measurement techniques of key satellite missions launched after 2000, such as CHAMP, GRACE, and GOCE. It also discusses mission outcomes, highlights unique aspects of the GRACE Follow-On Mission (launched in 2018), and outlines plans for future gravity field missions. This underscores the ongoing significance of satellite gravimetry in enhancing our understanding of the Earth's gravitational field and its applications in geosciences.

Satellite geodesy, the scientific discipline born with the launch of the first artificial satellite in 1957, has revolutionised our comprehension of the Earth's geometry, orientation in space and rotation, and gravitational field (Flechtner et al., 2021). Prior to this era, geodesy, influenced by the work of Kepler, Newton, and Huygens in the 17th century, was confined only to astronomical, terrestrial or airborne measurements. However, satellites have shattered these limitations, enabling consistent and comprehensive global observations of the Earth's geometry and physical properties. Among its primary objectives, satellite geodesy seeks to delineate spatial structures and track temporal changes in the Earth's gravitational field. This knowledge serves as a crucial link to investigate the physics of the Earth's interior, comprehend oceanic circulation patterns and dynamics, and, more recently, delve into complexities of climate change factors. Satellite gravimetry has emerged as a cornerstone in the study of climate change, monitoring phenomena such as the ice mass loss in Greenland and Antarctica, sea-level fluctuations, and shifts in the global water cycle.

The global representation of the external Earth's gravitational field often relies on spherical harmonic coefficients, leading to the creation of Earth's Gravitational Models (EGMs) (Flechtner et al., 2021). The EGMs come in two main forms: static and time-variable, each serving a multitude of geodetic and geophysical purposes. Static EGMs find

application in diverse fields, from determining physical heights (Heiskanen and Moritz, 1967; Vermeer, 2020) and geoid modelling (Sjöberg, 1984; Vaníček and Martinec, 1994; Barzaghi, 2016) to predicting satellite orbits (Somodi and Földvay, 2011) and characterising lithospheric stress (Runcorn, 1967), Earth's inertia tensor (Marchenkov and Schwintzer, 2003), and the Earth's dipole moment (Vermeer, 2020), including the precession-nutation angles (Bourda and Capitaine, 2004), as well as determining sub-lithospheric shear stresses (Runcorn, 1967) and lithospheric stress tensor parameters (Liu, 1983).

Time-variable EGMs have played a critical role in monitoring post-seismic deformations, pinpointing earthquake focal points (Fatolazadeh et al., 2019), modelling hydrological mass transport (Wahr et al., 1998), assessing variations in sub-lithospheric and lithospheric stresses (Eshagh et al., 2020a), understanding post-glacial rebound, estimating upper mantle viscosity (Sjöberg and Bagherbandi, 2013), and analysing variations in the Earth's pole excitation and length-of-day (Jin et al., 2011, 2012; Chen et al., 2016a, 2016b). These spatio-temporal datasets are instrumental in advancing our comprehension of dynamic Earth processes and phenomena (Flechtner et al., 2021).

In this comprehensive review article, our primary objective is to outline the intricate mathematical foundations that underpin satellite gravimetry techniques employed in the precise recovery of Earth's gravitational field. Unlike the insightful review by Flechtner et al. (2021), which provided a broader perspective on the evolution and applications of satellite gravimetry, our focus here is to offer a deeper insight into the mathematical intricacies that drive this field forward and application advances in geoscience and geodynamics.

Firstly, we explore the fundamental mathematical principles that govern satellite gravimetry. This will encompass a detailed examination of the various mathematical models, equations, and methodologies utilised to extract invaluable data about the Earth's gravitational field provided by satellite observations. Our aim is to provide geophysicists and geodesists with a comprehensive understanding of mathematical underpinnings that empower satellite gravimetry as a vital tool in the realm of geosciences.

Moving beyond the mathematical fundamentals, the second part of this paper presents a panoramic view of the diverse applications that stem from satellite gravimetry products. We elucidate how these products find utility in an array of fields, including geodesy, geophysics, oceanography, and climate science. By showcasing the versatility and real-world significance of satellite gravimetry data, we aspire to highlight its paramount role in advancing our knowledge of the Earth's dynamic processes and its contribution to scientific research.

Finally, we pay our attention to the horizon of satellite gravimetry, addressing future challenges that lie ahead. The rapid advancements in technology and evolving demands of scientific inquiry continue to shape this field. We explore emerging trends, innovative methodologies, and unresolved questions that will steer the course of satellite gravimetry in the coming years. Our discussion sheds light on exciting prospects and uncharted territories that await researchers in the pursuit of a deeper understanding of the Earth's gravitational field and its implications for our planet's dynamic behaviours.

## 2. Theory and methods of satellite gravimetry

In this section, we provide a concise overview of techniques employed to derive Earth's gravitational field data from satellite observations. Our emphasis is placed on elucidating mathematical connections between the observables and the spherical harmonic coefficients that serve as the mathematical foundation for representing the Earth's external global gravitational field.

## 2.1. Satellite orbits

Variations in orbital parameters can be considered as satellite gravimetry observations. Methods of linking spatio-temporal geopotential variations to orbital perturbations were presented by Kaula (1966). The determination of the gravitational potential from measured orbital parameters represents an inverse problem in satellite gravimetry. In this subsection, the relationship between orbital perturbations and the Earth's gravitational potential is given.

Let us begin with the definition of the gravitational potential  $V$  in the following form:

$$V = V_0 + V_1 + V^p \quad (1a)$$

where  $V_0$  and  $V_1$  denote the zero- and first-degree terms in its spherical harmonic expansion, respectively. The zero-degree term  $V_0$  represents the gravitational potential of the homogenous spherical Earth, while the first-degree term  $V_1$  describes 3-D deviation of the origin of the terrestrial coordinate system (TRF) from its centre of mass. When a geocentric coordinate system is used,  $V_1$  becomes zero. The last term  $V^p$  on the right-hand side of Eq. (1a) is called the perturbing potential that represents deviations of the Earth's gravitational field from the central field  $V_0$ .

If only  $V_0$  is used for the orbit computation, the result is the Keplerian orbit, i.e., an orbit without any perturbations. However, the real orbit of a satellite is not Keplerian, as the satellite is affected by different types of gravitational and non-gravitational forces, most notably by the Earth's polar flattening and mass density heterogeneities inside the Earth. If mathematical models of the known gravitational and non-gravitational forces exist, their effects can be computed, and the satellite's orbit can be predicted in time by solving the equation of motion (Newton's law of gravitation).

Some satellites have the possibility of removing (or significantly reducing) non-gravitational and external gravitational effects practically. After removing these perturbations, an orbit, influenced solely by the static Earth's gravitational field, is obtained and by subtracting the Keplerian orbit, generated from  $V_0$ , the perturbed orbit is derived, which can be mapped to the perturbing potential  $V^p$ . It can further be expanded into the spherical harmonic series

$$V^p(r, \theta, \lambda) = \sum_{n=2}^{\infty} \left(\frac{R}{r}\right)^{n+1} \sum_{m=-n}^n v_{nm} Y_{nm}(\theta, \lambda) \quad (1b)$$

where  $Y_{nm}(\theta, \lambda)$  are the fully-normalised spherical harmonic functions of degree  $n$  and order  $m$  with arguments of the spherical co-latitude  $\theta$  and spherical longitude  $\lambda$ ;  $R$  is the Earth's mean radius;  $r$  is the geocentric distance of a point outside the Earth, and  $v_{nm}$  are spherical harmonic coefficients describing the perturbing potential.

The static perturbing potential  $V^p$  in Eq. (1b) is only a function of the geocentric position, which can be determined, for example, using global navigation satellite systems (GNSS), such as GPS NAVSTAR, GLONASS, Galileo or BeiDou.

Kaula (1966) presented the perturbing potential  $V^p$  in terms of orbital elements by the following harmonic series

$$V^p = \frac{1}{R} \sum_{n=2}^{\infty} \sum_{m=-n}^n \sum_{p=0}^n \sum_{q=-\infty}^{\infty} \left(\frac{R}{r}\right)^{n+1} F_{nmp}(i) G_{npq}(e) s'_{nmpq}(\bar{\psi}) \quad (1c)$$

where  $F_{nmp}(i)$  and  $G_{npq}(e)$  are the inclination and the eccentricity functions,  $p$  and  $q$  the harmonic components (Douglas and Palmiter, 1967), see, e.g., (Kaula, 1966; or Seeber, 2003, p. 90–92) for their formulae. The parameter  $s'_{nmpq}(\bar{\psi})$  in Eq. (1c) reads

$$s'_{nmpq}(\bar{\psi}) = \frac{ds_{nmpq}(\bar{\psi})}{d\bar{\psi}}, \quad (1d)$$

where

$$s_{nmpq}(\bar{\psi}) = \begin{cases} v_{nm} \begin{cases} \sin \bar{\psi} & m > 0 \\ -\cos \bar{\psi} & m \leq 0 \end{cases} & n - m \text{ even} \\ v_{n,-m} \begin{cases} -\sin \bar{\psi} & m > 0 \\ -\cos \bar{\psi} & m \leq 0 \end{cases} & n - m \text{ odd} \end{cases} \quad (1e)$$

$$\bar{\psi} = (n - 2p)(\omega + \bar{M}) + m(\Omega - \Theta) + q\bar{M} \quad (1f)$$

$\Theta$  denotes the Greenwich apparent sidereal time (GAST),  $e$  is the first numerical eccentricity of the Keplerian ellipse,  $\bar{M}$  is the (time-dependent) mean anomaly,  $\omega$  is the argument of perigee,  $\Omega$  is the right ascension of the ascending node, and  $i$  is the orbit inclination.

By using Eq. (1c), the perturbing potential  $V^p$  can be derived from the orbital elements as well as its harmonic coefficients  $v_{nm}$ . It is important to note that the goal is to estimate the harmonic coefficients  $v_{nm}$  instead of  $V^p$ . Moreover, values of  $V^p$  cannot be directly measured.

Lagrange's planetary equations define a relationship between the temporal variations of the Keplerian orbital elements and the temporal derivatives of the perturbing potential  $V^p$ ; see Kaula (1966). The integration of these equations in time and their linearisation yield (Visser, 1992; p.14 and 15)

$$\Delta a_{nmpq} = \frac{2\bar{n}}{R\bar{\psi}} \left(\frac{R}{a}\right)^{n+1} F_{nmp} G_{npq} (n - 2p + q) s'_{nmpq}(\bar{\psi}) \quad (2a)$$

$$\Delta e_{nmpq} = \frac{\bar{n}}{\bar{\psi}} \frac{\sqrt{1-e^2}}{e} \left(\frac{R}{a}\right)^n F_{nmp} G_{npq} [(n - 2p + q)\sqrt{1-e^2} - (n - 2p)] s'_{nmpq}(\bar{\psi}) \quad (2b)$$

$$\Delta \omega_{nmpq} = \frac{\bar{n}}{\bar{\psi}} \left(\frac{R}{a}\right)^n \left[ \frac{\sqrt{1-e^2}}{e} F_{nmp} G'_{npq} - \frac{\cot i F'_{nmp} G_{npq}}{\sqrt{1-e^2}} \right] s_{nmpq}(\bar{\psi}) \quad (2c)$$

$$\Delta i_{nmpq} = \frac{\bar{n}}{\bar{\psi} \sqrt{1-e^2} \sin i} \left(\frac{R}{a}\right)^n F_{nmp} G_{npq} [(n - 2p) \cos i - m] s'_{nmpq}(\bar{\psi}) \quad (2d)$$

$$\Delta \Omega_{nmpq} = \frac{\bar{n}}{\bar{\psi} \sqrt{1-e^2} \sin i} \left(\frac{R}{a}\right)^n F'_{nmp} G_{npq} s_{nmpq}(\bar{\psi}) \quad (2e)$$

$$\Delta \bar{M}_{nmpq} = \frac{\bar{n}}{\bar{\psi}} \left(\frac{R}{a}\right)^n F_{nmp} \left[ 2(n + 1) G_{npq} - \frac{\sqrt{1-e^2}}{e} G'_{npq} - 3G_{npq}(n - 2p + q) \frac{\bar{n}}{\bar{\psi}} \right] s_{nmpq}(\bar{\psi}) \quad (2f)$$

where  $G'_{npq} = dG_{npq}(e)/de$ ,  $G_{npq} = G_{npq}(e)$ ,  $F'_{nmp} = dF_{nmp}/di$ ,  $F_{nmp} = F_{nmp}(i)$ ,  $\bar{n}$  stands for the mean orbital motion, and  $a$  for the major semi-axis of the orbital ellipse.

The solutions in Eqs. (2a)-(2f) are valid only when the perturbations are independent. The approximation applied for deriving these equations is accurate enough to describe the Earth's gravitational potential (Seeber, 2003, p. 93). Summation parameters  $n$ ,  $m$ ,  $p$ , and  $q$  relate to the orbital perturbations and the unknown harmonic coefficients  $v_{nm}$  on the right-hand side of the equations. Consequently, a system of equations can be established for finding the solution for harmonic coefficients  $v_{nm}$  that are multiplied by the attenuation factor  $\left(\frac{R}{a}\right)^n$ , i.e.,  $v_{nm} \left(\frac{R}{a}\right)^n$ .

The mathematical models that describe linear changes in orbital elements, as shown in Eqs. (2a)-(2f), formulate a system of equations with unknowns in the functions  $S_{nmpq}$  and  $s'_{nmpq}$ . The number of unknowns varies depending on the maximum degree of the harmonic series expansion. However, at any given point along the orbit, six equations

can be constructed, which are insufficient for solving for  $v_{nm}$ . Consequently, additional satellite revolutions around Earth are necessary to encompass the globe and determine the  $v_{nm}$  coefficients. Such systems of equations are often ill-conditioned, necessitating the use of regularisation to achieve a smooth solution.

Eqs. (2a)-(2f) have singularities in case of a circular orbit. The parameter  $\dot{\psi}$  is zero for  $n = 2p$ ,  $m = 0$ , and  $q = 0$ . In addition, if these equations are solved for  $s_{nmpq}$  or  $s'_{nmpq}$ ,  $G_{npq}$  and/or  $G'_{npq}$  will be in the denominators of the results, and when  $e = 0$ , they become zero. Even a small value of  $\dot{\psi}$  amplifies the velocity of orbital elements, which means

$$\ddot{\mathbf{r}}_{\text{TRF}} = \frac{1}{r} \begin{bmatrix} \sum_{n=0}^{\infty} \left(\frac{R}{r}\right)^{n+1} \sum_{m=-n}^n v_{nm} \left[ -\cos\theta \cos\lambda \frac{\partial}{\partial\theta} - \sin\lambda \frac{\partial}{\sin\theta \partial\lambda} - (n+1)\cos\lambda \sin\theta \right] Y_{nm}(\theta\lambda) \\ \sum_{n=0}^{\infty} \left(\frac{R}{r}\right)^{n+1} \sum_{m=-n}^n v_{nm} \left[ -\cos\theta \sin\lambda \frac{\partial}{\partial\theta} + \cos\lambda \frac{\partial}{\sin\theta \partial\lambda} - (n+1)\sin\lambda \sin\theta \right] Y_{nm}(\theta\lambda) \\ \sum_{n=0}^{\infty} \left(\frac{R}{r}\right)^{n+1} \sum_{m=-n}^n v_{nm} \left[ \sin\theta \frac{\partial}{\partial\theta} - (n+1)\cos\theta \right] Y_{nm}(\theta\lambda) \end{bmatrix} \cdot / \quad (3b)$$

that the orbit is in resonance between the mean motion of a satellite and the Earth's rotation, see, e.g.,  $v_{nm}$  (Klokočnik et al., 2013).

## 2.2. Satellite acceleration, velocity and gravity gradient

We explore how changes in the orbital elements of a satellite can be analysed to recover the Earth's gravity field. These elements can also be derived from the satellite's position and velocity vectors. Moreover, velocity and acceleration vectors, calculated from the satellite's position, can be employed in gravitational field modelling. The acceleration vector represents the first-order gradient of the Earth's gravitational potential. Meanwhile, the second-order gradients are instrumental in high resolution and local gravitational field modelling. In the subsequent sections, we elucidate the principles underlying the use of these observables for gravitational field modelling.

### 2.2.1. Satellite acceleration

Geocentric coordinates of a satellite can be estimated using GNSS. However, the TRF coordinates cannot directly be connected to the harmonic coefficients  $v_{nm}$ . A method of solving this problem is to estimate the geopotential perturbations in terms of rates of orbital elements and to apply the Lagrangian or Gaussian equations for solving  $v_{nm}$ . Alternatively, they can be solved by estimating the first- and second-order time derivatives of the along-, cross-, and radial-track perturbations, and by applying Hill's equations. The acceleration vector of a satellite can then be estimated from these coordinates. Ditmar and van der Sluijs Eck (2004) and Guo et al. (2017) developed the idea of determining orbits from GNSS phase measurements. They assumed that the position vector of a satellite  $\mathbf{r}(t)$  at the epoch  $t$  is measured with a sampling interval  $\Delta t$ , and estimated the acceleration vector  $\ddot{\mathbf{r}}(t)$  of the satellite using the following expression, see (Guo et al., 2017)

$$\ddot{\mathbf{r}}(t) = \frac{\mathbf{r}(t + \Delta t) - 2\mathbf{r}(t) + \mathbf{r}(t - \Delta t)}{(\Delta t)^2} \quad (3a)$$

The expression in Eq. (3a) is a simple three-point numerical differentiation scheme for computing the acceleration vector of a satellite from its orbit. Ditmar and van der Sluijs Eck (2004) mentioned the following points in this approach: (i) noise in the orbit-derived accelerations strongly depends on the sampling frequency; therefore, the key element of the proposed technique is frequency-dependent data weighting. (ii) Satellite position vectors must be differentiated in a

pseudo-inertial coordinate frame (like CRF) to provide absolute accelerations without involving the centrifugal and Coriolis forces. (iii) The total satellite acceleration vector derived from a satellite orbit should be converted into residual accelerations by subtracting the contribution of the reference gravitational field. The estimated accelerations in the Celestial Reference Frame (CRF) should be rotated to the Terrestrial Reference Frame (TRF).

The mathematical models of the satellite acceleration vector in TRF represented by the spherical harmonic series read, e.g., (Eshagh, 2020),

All parameters on the right-hand side of Eq. (3b) are known except for the harmonic coefficients  $v_{nm}$ . A comprehensive system of equations emerges as satellite orbits span the globe, which is essential for determining the harmonic coefficients  $v_{nm}$ . Similarly, this system of equations is often ill-conditioned, necessitating the application of a regularisation scheme or constraining the solution with some a priori information to solve it effectively.

### 2.2.2. Satellite velocity

Bjerhammar (1968) presented the energy integral method for recovering the gravitational potential from the kinetic energy of a satellite. In this approach, the satellite velocity vector is used to determine the kinetic energy of a satellite and then the gravitational potential according to the Lagrangian function. Jekeli (1999) presented the following equation for the gravitational field recovery from the satellite velocity vector:

$$\begin{aligned} & \frac{1}{2} \left( \dot{x}_{\text{TRF}}^2 + \dot{y}_{\text{TRF}}^2 + \dot{z}_{\text{TRF}}^2 \right) - \frac{1}{2} \omega_e^2 (x_{\text{TRF}}^2 + y_{\text{TRF}}^2) - \int_0^t \mathbf{a}_{\text{TRF}} \cdot \dot{\mathbf{r}}_{\text{TRF}} dt \\ & = - \sum_{n=0}^{\infty} \left(\frac{R}{r}\right)^{n+1} \sum_{m=-n}^n v_{nm} Y_{nm}(\theta, \lambda) + H, \end{aligned} \quad (3c)$$

Here  $H$  is the constant value, so-called Hamiltonian, in the case of no energy dissipation; the integral on the left-hand side is the energy dissipation of the system in the time interval of 0 to  $t$ ; and  $\mathbf{a}_{\text{TRF}}$  is the vector of the dissipative acceleration. Therefore,  $H$  can be considered as an extra unknown in addition to the harmonic coefficients  $v_{nm}$  in the system of the observation equations in Eq. (3c).

It should be stated that from the position and velocity vectors of a satellite only one equation can be formed for recovering the harmonic coefficients  $v_{nm}$ . Compared to the acceleration method and other methods presented so far, the energy-integral approach has a direct relation with the gravitational potential, not with its derivatives. Therefore, a smoother gravitational field model can be obtained by comparing to those obtained from gradients of the gravitational potential.

### 2.2.3. Satellite gravity gradiometry

The second-order gradients of the gravitational potential counterbalance the attenuation of the gravitational field due to the distance of the satellite sensors from the gravitating masses. They are measured by a gradiometer on the principle of differential accelerometry that contains

three pairs of accelerometers along three axes of a gradiometer reference frame, totalling six accelerometers. Spherical harmonic series of the gravitational gradients read, e.g., (Reed, 1973; Koop, 1993),

$$V_{zz} = \frac{1}{r^2} \sum_{n=0}^{\infty} (n+1)(n+2) \left(\frac{R}{r}\right)^{n+1} \sum_{m=-n}^n v_{nm} Y_{nm}(\theta, \lambda) \quad (4a)$$

$$V_{xx} = \frac{1}{r^2} \sum_{n=0}^{\infty} \left(\frac{R}{r}\right)^{n+1} \sum_{m=-n}^n v_{nm} \left[ - (n+1) Y_{nm}(\theta, \lambda) + \frac{\partial^2 Y_{nm}(\theta, \lambda)}{\partial \theta^2} \right] \quad (4b)$$

$$V_{yy} = \frac{1}{r^2} \sum_{n=0}^{\infty} \left(\frac{R}{r}\right)^{n+1} \sum_{m=-n}^n v_{nm} \left[ - (n+1) Y_{nm}(\theta, \lambda) + \frac{\partial Y_{nm}(\theta, \lambda)}{\tan \theta \partial \theta} + \frac{\partial^2 Y_{nm}(\theta, \lambda)}{\sin^2 \theta \partial \lambda^2} \right] \quad (4c)$$

$$V_{xy} = \frac{1}{r^2} \sum_{n=2}^{\infty} \left(\frac{R}{r}\right)^{n+1} \sum_{m=-n}^n v_{nm} \left( \frac{1}{\sin \theta} \frac{\partial^2 Y_{nm}(\theta, \lambda)}{\partial \theta \partial \lambda} - \frac{\cos \theta}{\sin^2 \theta} \frac{\partial Y_{nm}(\theta, \lambda)}{\partial \lambda} \right) \quad (4d)$$

$$V_{xz} = \frac{1}{r^2} \sum_{n=1}^{\infty} (n+2) \left(\frac{R}{r}\right)^{n+1} \sum_{m=-n}^n v_{nm} \frac{\partial Y_{nm}(\theta, \lambda)}{\partial \theta} \quad (4e)$$

$$V_{yz} = \frac{1}{r^2} \sum_{n=1}^{\infty} (n+2) \left(\frac{R}{r}\right)^{n+1} \sum_{m=-n}^n v_{nm} \frac{\partial Y_{nm}(\theta, \lambda)}{\sin \theta \partial \lambda} \quad (4f)$$

The harmonic series presented in Eqs. (4a)-(4f) constitutes observation equations with known parameters on the right-hand side, except for the harmonic coefficients  $v_{nm}$ . This setup allows the construction of a comprehensive system of linear equations, which can be solved for  $v_{nm}$  by employing GOCE gradient data. It is noteworthy that  $v_{nm}$  of higher degrees and orders compared to other observables can be inferred from satellite gravity gradients. Among the gradients,  $V_{zz}$  is distinguished by its strong signal and straightforward mathematical representation, owing to the more pronounced changes in the gravitational field in the radial direction. Furthermore, the resolution of the gradiometric boundary-value problems, through integral formulas, facilitates the calculation of  $v_{nm}$ . Specifically, gradients  $V_{xz}$  and  $V_{yz}$  are jointly utilised for one solution, while a combination of ( $V_{xx}$ - $V_{yy}$ ) and  $2V_{xy}$  are applied for another. As discussed by Martinec (2003), the gradient combinations are necessary in order to formulate integral-based solutions with easily determinable integral kernels. It is important to note that  $V_{xz}$  and  $V_{yz}$  lack zero-degree harmonics, implying that these degrees cannot be derived from these gradients. Similarly,  $V_{xy}$  excludes both zero- and first-degree harmonics.

### 2.3. Low-low satellite-to-satellite tracking data

Temporal changes of a distance between two satellites, or inter-satellite range rates, can also be measured. In the case where high orbiting satellites track low orbiters, the method is called high-low satellite-to-satellite tracking (hl SST). For example, low orbiters are precisely positioned by GNSS satellites. Subsequently, estimated kinematic orbits are applied for a gravitational field modelling based on the methods presented above. However, in the GRACE mission, the low-low SST (ll-SST) technique was used, i.e., the range rates between two low orbiters almost in the same orbit were measured precisely. The measured range rates are not constant owing to variations of the gravitational field (due to Earth's mass heterogeneities). Therefore, the range rates measured by ll-SST are particularly useful for detecting temporal gravitational field variations. In this section, we briefly explain the principle of recovery of the gravitational field variations through range rates measured by ll-SST; see Eshagh (2020) for more details.

#### 2.3.1. Satellite-to-satellite range rates

Fischell and Pisacane (1978) introduced the following relationship between the range rates of two orbiters and the Earth's gravitational

potential in the orbital frame:

$$v_0 \dot{\tilde{\rho}} = \sum_{n=0}^{\infty} \sum_{m=-n}^n v_{nm} \left[ \left(\frac{R}{r_2}\right)^{n+1} Y_{nm}(\theta_2, \lambda_2) - \left(\frac{R}{r_1}\right)^{n+1} Y_{nm}(\theta_1, \lambda_1) \right], \quad (5)$$

where  $\dot{\tilde{\rho}}$  stands for the inter-satellite range rate,  $v_0$  is the mean velocity of a satellite, and  $(r_2, \theta_2, \lambda_2)$  and  $(r_1, \theta_1, \lambda_1)$  are the spherical coordinates of the two satellites in TRF.

In Eq. (5), the only unknown parameters are the harmonic coefficients  $v_{nm}$ . Jekeli and Rapp (1980) and Sjöberg (1982) developed the idea of integrating the velocity difference over an extra-terrestrial sphere for computing the gravitational potential.

Eq. (5) demonstrates that in order to compute  $v_{nm}$ , the difference between two spherical harmonic functions at the distinct positions of the twin satellites is applied. Theoretically, differencing acts as an amplifying mathematical operator, which means that the higher degrees and orders of  $v_{nm}$  are more prominently sensed when using range rates, compared to using the velocity of a single satellite. This is based on the energy integral, which is directly related to the Earth's gravitational potential.

#### 2.3.2. Satellite-to-satellite line-of-sight

Rummel (1980) developed another method to relate the inter-satellite range rates with the gravitational potential. He defined the range rate as the norm of the position vector differences of the two satellites, and then took its second-order time derivative to obtain the acceleration, i.e.,

$$\ddot{\tilde{\rho}} = \Delta \ddot{\mathbf{r}}_{12} \mathbf{e}_{\text{LOS}} + \frac{(\Delta \dot{\mathbf{r}}_{12})^2 - \dot{\tilde{\rho}}^2}{\tilde{\rho}} \quad (6a)$$

where  $\mathbf{e}_{\text{LOS}} = \frac{\Delta \mathbf{r}_{12}}{\tilde{\rho}}$  is the line-of-sight (LOS) unit vector pointing from the satellite 1 to the satellite 2;  $\Delta \mathbf{r}_{12} = \mathbf{r}_2 - \mathbf{r}_1$  is the inter-satellite vector, and  $\tilde{\rho}$  is the distance between them;  $\Delta \dot{\mathbf{r}}_{12} = \dot{\mathbf{r}}_2 - \dot{\mathbf{r}}_1$  and  $\Delta \ddot{\mathbf{r}}_{12} = \ddot{\mathbf{r}}_2 - \ddot{\mathbf{r}}_1$  denote the inter-satellite velocity and acceleration vectors, respectively.

In Eq. (6a), the inter-satellite acceleration vector  $\Delta \ddot{\mathbf{r}}_{12}$  is directly related with the gravitational potential. Since the acceleration is proportional to the gradient of the gravitational potential (equation of motion), one can write in the inertial frame

$$\Delta \ddot{\mathbf{r}}_{12} = \nabla \Delta V_{12} \quad (6b)$$

where  $\Delta V_{12} = V(r_2, \theta_2, \lambda_2) - V(r_1, \theta_1, \lambda_1)$ ,  $\nabla$  is the gradient operator, and  $\Delta V_{12}$  is the gravitational potential difference at the positions of the two satellites.

According to Eqs. (1a), (6b) and (6a), the following formula connecting the LOS measurements with the harmonic coefficients  $v_{nm}$  can be formulated, see (Eshagh, 2020),

$$\begin{aligned} \ddot{\tilde{\rho}} - \frac{(\Delta \dot{\mathbf{r}}_{12})^2 - \dot{\tilde{\rho}}^2}{\tilde{\rho}} &= \sum_{n=0}^{\infty} \sum_{m=-n}^n v_{nm} \sum_{i=1}^2 \frac{(-1)^i}{r_i} \left(\frac{R}{r_i}\right)^{n+1} \left( - (n \right. \\ &\quad \left. + 1) Y_{nm}(\theta_i, \lambda_i) \mathbf{e}_r + \frac{\partial Y_{nm}(\theta_i, \lambda_i)}{\partial \theta_i} \mathbf{e}_{\theta_i} + \frac{\partial Y_{nm}(\theta_i, \lambda_i)}{\sin \theta_i \partial \lambda_i} \mathbf{e}_{\lambda_i} \right) \cdot \mathbf{e}_{\text{LOS}} \end{aligned} \quad (6c)$$

The expression in Eq. (6c) represents a mathematical model relating the harmonic coefficients of the gravitational potential and the range rates between the satellite pair. The left-hand side contains the range, its first- and second-order temporal derivatives, and the inter-satellite velocity vector.

By taking the gradient of the gravitational potential, the gravitational acceleration vector is obtained in the local north-oriented frame (LNOF) but the origin of this frame is defined by the satellite position. Therefore, when the gradient is applied to the potential at satellite 1, the result will be different for satellite 2. The inner product of the gradients projects them to the LOS direction between the two satellites, or in the

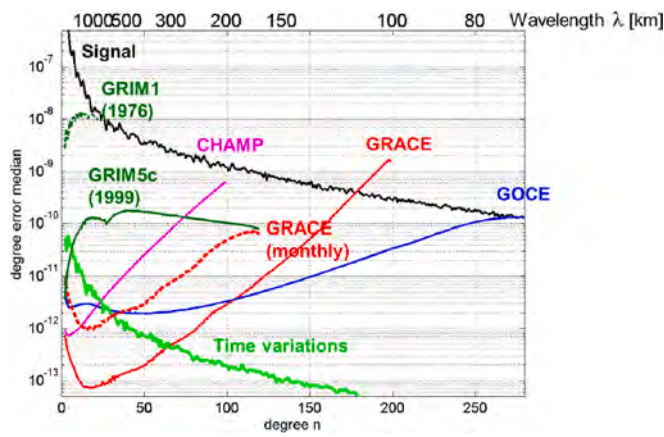


Fig. 1. Absolute gravitational signal and error estimates of different observation concepts as a function of the harmonic degree  $n$  (bottom axis) and spatial wavelength  $\lambda$  (top axis).

direction in which the range and range rate are measured.

Eq. (6c) illustrates that the mathematical model for LOS measurements is differential in nature. This means that the acceleration vector of each satellite is calculated and then subtracted from one another. Acceleration is more sensitive to the higher frequencies of the gravitational field, and this sensitivity is further amplified when its differential form is employed, making it even more sensitive to high frequencies. In essence, we can theoretically assert that LOS measurements are more sensitive to the high frequencies of the gravitational field compared to range rates. However, a significant challenge is the quality of range and range accelerations, which must be derived from satellite coordinates and range rates.

### 3. Products of satellite gravimetry

There are generally two types of products derived from satellite gravimetry: static and time-variable gravitational models. The static gravitational models represent long-term averages of the gravitational field determined from data of a satellite mission during its lifetime, while time-variable models are temporal snapshots derived from a few days up to one month of data.

#### 3.1. Static gravitational field products

So far, we showed that all types of satellite gravimetric measurements are in one way or another connected to the harmonic coefficients  $v_{nm}$  of the Earth's gravitational potential. A set of these coefficients is derived from a specific satellite gravimetry mission, data coverage and period, thus forming a particular EGM. Obviously, due to uncertainties, different spatial resolutions and attenuation of the satellite gravimetric data, the maximum degree and order differ between EGMs.

The performance of a gravity-dedicated satellite mission depends mainly on its observation technique and orbit design. Fig. 1 shows the performance of different satellite mission concepts in terms of degree error standard deviations, which describe the average noise amplitude for a certain degree  $n$  of the spherical harmonic series of the gravitational potential  $V$ . The harmonic degree  $n$  is linked to a spatial half-wavelength  $\kappa = 20,000 \text{ km}/n$ . As an example, a harmonic degree of  $n = 200$ , which was the pre-launch minimum target resolution for the GOCE mission, corresponds to a spatial half-wavelength of  $\kappa = 100 \text{ km}$ .

The black curve in Fig. 1 shows the amplitude of the gravitational field signal itself. In contrast, the coloured curves depict error estimates of EGMs derived from various observational concepts and corresponding data sources. The crossover point of a mission performance curve with the black curve indicates the harmonic degree at which the signal-to-

noise ratio is 1. Beyond this degree, the error of the EGM harmonic constituent is on average larger than the signal itself.

From the kinematic orbit information (hl-SST), only long-wavelength features of the gravitational field can be extracted. Although this observation type is not a direct functional of the gravitational potential, it can be interpreted as the disturbing acceleration of an orbiter; thus, it represents the first-order spatial derivative of the gravitational potential  $\partial V/\partial x_i$ . As an example of this measurement concept, the purple curve shows the performance of an EGM that was derived from CHAMP data (Reigber et al., 2002) over the period from 2000 to 2010.

The red solid curve shows the performance of the EGM containing only GRACE (Tapley et al., 2004) K-band inter-satellite range data over the period from 2002 to 2017, following the concept of hl-SST supported at very low spherical harmonic degrees by hl-SST. Compared to the CHAMP mission, the superior measurement principle of the GRACE single axis gradiometer results in a significantly improved accuracy of the low-to-medium harmonic coefficients as well as in a higher spatial resolution. This is explained by the fact that the GRACE concept can be interpreted as a measurement of acceleration differences along baselines of about 200 km. The excellent performance of GRACE in this frequency band makes this mission sensitive to small temporal variations of the Earth's gravitational field, which are four to five magnitudes smaller than the static signal (light green curve). These degree-wise amplitudes are compared with the average GRACE performance of a single month (red dashed curve), which is of course substantially lower than that of a multi-year solution (red solid curve).

The blue curve shows the performance of European Space Agency's (ESA's) dedicated gravity mission GOCE (Drinkwater et al., 2003) over the period 2009–2013. It is mainly based on the measurement technique of the satellite gravity gradiometry (SGG) supported by hl-SST at low degrees, because SGG alone is weak in this frequency band due to specific noise characteristics of the gravity gradiometer instrument. Measuring the acceleration differences at very short baselines of about half a meter, which approximate the second-order derivatives of the gravitational potential  $\partial^2 V/(\partial x_i \partial x_j)$ , enables further increasing the sensitivity of gradient data at shorter wavelengths. GOCE starts to become superior over GRACE approximately from harmonic degree  $n = 100$ .

In order to demonstrate the huge impact of gravity-dedicated satellite missions on our knowledge of the Earth's gravitational field, the dark green curves show power spectra of representative EGMs computed before the era of gravity-dedicated satellite missions. While GRIM1 (Balmino et al., 1976), the acronym for GRGS and Institute Munich, is based mostly on optical and laser observations to major geodetic satellites, GRIM5c (Gruber et al., 2000) also contains a global collection of ground data. Evidently, already the CHAMP solution outperforms all previous attempts to properly map the Earth's external gravitational field on a global scale by orders of magnitude at lower harmonic degrees.

Static EGMs with high precision and resolution are important for many applications. Satellite-only EGMs represent the Earth's gravitational field with largely uniform quality, but they are limited in terms of their spatial resolution. Obviously, their spatial resolution can be improved by combining them with satellite altimetry and terrestrial gravity observations (Rapp, 1998). Terrestrial gravimetric data contain all frequencies of the gravity field, but their global distribution is very irregular, so their long-wavelength contributions is limited. These data are generally provided in the form of mean values for compartments (blocks) formed by the grid of geographical coordinates with angular resolutions from  $5' \times 5'$  to  $1^\circ \times 1^\circ$ . Again, the spherical harmonic expansion is employed for representing the gravitational potential, where the maximum harmonic degree and order depend on the spatial resolution of the altimetric and terrestrial gravity data. Combined EGMs thus contain the following observations: the harmonic coefficients of a satellite-only EGM with the full error covariance matrix, mean free-air

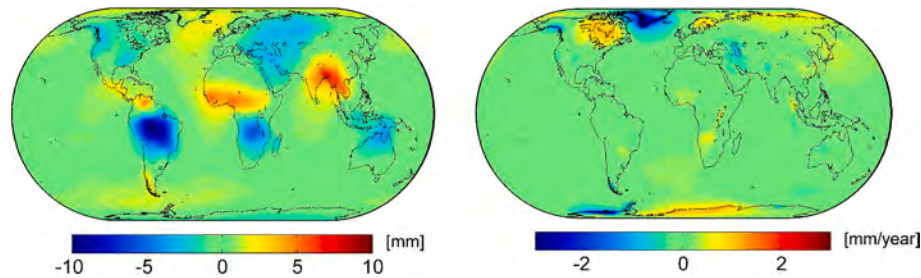


**Fig. 2.** Non-tidal temporal variations of the gravitational field from GRACE: a) geoid height deviations from a long-term mean in September, and b) their linear trends.

gravity anomalies from terrestrial gravimetry on land and sea, and mean geoid heights or gravity anomalies derived from satellite altimetry, both with an appropriate error model.

### 3.2. Temporal gravitational field products

The Earth's gravitational field is affected by temporal variations due to mass redistribution in the atmosphere, hydrosphere, cryosphere, and the solid Earth's surface, crust, mantle, and core. These processes take place at different spatial and temporal scales. The magnitude of the non-tidal gravity variations produced by mass redistributions are five to six orders of magnitude smaller than the static gravity field, cf. Fig. 1. Fig. 2a shows amplitudes of annual geoid height variations, particularly for September, averaged over fifteen years of the GRACE data. In many regions, the annual cycle is the dominant period. Evidently, the largest variations are observed over large-scale hydrological basins along the equator, such as the Amazon and Congo Basins. They are caused by seasonal changes in the global water cycle and related variations of the ground water level. GRACE mission has also been used for the estimation of height changes due to hydrological signals.

In addition to these periodic variations, long-term trends can be observed, see Fig. 2b. Large linear trends are caused by melting of ice sheets (e.g., in Greenland and Antarctica), glacial isostatic adjustment (e.g., in Fennoscandia, Northern Canada), long-term trends in the water cycle (e.g., droughts or ground water depletion partly caused by human activities such as irrigation), and the mass-related component of sea level changes. Minor contributions result from slow motions of the Earth's core and mantle convection. Instantaneous gravity variations are caused by mass changes related to volcanic activities and large earthquakes.

Temporal gravitational field products are mainly derived from the II-SST data as provided by the GRACE and GRACE-FO missions, because this data type is sensitive to the low-to-medium degrees of the harmonic spectrum where the largest gravitational variations occur, see Fig. 1. In contrast, the sensitivity of the GOCE gradient data to temporal variations of the gravitational field is rather low (Heller et al., 2020).

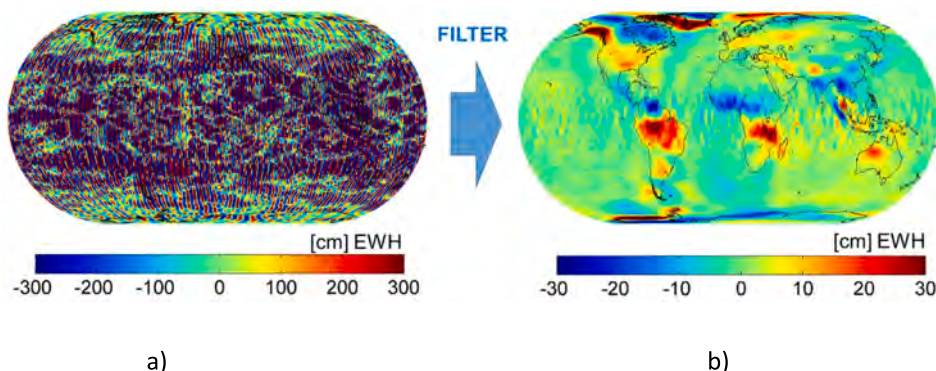


**Fig. 3.** a) Raw temporal gravity field solution in terms of equivalent water height (EWH) [cm], b) after application of a decorrelation filter.

Temporal EGMs derived from the single-pair in-line tracking missions GRACE and GRACE-FO are hampered by temporal aliasing effects. Due to limited temporal resolutions of these missions, high-frequency mass variations cannot be captured by the satellite data as they alias into the solution. Therefore, in order to reduce high-frequency gravitational variations related to atmospheric and oceanic mass variations, the so-called de-aliasing models derived from geophysical background models must be applied. However, the background models remain the biggest error contributors to temporal EGMs, exceeding by far sensor errors (Flechtner et al., 2016). Fig. 2a shows a “raw” temporal gravitational solution derived from GRACE data. North-South stripes are caused by the anisotropic error behaviour of along-track inter-satellite ranges in connection with temporal aliasing. Therefore, a-posteriori filters must be applied to reduce the striping noise and to reveal the temporal gravitational signal, see Fig. 3b, at the cost of removing also the higher-frequency component of the signal itself.

## 4. Applications

In Section 2, we summarised the recovery of Earth's gravitational field from different types of satellite gravimetry data. The products of satellite gravimetry were classified in Section 3 as static and time-variable EGMs. The aim of this section is to provide examples how these EGMs are used in selected geodetic, geophysical, glaciological, and oceanographic applications.

### 4.1. Applications of static EGMs

As already stated, static EGMs reflect the Earth's inner structure, which is not fully known. Therefore, different assumptions are made to extract the desired information from the gravitational field. Here, we demonstrate the use of static EGMs to determine the crustal structure, elastic thickness and rigidity, ice thickness, bathymetric depths, sediment basement morphology, and the lithospheric and sub-lithospheric stresses due to mantle convection.

#### 4.1.1. Geoid modelling

The geoid is the reference equipotential surface of the Earth's gravity field that best approximates the mean sea level. It continues under continents, where it is used to define the height reference surface for physical heights. The geoid should be known accurately to represent a reliable reference for physical heights. The knowledge of the precise geoid allows to replace lengthy and costly estimation of physical heights through spirit levelling by GNSS positioning. However, to achieve this goal, good knowledge of the Earth's gravity field, theoretical and numerical skills in geoid modelling, and precise data handling in all frequency bands are required.

Different approaches have been developed and applied for a gravimetric geoid modelling. All of them combine terrestrial/airborne gravity data, which are relatively sensitive to all frequencies but geographically limited, with EGMs providing low frequencies (long wavelengths) of the geoid. Thus, terrestrial gravity data are used to recover high frequencies of the geoid undulations and the EGMs for the low frequencies. In all modelling methods, computations of the effects of topographic and atmospheric masses, downward continuation of surface gravity data to sea level, and conversion of gravity data and EGMs to geoid/co-geoid must be performed. Geoid modelling methods primarily deal with the mathematical and numerical handling of these processes.

There is a variety of geoid modelling methods. Only a short overview of methods, that have been established in the literature and are used for routine applications, is provided. Fundamental means of classification of different methods is the adopted reference surface. Stokes's solution of the geoid height related to the reference ellipsoid requires gravity to be known on the geoid. Methods based on Molodensky's theory refer to the telluroid (i.e., the surface where the normal gravity potential equal the actual gravity potential on the Earth's surface along one plumbline) and gravity values are given on the Earth's surface. The sought quantity in the latter method is the height anomaly. In spherical approximation, the basic equation for the geoid height is (Stokes, 1849)

$$N = \frac{R}{4\pi\gamma_e} \iint_{\sigma} \Delta g S(\psi) d\sigma \quad (7a)$$

and for the height anomaly (Molodensky et al., 1962)

$$\zeta_k = \frac{R+H}{4\pi\gamma_e} \iint_{\sigma} g_k S(\psi) d\sigma \quad (7b)$$

where  $\Delta g$  denotes the gravity anomaly on the geoid,  $R$  is the Earth's mean radius approximating the geoid,  $\gamma_e$  is normal gravity on the reference ellipsoid,  $\gamma_e$  is normal gravity on the telluroid,  $\sigma$  is the unit sphere,  $\psi$  is the spherical distance between the computation point and spherical surface element  $d\sigma$ , and  $S(\psi)$  is the spherical Stokes function. The parameter  $g_k$  represents the gravity anomaly defined as a difference of gravity measured on the Earth's surface and normal gravity on the telluroid, that is expressed as a series expansion leading to corresponding terms for the height anomaly  $\zeta_k$  (Moritz, 1980a; Sideris, 1995).

The evaluation of these integral transforms is carried out spatially, spectrally, or stochastically, with the last two approached being the most common computational strategies used in practice. Inserting the integration limits for  $\varphi$  and  $\lambda$ , the 1-D convolution integral along parallels is defined between quantity  $\Delta g \cos\varphi$  and the Stokes function  $S(\psi)$ . This enables the utilisation of the convolution theorem in Fourier's theory and leads to an evaluation of the geoid heights by the 1-D Fourier Transform along meridians (Haagmans et al., 1993)

$$N(\varphi, \lambda) = \frac{R}{4\pi\gamma_e} \mathbf{F}_{\lambda}^{-1} \left\{ \int_{\varphi'=-\pi/2}^{\pi/2} \mathbf{F}_{\lambda} [\Delta g(\varphi', \lambda) \cos\varphi'] \mathbf{F}_{\lambda} \{S(\varphi, \lambda)\} d\varphi' \right\} \quad (7c)$$

where  $\varphi'$  is the latitude at the integration point,  $\mathbf{F}_{\lambda}$  is the Fourier

transform operator along longitudes and  $\mathbf{F}_{\lambda}^{-1}$  its inverse.

In order to avoid the numerical integration along meridians, different approximations have been proposed that transform the integral expression for the geoid height to a 2-D convolution, suitable for a spectral evaluation, for instance, according to Sideris (2016).

$$N(\varphi, \lambda) = \frac{R}{4\pi\gamma_e} \mathbf{F}^{-1} \{ \mathbf{F} [\Delta g(\varphi, \lambda) \cos\varphi] \mathbf{F} [S(\varphi, \lambda, \bar{\varphi})] \} \quad (7d)$$

where  $\bar{\varphi}$  denotes a mean latitude value for the area under consideration and  $\mathbf{F}$  and  $\mathbf{F}^{-1}$  are the Fourier transform operator and its inverse, respectively.

The stochastic approaches comprise different techniques that apply some sort of statistical tools to evaluate individual parameters, for instance, different least-squares estimators for the Stokes integral as a result of different stochastic characteristics of local gravity data and used EGM, or the integration cap radius (Varga et al., 2021). Key representative in this family of methods is least-squares collocation (Krarup, 1969), a versatile stochastic process that best represents the disturbing potential and that allows to perform predictions and error estimates of gravity data as functionals of the disturbing potential, the only requirement being the availability of the corresponding signal and error covariance functions (Tscherning and Rapp, 1974). For example, the residual height anomaly, obtained from surface gravity data reduced for the contribution of a selected EGM, is given by the following expression (Krarup, 1969; Wang et al., 2016)

$$\zeta_{res} = \mathbf{C}_{cf} (\mathbf{C}_{ff} + \mathbf{C}_{mm})^{-1} \mathbf{f} \quad (7e)$$

where  $\mathbf{f}$  represents a vector of observed gravity data,  $\mathbf{C}_{cf}$  is the cross-covariance matrix between the residual height anomaly and gravity observations, and the other two matrices on the right-hand side of Eq. (7e) represent the signal and error covariance matrices of the observations.

The disturbing potential and its different functionals can alternatively be described by means of spherical radial basis functions, a mathematical tool expressing local characteristics and proving to serve as a best compromise between frequency and spatial localisation. A spherical radial basis function centred at points  $P_k$  on the geocentric sphere with radius  $R$  is defined between  $P_k$  and an observation point  $P$  through a Legendre series as follows (Freedeen et al., 1998)

$$B(\mathbf{x}, \mathbf{x}_k) = \sum_{n=0}^{\infty} \frac{2n+1}{4\pi} \left(\frac{R}{r}\right)^{n+1} B_n P_n(\mathbf{r}^T \mathbf{r}_k) \quad (7f)$$

where  $\mathbf{x}$  denotes the geocentric position vector,  $P_n$  are the Legendre polynomials of the degree  $n$ , and  $B_n$  are coefficients contributing to the shape of the radial basis functions. A harmonic function  $F(\mathbf{x})$  can be expressed in terms of spherical radial basis functions as the following series (Liu et al., 2020)

$$F(\mathbf{x}) = \sum_{k=1}^K d_k B(\mathbf{x}, \mathbf{x}_k) \quad (7g)$$

where  $K$  is the number of grid points  $P_k$  as well as sought coefficients  $d_k$ . After using the spherical radial basis function representation for specific functionals, an estimation model can be defined linking this representation to the corresponding observations leading eventually to estimates for the coefficients  $d_k$ .

All geoid modelling methods combine local gravity data with harmonic coefficients of an EGM. The most commonly used procedure is the three-step remove-compute-restore scheme. In the first step, residual gravity data is computed by subtracting the low-frequency EGM contribution and residual topographic effects from observed gravity data. The residual geoid heights or height anomalies are then evaluated and finally the EGM contribution and topographic effects, removed in the first step, are restored to obtain the complete geoid height or height

anomaly (Barzaghi, 2016). A comprehensive application and evaluation of various methods mentioned above have recently been conducted as part of the Colorado experiment (Wang et al., 2021). Fourteen groups from different countries estimated local geoid and quasigeoid models by using the same terrestrial and airborne gravity data, covering a study area of  $5^\circ \times 4^\circ$  in Colorado, USA. The majority of solutions employed the remove-compute-restore technique with variations in the parameters for modifying the Stokes kernel or spectrally combining the EGMs with local gravity data. The implemented geoid estimation algorithms included Fourier transforms, least-squares modification of Stokes's formula with additive corrections, spherical radial basis functions, and least-squares collocation. Despite the diverse approaches, the different models exhibited a consistent agreement with a standard deviation of differences at the level of  $\pm 2$  cm, thus providing a benchmark for calibrating regional gravity field modelling methods.

#### 4.1.2. Height systems

In geodesy and surveying, different physical heights are used, particularly orthometric and normal heights. The two physical heights are related to the Earth's gravity field and use the geoid as their common reference surface. If they are estimated by GNSS, the geoid height and the height anomaly are applied to transform the ellipsoidal height into the respective physical height. They can be also obtained by spirit levelling starting from a benchmark with the known orthometric/normal height. Respective corrections – normal or orthometric – must be then applied to levelled height differences.

Orthometric and normal heights of a point  $P$  are physical heights (minimum distances in physical sense) defined using the geopotential number  $C(P)$ , i.e.,

$$C(P) = \int_{P_0}^P g \, d\ell = W_0 - W_P \quad (8a)$$

where  $P_0$  is a respective point on the geoid along the plumbline passing through the point  $P$ ,  $W_0 = W(P_0)$  is the reference gravity potential associated to the geoid,  $W_P = W(P)$  is the gravity potential at  $P$ , and  $g = |\nabla W|$  along the plumbline  $\ell$  from  $P_0$  to  $P$ . It is obvious that both normal and orthometric heights are equal to zero if the point  $P$  is at the geoid.

The orthometric height is defined as (Heiskanen and Moritz, 1967)

$$H(P) = \frac{C(P)}{\bar{g}} \quad (8b)$$

where the mean value of gravity along the plumbline between the geoid and surface point  $P$  reads

$$\bar{g} = \frac{1}{H_P} \int_{P_0}^P g \, d\ell \quad (8c)$$

The orthometric height of a point  $B$  can be obtained via spirit levelling (Heiskanen and Moritz, 1967) along a levelling line starting from a point  $A$  with the known orthometric height, so that

$$H_B - H_A = \Delta L_{AB} + \int_A^B \frac{g - \gamma_0}{\gamma_0} dl + H_B \frac{\gamma_0 - \bar{g}_B}{\gamma_0} - H_A \frac{\gamma_0 - \bar{g}_A}{\gamma_0} = \Delta L_{AB} + \Delta H^{ort} \quad (8d)$$

where  $H_A$  and  $H_B$  are the orthometric heights of the points  $A$  and  $B$ , respectively,  $\Delta L_{AB}$  is the levelled height increment,  $\Delta H^{ort}$  is the orthometric correction, and  $\gamma_0$  is the value of normal gravity at the latitude  $\varphi = 45^\circ$ . The orthometric correction depends on gravity between the surface points  $A$  and  $B$  and the geoid (values of  $\bar{g}_A$  and  $\bar{g}_B$ ), exactly as the mean gravity in Eq. (8c), that makes its estimation more difficult.

To avoid the necessity of knowing gravity inside topography, the normal height  $H_p^*$  of a point  $P$  was defined following an approach similar to that used in the definition of the orthometric height. For that, we consider the normal potential  $U$  and the modulus of the normal gravity  $\gamma = |\nabla U|$  of the reference ellipsoid (Heiskanen and Moritz, 1967). We

then write for a given point  $Q$  the following expression

$$\int_0^Q \gamma \, dh = U_0 - U_Q \quad (8e)$$

where  $U_0$  is the normal potential at the reference ellipsoid and the integral is along the surface normal to the reference ellipsoid. If we further assume that  $U_0 = W_0$  and that the point  $Q$  is selected so that  $U_Q = W_P$ , where  $P$  is the point on the Earth surface, we have

$$\int_0^Q \gamma \, dh = U_0 - U_Q = W_0 - W_P = C(P) \quad (8f)$$

The normal height  $H_p^*$  of a point  $P$  is then defined as

$$H^*(P) = \frac{C(P)}{\bar{\gamma}} \quad (8g)$$

where

$$\bar{\gamma} = \frac{1}{H_p^*} \int_0^Q \gamma \, dh \quad (8h)$$

The normal height of the point  $P$ ,  $H^*(P)$ , is equivalent to the height of the point  $Q$  at the telluroid above the reference ellipsoid. Still, the normal height of the point  $P$  is zero only if the point is at the geoid; thus, the reference surface for normal heights is also the geoid.

Normal heights can also be estimated by spirit levelling. By levelling the height increment  $\Delta L_{AB}$ , the normal height difference between the two points  $A$  and  $B$  can be obtained as

$$H_B^* - H_A^* = \Delta L_{AB} + \int_A^B \frac{g - \gamma_0}{\gamma_0} d\ell + H_B^* \frac{\gamma_0 - \bar{\gamma}_B}{\gamma_0} - H_A^* \frac{\gamma_0 - \bar{\gamma}_A}{\gamma_0} = \Delta L_{AB} + \Delta H^* \quad (8i)$$

where  $\Delta H^*$  is the normal correction (Heiskanen and Moritz, 1967). In contrary to the orthometric correction above, it depends only on gravity measured at the Earth's surface (see the integral in Eq. 8i) and no hypotheses on topographic mass density distribution must be adopted.

Given the definitions above, one can see the relationships between physical height definitions and the Earth's gravity field. As mentioned above, one can obtain physical height differences (either orthometric or normal) by spirit levelling. Therefore, to estimate physical heights of points, one must start the levelling line from a point with known orthometric or normal height. The mean-sea level (MSL) representing the regional geoid can be estimated by means of a tide gauge. Physical heights in a given region are then defined with respect to the particular MSL value. Different reference values have been defined and used around the world. Since the MSL does not rigorously coincide with the global geoid (see the next session), different regional height systems are not coherent. Given that the discrepancy between the global geoid and local MSL estimates can amount to 2 m, one can have discrepancies between different regional height systems at the order of decimetres or more. In the past, this was considered tolerable; however, in view of highly accurate geodetic observations and their global distribution, inconsistencies among different regional height systems become critical.

In recent years, several authors have proposed methods for unification of the existing physical height systems that are based on the improved knowledge of the global geoid, e.g., (Rummel and Teunissen, 1988; Rummel, 2012; Rummel et al., 2014). Following this progress, the resolution on the definition and the realisation of a unified physical height system was accepted by the International Association of Geodesy (IAG). Based on this resolution, the International Height Reference System (IHR) and its realisation (see International Height Reference System 2015), the International Height Reference Frame (IHRF), were defined (Ihde et al., 2017). In the IHR/IHRF, orthometric and normal heights are obtained in terms of the geopotential numbers as in Eqs. (8b) and (8g). Furthermore, the conventional value

$$W_0 = 62,636,853.4 \text{ m}^2 \text{ s}^{-2} \quad (8j)$$

is assumed as the common reference value for the Earth's gravity potential at the geoid level (Sánchez et al., 2016). In this way, the physical height of any point  $P$  on, below or above the Earth's surface in the IHRF can be obtained once the geopotential  $W(P)$  in that point is known. Again, this proves the close relationship between physical heights and the knowledge of Earth's gravity field even in this modern concept.

Thus, the IHRF/IHRF height of the point  $P$  on, below or above the Earth's surface is given via the estimation of  $W(P)$  obtained as

$$W(P) = U(P) + \gamma(P) \zeta(P) + \Delta W_0 \quad (8k)$$

where  $U(P)$  is the value of the GRS80 normal potential (Moritz, 1980b),  $\gamma(P)$  is GRS80 normal gravity (Moritz, 1980b),  $\zeta(P)$  is the height anomaly (Heiskanen and Moritz, 1967), and

$$\begin{aligned} \Delta W_0 &= W_0 - U_0 = 62,636,853.40 \text{ m}^2 \text{ s}^{-2} - 62,636,860.85 \text{ m}^2 \text{ s}^{-2} \\ &= -7.45 \text{ m}^2 \text{ s}^{-2} \end{aligned} \quad (8l)$$

is the term that accounts for the discrepancy between the new conventional  $W_0$  in Eq. (8j) and the  $U_0$  is the GRS80 value at the reference ellipsoid (Moritz, 1980b). The height anomaly  $\zeta(P)$  can be directly evaluated from surface gravity values with, e.g., collocation. Since the normal potential and normal gravity are expressed via analytical formulas with known fundamental constants (Moritz, 1980a), estimating the normal height of the point  $P$  is equivalent to estimating the height anomaly  $\zeta$  (by IHRF/IHRF conventions in the zero-tide system). As previously mentioned, the Colorado test proved that the geoid heights and the height anomalies can be estimated at the precision level of  $\pm 2$  cm. This means that soon, following the IHRF/IHRF concept, globally coherent physical heights will be available at this precision level, a significant improvement with respect to the present-day situation.

#### 4.1.3. Ocean dynamic topography, geostrophic and eddy currents

In oceanic regions, the global geoid is approximated by the mean sea surface. However, the ocean surface does not precisely coincide with the equipotential surface of the Earth's gravity field. By averaging the ocean surface over time and accounting for all temporal variations such as ocean tides, the mean sea level (MSL) is obtained for the corresponding time interval. Even after accounting for all time-dependent variations, a quasi-stationary component persists. Furthermore, the long-term average of the geometric ocean surface, known as MSL, is not exactly an equipotential surface due to remaining non-gravitational forces and sea water variability (sea water temperature and salinity, atmospheric pressure variations, sea level rise, etc.). These effects displace the sea surface from the geoid. This quasi-stationary component is referred to as

the mean dynamic topography (MDT) which represents the orthometric height of the sea surface.

Satellite altimetry is utilised to measure the geometric height  $h$  of an instantaneous sea surface, while gravity observations can be used to compute the geoid height  $N$ . Mathematically, the MDT is then defined by

$$\zeta = h - N \quad (9a)$$

Geostrophic ocean currents result from an exact balance between the Coriolis force and the pressure gradient force at the sea surface. They can, in turn, be derived from the horizontal gradients of the mean dynamic topography  $\zeta$  as follows (Hwang et al., 2002):

$$u_{\text{geo}} = \frac{g}{f} \frac{1}{R} \frac{\partial \zeta}{\partial \theta} \quad (9b)$$

$$v_{\text{geo}} = \frac{g}{f} \frac{1}{R} \frac{\partial \zeta}{\sin \theta \partial \lambda} \quad (9c)$$

where  $u_{\text{geo}}$  and  $v_{\text{geo}}$  represent the northward and eastward geostrophic velocity components, respectively,  $g$  denotes gravity,  $f = 2\tilde{\omega} \cos \theta$  represents the Coriolis force, and  $\tilde{\omega}$  is the Earth's angular velocity. Eqs. (9b) and (9c) are simplified versions of the Navier-Stokes equations, in which the pressure gradient force is balanced by the Coriolis effect, i.e., geostrophic condition. The surface currents travel along the isolines of the MDT.

As an example, Fig. 4a shows the MDT in the region of the Gulf Stream derived from a combination of satellite altimetry and gravity data, and Fig. 4b the geostrophic ocean current velocities derived from it.

Eddy currents, also referred to as Foucault's currents, wield substantial influence over oceanic dynamics and exert their impact on a wide array of marine phenomena. The wealth of knowledge, derived from geostrophic velocities related to the eddies, finds diverse applications. This information proves invaluable for investigating the role of eddies in processes such as oceanic heat transport, dispersion of nutrients, cycling of carbon, and the distribution of marine organisms. The insights gleaned from geostrophic velocities significantly contribute to advancing our comprehension of climate variability, oceanic mechanisms, and the dynamics of ecosystems. To gain a comprehensive understanding of the influence of the eddies on ocean circulation, heat transport, and biogeochemical cycling (Chelton et al., 2011), it becomes imperative to grasp their characteristics and behavioural patterns. This understanding has been greatly enriched through the examination of geostrophic velocities, facilitated by satellite altimetry and in situ observations (Dong et al., 2018).

The examination of geostrophic velocities, derived from satellite altimetry, has greatly advanced our knowledge of eddy properties and

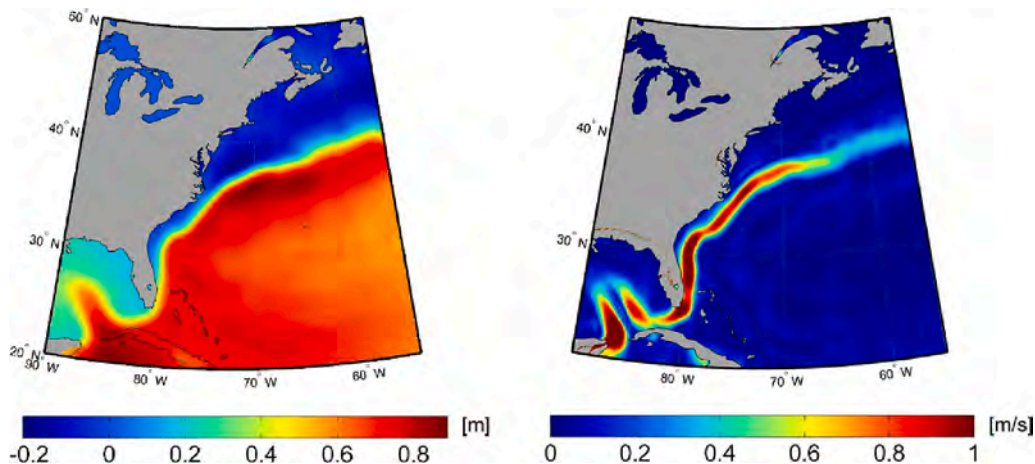


Fig. 4. a) Geoid MDT, and b) geostrophic ocean current velocities of the Gulf stream region.

their global distribution. Chelton et al. (2011) provided a comprehensive overview of nonlinear mesoscale eddies, emphasising the importance of geostrophic velocities in capturing eddy dynamical features and their influence on large-scale circulation patterns. The synergy between satellite altimetry and ocean modelling has further enhanced our ability to study these currents, as highlighted by Morrow et al. (2019), who emphasised the value of combining satellite altimetry data with numerical models. Recent studies have also focused on assimilating geostrophic velocities into regional ocean models to simulate mesoscale eddies in specific regions. Cui et al. (2019) successfully used satellite altimetry data to study eddies in South China Sea, demonstrating the utility of incorporating geostrophic velocities into models for regional-scale studies. Advancements in satellite altimetry and gravimetry techniques and data processing have deepened our understanding of the connections between geostrophic velocities and eddy-induced processes. Dong et al. (2018) discussed the role of satellite altimetry in capturing eddy characteristics and variability, highlighting both challenges and opportunities in using geostrophic velocities for studying eddy dynamics and their impacts on the oceanic environment. Additionally, Qiu and Chen (2005) investigated heat transport by eddies in the North Pacific, using geostrophic velocities derived from altimetry data to reveal the crucial role of transient eddies in heat exchange between the ocean and atmosphere.

Determination of the eddy current geometry from satellite altimetry-derived geostrophic velocities has also been extensively investigated. For example, Hwang et al. (2002) examined mesoscale eddy kinematics in the region of subtropical counter currents using the TOPEX/Poseidon altimetric data, shedding light on the dynamics and characteristics of these eddies. Similarly, Chaigneau et al. (2008) studied the mesoscale eddies off the coast of Peru and the subtropical counter currents, employing altimeter records and specific identification techniques to extract information about eddy geometry and dynamics.

To illustrate how eddy current geometry is derived from geostrophic velocities, the approaches used by Hwang et al. (2002) and Chaigneau et al. (2008) are briefly described. For this purpose, we introduce the following parameters

$$\tilde{\Omega} = G_{21} - G_{12} \quad (9d)$$

$$\tilde{\gamma}_1 = G_{21} + G_{12} \quad (9e)$$

$$\tilde{\gamma}_2 = G_{11} - G_{22} \quad (9f)$$

$$\tilde{\psi} = G_{11} + G_{22} \quad (9g)$$

defined for

$$G_{11} = \frac{\partial u_{\text{geo}}}{\partial x}, G_{12} = \frac{\partial u_{\text{geo}}}{\partial y}, G_{21} = \frac{\partial v_{\text{geo}}}{\partial x} \text{ and } G_{22} = \frac{\partial v_{\text{geo}}}{\partial y} \quad (9h)$$

where  $\tilde{\Omega}$  is called the vorticity, which is twice the angular velocity of the current. It is positive in the northern hemisphere with cold/cored or low pressure, and negative for the warm/corded or high pressure. The parameters  $\tilde{\gamma}_1$  and  $\tilde{\gamma}_2$  are the shear and stretching deformation rates, and  $\tilde{\psi}$  is the divergence. A positive/negative stretching deformation shows extension/compression in the west/east direction and compression/extension in the south/north direction. A positive stretching rate means that a circular eddy becomes an ellipse with its major/minor semi-axes along the east-west direction. A positive/negative shear rate means extension/compression in the northeast/southwest direction a compression/extension in the northwest/southeast direction. Then a positive shear rate means an elliptical eddy elongated northeast/southwest.

The total deformation is defined by (Carton, 2001; p. 220)

$$\tilde{\gamma} = \sqrt{\tilde{\gamma}_1^2 + \tilde{\gamma}_2^2} \quad (9i)$$

The mathematical relation between the geostrophic velocities and

the kinematic parameters of an eddy current is given by (Hwang et al., 2002)

$$u_{\text{geo}} = G_{11}(x - x_0) + G_{12}(y - y_0) + u_c \quad (9j)$$

$$v_{\text{geo}} = G_{21}(x - x_0) + G_{22}(y - y_0) + v_c \quad (9k)$$

where  $(x, y)$  are the Cartesian coordinates of the particles in a local coordinate frame,  $(x_0, y_0)$  represent the coordinates of the centre of eddy, and  $u_c$  and  $v_c$  are instantaneous velocities of the centre of the eddy relative to the water around.

In fact, the left-hand sides of Eqs. (9j) and (9k) defining the geostrophic velocities are considered as observations, and  $G_{11}$ ,  $G_{12}$ ,  $G_{21}$ ,  $G_{22}$ ,  $x_0$ ,  $y_0$ ,  $u_c$ , and  $v_c$  are the unknown parameters to be estimated. Therefore, there are two equations and eight unknowns, which means that more particles over the eddy area should be used so that an over-determined system of linear equations can be created and the optimal estimates for the unknown parameters are derived; see Hwang et al. (2002) or Chaigneau et al. (2008) for more details.

#### 4.1.4. Crustal thickness

The Mohorovičić discontinuity, commonly referred to as ‘‘Moho’’, represents the boundary between the Earth’s crust and the uppermost mantle. This boundary is typically determined through seismic or gravimetric methods. Isostasy is used to compute the Moho depth, with different isostatic theories being implemented for this purpose (Pratt, 1854; Airy, 1855; Vening Meinesz, 1931; Heiskanen, 1931). According to Airy (1855), mountains have roots below the surface, and the depth of these roots changes in a manner opposite to that of the topographic heights. On the other hand, Vening Meinesz (1931) proposed that the lithosphere bends due to the force exerted by topographic masses on its surface. A thicker lithospheric shell exhibits greater stiffness and consequently bends less, leading to the transition from local to regional compensation in the Vening Meinesz theory.

Recent advancements in Moho depth determination have been marked by significant contributions across various methodologies and data sources. Parker (1972) initiated the use of iterative solutions with Fourier transforms for gravitational anomalies, which Oldenburg (1974) refined by filtering out higher-frequency terms. Sünkel (1985) adapted the Airy-Heiskanen model into a Vening Meinesz-computed model through iterative least-squares, integrating disturbing and topographic-isostatic potentials. Moritz (1990) introduced a global spherical approximation for Moho depth estimation using an integral formula based on isostatic compensation principles. Subsequent studies explored diverse approaches for regional Moho depth determination. Braitenberg et al. (2000) and Gómez-Ortiz et al. (2005) utilised gravity data inversion, employing spectral, classical, and Parker-Oldenburg methods. Shin et al. (2015) combined GRACE and terrestrial gravity data, while Sjöberg (2009) reformulated Moritz’s solutions, developing the Vening Meinesz-Moritz (VMM) inverse problem framework. Further contributions include Reguzzoni and Sampietro (2012) and Reguzzoni et al. (2013), who utilised GOCE gravitational gradients for global Moho modelling, and Barzaghi et al. (2016), who applied collocation methods using GOCE and terrestrial data. Eshagh (2016), Eshagh and Hussain (2016) made notable advancements in local and regional Moho depth estimations and modelling techniques. Studies like Gedamu et al. (2020) have also highlighted the importance of accounting for geological anomalies, such as mantle plumes, in Moho depth calculations. Abreh-dary and Sjöberg (2023) further explored the correlation between crustal thickness and Moho depth, emphasising the relationship between geological properties and geophysical measurements. These efforts collectively enhance our understanding of the Earth’s crustal structure through refined Moho depth determination techniques.

One assumption commonly made in studies of the Earth’s crustal structure is that the crust and mantle are in an isostatic equilibrium. Several models have been developed to explain this equilibrium,

including the Airy-Heiskanen, Pratt-Hayford, and Vening Meinesz models (Vening Meinesz, 1931). These models have been extensively discussed in the literature (Heiskanen and Moritz, 1967; Vermeer, 2020). In the gravimetric approach to Moho determination, the main assumption is that the isostatic gravity anomaly should be zero, so that the crust remains in isostatic balance. This assumption is presented mathematically by

$$\Delta g' = \Delta g - \Delta g^{\text{TBSCI}} + \Delta g^{\text{CMP}} = 0 \quad (10a)$$

where  $\Delta g$  is the gravity anomaly,  $\Delta g^{\text{TBSCI}}$  is the total effect of the topographic and bathymetric masses, sediments, crustal crystalline, and ice on  $\Delta g$ , and  $\Delta g^{\text{CMP}}$  is the compensation effect of these masses on  $\Delta g$ . If  $\Delta g=0$  in Eq. (10a), then  $\Delta g^{\text{TBSCI}} = \Delta g^{\text{CMP}}$ , meaning that the gravimetric isostasy becomes the Airy-Heiskanen model with extremely local compensation property.

The compensation depth at the so-called the Moho discontinuity  $\tilde{D}_0$  and the density contrast  $\Delta\rho$  between the crust and upper mantle are two important factors needed for modelling this equilibrium. The variation of Moho depth with respect to  $\tilde{D}_0$  can be determined by (Eshagh, 2017)

$$\Delta\tilde{D} = \frac{1}{4\pi GR\Delta\rho} \sum_{n=0}^{\infty} \frac{2n+1}{n-1} \beta_n^* \Gamma_n \sum_{m=-n}^n (\Delta g_{nm}^{\text{TBSCI}} - \Delta g_{nm}) Y_{nm}(\theta\lambda) \quad (10b)$$

where  $G$  is the Newtonian gravitational constant, and the parameters  $\beta_n^*$  and  $\Gamma_n$  read

$$\beta_n^* = \begin{cases} 1 & \text{over oceans} \\ \left[1 + (n+2) \frac{\tilde{D}_0}{2R}\right]^{-1} & \text{over continents} \end{cases}, \Gamma_n = \left(\frac{R}{R - \tilde{D}_0}\right)^{n+2} \quad (10c)$$

The Moho density contrast  $\Delta\rho$  can also be determined from  $\Delta\tilde{D}$ , if its available or even the product  $\Delta\rho\Delta\tilde{D}$  (e.g., Eshagh et al., 2016) in which the GOCE data are constrained to seismic data for determination of  $\Delta\rho\Delta\tilde{D}$ . Fig. 5 shows the map of the Moho depth recovered from the GOCE gravity gradients over central Asia based on their approach. They used the average value of the Moho depth from the CRUST1.0 model Laske et al. (2013) over the study area, also, considered the effects of the crustal heterogeneities, sediment thickness in addition to the topography model of the area. The GOCE data was inverted directly to  $\Delta\rho\Delta\tilde{D}$  using integral equations, and later constrained by the seismic model of CRUST1.0 through condition adjustment separating the Moho depth

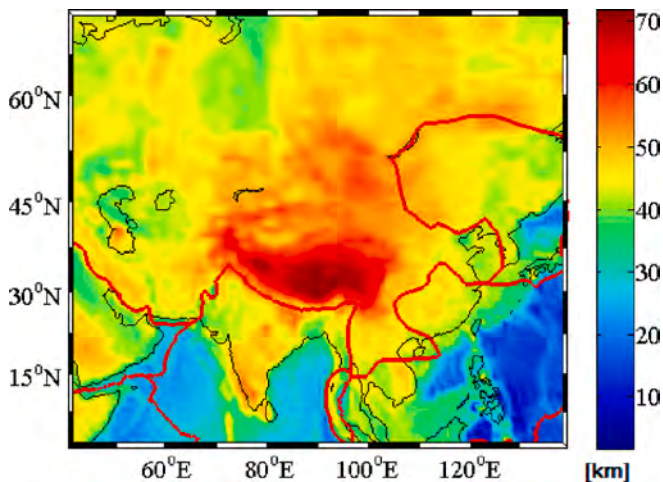


Fig. 5. Map of the Moho depth computed from inversion of GOCE gravity gradients over Central Asia, after Eshagh et al. (2016).

from the density contrast.

#### 4.1.5. Elastic thickness and rigidity

The original concept, proposed by Vening Meinesz (1931), envisions the Earth's crust as a thin elastic plate that undergoes bending when subjected to external loads. In this framework, the flexure of the plate is influenced by both the magnitude of the load and the mechanical properties of the plate, including its thickness. By considering the lithosphere as a thin elastic shell, researchers have sought to determine the effective elastic thickness ( $T_e$ ) by integrating the principles of flexure theory and gravimetric isostasy. Subsequently, various researchers have advanced this idea by employing spectral methods such as admittance and coherence analyses, which explore the relationships between topography and gravity anomalies.

The study of Earth's elastic thickness  $T_e$  has seen significant progress with diverse methodologies and regional assessments. Early works by Calmant et al. (1990) and Filmer et al. (1993) explored  $T_e$  in relation to oceanic lithosphere age and island flexure, respectively. Investigations extended across various regions, from Canada by Audet and Mareschal (2004) to the Iberian Peninsula by Gómez-Ortiz et al. (2005), and included analyses of continental lithosphere by Burov and Diament (1995), as well as studies on flexural rigidity and gravity anomalies by Stewart and Watts (1997) and McKenzie and Fairhead (1997). Martian lithospheric studies were undertaken by Johnson et al. (2000), employing a combination of Jeffrey's Moho determination method and flexural theory. Inverse modelling and spectral methods have been instrumental, as seen in the works of Braitenberg et al. (2002) and Kirby (2014), with further applications to the Arabian plate by Chen et al. (2015). Martian  $T_e$  was also a focus, with McGovern et al. (2002) using the admittance method and various regional studies employing coherence methods, comparative analyses, and the Forsyth (1985) method highlighted by McKenzie (2003, 2010) and Swain and Kirby (2003a, 2003b). Tassara (2005) and Jordan and Watts (2005) reviewed flexural analysis and gravity modelling techniques for the Andean margin and India-Eurasia collision zone, respectively. Wavelet and classical spectral isostatic analysis were applied to South America by Tassara et al. (2007), with Pérez-Gussinyé and Watts (2005) and Pérez-Gussinyé et al. (2007, 2009) conducting similar studies across Fennoscandia, South America, and Africa. Satellite-derived data have been used for  $T_e$  estimates over the Colombian Andes by Galán and Casallas (2010) and globally by Tesauro et al. (2013), with Abbaszadeh et al. (2013) and Zamani et al. (2014) focusing on Iran.

Eshagh (2018) introduced a spherical harmonic domain method for  $T_e$  determination, initially applied to South America and later extended to Asia and Africa, leveraging GOCE data, by Eshagh et al. (2019, 2020) and Eshagh and Pitoňák (2019). This method was further developed for the viscoelastic lithosphere over Fennoscandia by Eshagh and Tenzer (2021), showcasing the evolving techniques for understanding Earth's elastic thickness. Furthermore, Eshagh (2018) introduced a method for elastic thickness determination in a spherical harmonic domain, applying it initially to South America and later extending it to Asia. This approach was further enhanced by Eshagh et al. (2018), who applied it to Asia, and Eshagh and Pitoňák (2019), who utilised GOCE data for estimating the elastic thickness of Africa. Eshagh et al. (2020b) subsequently applied this method over Iran, while Eshagh and Tenzer (2021) developed the theory for viscoelastic lithosphere and applied it over Fennoscandia. The method presented by Eshagh (2018) entails an analysis in the spherical harmonic domain for the determination of  $T_e$ . This approach is based on the following mathematical expression:

$$\Delta g = \Delta g^{\text{TBSCI}} - 4\pi GR \Delta\rho \sum_{n=0}^{\infty} \Gamma_n \frac{n-1}{2n+1} \beta_n^* C_n^{-1} \sum_{m=-n}^n \bar{K}_{nm} Y_{nm}(\theta, \lambda) \quad (11a)$$

with

$$\bar{K}_{nm} = (\bar{\rho}d)_{nm} + (\rho^s d_s)_{nm} + (\rho^c d_c)_{nm} + (\rho^l d_l)_{nm} \quad (11b)$$

where  $\Delta g^{\text{TBSCl}}$  is the joint effect of topographic, bathymetric masses, sediments, crystalline and ice on gravity anomaly,  $\bar{\rho}$  is the density of the topographic masses when the computation point is in continents and the density contrast between the water and topographic masses when it is over ocean,  $d$  stands for the topographic height or bathymetric depth,  $\rho^s$  and  $d_s$  are the density and thickness of sediment layers,  $\rho^c$  and  $d_c$  the corresponding values for a crustal crystalline, and  $\rho^l$  and  $d_l$  those of the ice,  $(\bullet)_{nm}$  means the spherical harmonic coefficients, and  $C_n$  is the compensation degree. The compensation degree is derived from the flexure isostasy model as follows (e.g., Eshagh, 2016)

$$C_n = \frac{n^2(n+1)^2 \tilde{\theta} + \Delta\rho}{R^4 g} \quad \text{and} \quad \tilde{\theta} = \begin{cases} D^{\text{Rig}} & \text{if flexural rigidity is desired} \\ \frac{ET_e^3}{12(1-\nu^2)} & \text{if elastic thickness is desired} \end{cases} \quad (11c)$$

where  $g$  is the gravity attraction,  $E$  stands for the Young modulus, and  $\nu$  is the Poisson ratio. The left-hand side of Eq. (11a) defines the gravity anomalies excluding the signals from sub-lithosphere, degrees below 15. A proper elastic thickness can be found by inserting different values  $C_n$  and inserting it in Eq. (11a) and checking which one gives the closest value to the gravity anomaly of lithosphere.

They developed a mathematical model akin to Eq. (11a), tailored for the second-order radial derivative of the gravitational potential as measured by GOCE. The model incorporates the effects of topographic and bathymetric masses, along with sediments and crystalline structures, derived from the CRUST1.0 model. The estimation of  $T_e$  involves a search method where an upper bound of 100 km is initially set for the search domain. Values ranging from 0 to 100 km, in increments of 1 km, are tested within the equations to identify the one that best approximates the GOCE data or minimises the discrepancy between the left and right sides of the model. The  $T_e$  value that meets this criterion is then selected for that specific point. It is important to note that at certain locations, such a minimum may not be identifiable, making smoothing an essential step post- $T_e$  estimation. Fig. 6 displays the  $T_e$  determined from GOCE gradient data over Africa, as reported by Eshagh and Pitoňák (2019).

#### 4.1.6. Ocean bathymetry, ice thickness and sediment basement

Satellite gravimetry/altimetry has transformed our understanding of

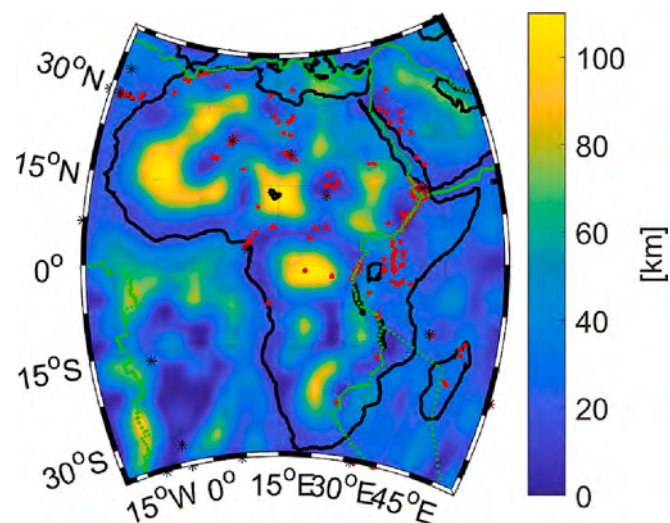


Fig. 6. The elastic thickness ( $T_e$ ) of the lithosphere in Africa from the GOCE gradient data (Eshagh and Pitoňák, 2019).

Earth's system, particularly in marine areas. Satellite bathymetry provides precise measurements of seafloor depths, revealing intricate underwater landscapes and enhancing our knowledge of marine environments. These methods are pivotal for research in oceanography, geology, and climate science, providing critical data on Earth's dynamic aquatic ecosystems. This section will cover these techniques in deepening our comprehension of the planet's aquatic regions. In addition to bathymetry, the problem of sediment thickness determination and estimating ice thickness are presented.

**4.1.6.1. Ocean bathymetry.** Over past decades, various algorithms for deriving bathymetric predictions from satellite altimeter data have been developed and published. Walter and Sandwell (1994) addressed challenges related to dense but widely spaced satellite-derived gravity data (with track spacing of 2–4 km) and limited shipboard depth soundings (with hundreds of kilometres between tracks in some areas) on the southern oceans (south of 30° S). They introduced flexural isostatic compensation theory, suggesting a potential linear correlation between bathymetry and downward continued gravity data within a specific wavelength range (15–160 km), given thin sediment cover and moderate seafloor relief and proposed a methodology that combines this theoretical framework with Wiener optimisation theory and empirical evidence for gravity noise-to-signal ratios. This approach was used to design filters (low-pass and band-pass) for predicting bathymetry from gravity data. A review by Calmant and Baudry (1996) discusses the utilisation of satellite altimetry data to determine the gravity field of global oceans. This data is then employed to predict the bathymetry of deep-seafloor features like seamounts and ridges. Hwang (2010a, 2010b) discussed the development of a bathymetric model for the South China Sea using a combination of altimeter-derived gravity anomalies, shipborne depth measurements, ETOPO5 data (National Geophysical Data Center, 1993), and Generic Mapping Toolbox (GMT) shorelines (Wessel and Smith, 1998). Smith et al. (2006) discussed the need for globally uniform bathymetry, the role of satellite altimetry, factors that limit resolution, the current situation in bathymetry mapping, and the prospects for a future mission to improve bathymetric data. The authors emphasise that bathymetric survey lines cover remote ocean basins sparsely, like the way the Interstate Highway System covers the United States. Tozer et al. (2019) presented an updated global bathymetry and topography grid with the angular resolution of 15 arc sec. This grid is generated by combining shipboard soundings with depth predictions based on satellite altimetry data. The data used in this updated model includes over 33.6 million measurements obtained from multi-beam and single-beam sonar systems.

Presently, various satellite missions provide altimetry data over oceans, offering measurements of the distances between satellites and the ocean surface. These measurements, known as sea surface topography, deviate from the geoid. They serve as essential data for calculating geoid heights over oceans. While satellite gravimetry data or gravity models can be used for this purpose, they typically have limited resolutions. In cases where information on the average ocean depth is accessible, it allows us to define the variations in seafloor topography around it, as discussed by Eshagh (2021):

$$\Delta d = -\frac{1}{4\pi G \bar{\rho}} \sum_{n=0}^{\infty} \frac{2n+1}{B_n} \sum_{m=-n}^n (t_{nm} - v_{nm}^{\text{B/Iso}}) Y_{nm}(\theta, \lambda) - \left( \frac{R^2 A \delta_{n0}}{B_0} \right) \quad (12a)$$

where  $\delta_{n0}$  is the Kronecker delta. The remaining parameters in Eq. (12a) read

$$v_{nm}^{\text{B/Iso}} = -(v_{nm}^s + v_{nm}^c) + 4\pi G R \Delta\rho \Gamma_n^{-1} \beta_n^s C_n^{-1} \left[ (\rho^s d_s)_{nm} + (\rho^c d_c)_{nm} \right] \quad (12b)$$

which is the harmonics of isostatically compensated bathymetric masses, should be computed and removed from the observed disturbing

potential harmonics, the rest of parameters are already presented in Section 4.1.5.

In Eq. (12a), we have

$$A = \frac{1}{3R} \left[ 1 - \left( 1 - \frac{d_0}{R} \right)^3 \right] - \Delta\rho \frac{1}{R} \Gamma_0^{-1} \beta_0^* C_0^{-1} d_0 \quad (12c)$$

which a constant depending on the mean ocean depth  $d_0$ , and

$$B_n = R \left( \frac{R - d_0}{R} \right)^{n+2} + R \Delta\rho \Gamma_n^{-1} \beta_n^* C_n^{-1} \quad (12d)$$

where  $v_{nm}^s$  and  $v_{nm}^c$  are harmonic coefficients of the gravitational potentials of the sediment and crustal crystalline masses.

The compensation mechanism of isostasy is introduced to the model via  $C_n$ , which is a function of the mechanical properties of the lithosphere such as the Young modulus, Poisson ratio and  $T_e$ . The first parameters are determined from the seismic waves, for example, those provided in the CRUST1.0 model. The  $T_e$  of the oceanic lithosphere is needed, which can be independently determined with a proper approximation from the age of the oceanic lithosphere according to the following formula (Calmant et al., 1990):

$$T_e = \sqrt{\kappa t} \operatorname{erf}^{-1} \left( \frac{T}{T_m} \right) \quad (12e)$$

where  $t$  is the age of the oceanic lithosphere in Ma,  $\kappa = 31.5 \times 10^6$  the lithospheric diffusivity,  $T = 400\text{--}600$  °C stands for the lithospheric isotherm, and  $T_m = 1250$  °C is the temperature of the mantle. Finally,  $\operatorname{erf}^{-1}$  is the inverse of the error function.

**4.1.6.2. Ice thickness.** Various studies have focused on assessing glacier volume changes, typically relying on time-variable EGMs. Nevertheless, the primary objective of this section is to ascertain the static thickness or the average thickness at individual glacier points over a specific time-frame. Gravity data serves as a valuable tool for this purpose, but the key challenge lies in isolating the ice's contribution from the measurements.

Forsberg and Skourup (2005) utilised ICESat laser measurements to create a high-resolution map of the Arctic Ocean's sea-ice surface. They employed a "lowest-level" filtering scheme to invert these measurements, determining gravity anomalies and sea-ice freeboard heights. By integrating updated terrestrial gravity data from the Arctic Gravity Project with EGMs based on GRACE data, they improved the Arctic geoid model. This model aided in converting ICESat measurements into sea-ice freeboard heights using a coarse lowest-level surface method. The derived heights qualitatively matched multi-year sea-ice coverage, but the study noted a potential bias introduced by the filtering scheme. A comparison with an airborne lidar flight north of Greenland revealed this bias. In the work by Bull and Hardy (2017), a methodology was outlined for determining valley glacier thickness through gravity measurements. They measured gravity values at specific points on four transverse lines on a Norwegian glacier, about 4 km long and km wide. Gravity values were also measured on three lines in the valley below the glacier's snout for comparison. Positions and altitudes of these gravity stations were determined using triangulation techniques.

The thickness of ice can be determined using the following formula (Eshagh, 2020)

$$d_I = \frac{1}{4\pi GR} \sum_{n=0}^{\infty} \left( -\frac{\Delta\rho^I}{2n+1} + \Delta\rho\rho^I \Gamma_n^{-1} \beta_n^* C_n^{-1} \right)^{-1} \sum_{m=-n}^n (t_{nm} - v_{nm}^{\text{TSC/Iso}}) Y_{nm}(\theta\lambda), \quad (13a)$$

where  $\Delta\rho^I$  is the density contrast between the upper crust and ice,  $\rho^I$  stands for the density of ice, and

$$v_{nm}^{\text{TSC/Iso}} = -\left( v_{nm}^T + v_{nm}^S + v_{nm}^C \right) + 4\pi Gr \Delta\rho \Gamma_n^{-1} \beta_n^* C_n^{-1} \left[ (\rho^T H)_{nm} + (\rho^S d_S)_{nm} + (\rho^C d_C)_{nm} \right] \quad (13b)$$

Some approximations were employed in the derivation of Eq. (13a), rendering this method suitable for cases where the ice thickness is not substantial, and the maximum degree of the harmonic series is not excessively high. Eshagh (2021) noted that for the height of 10 km and maximum degree of 360, the relative error resulting from this approximation would be roughly 11%. For the maximum degree of 180, the relative error decreases to about 4%. When the height is reduced to 5 km, the relative error is about 4% for the maximum degree of 360 and <1% for the maximum degree of 180. One limitation of employing Eq. (13a) is its reliance on the elastic thickness, which must be known a priori from independent sources.

**4.1.6.3. Sediment thickness.** Sediments undergo compaction over time, resulting in a density gradient where the density is higher at their bottom and lower at their surface. Estimating the thickness of the sediments is a complex process due to the exponential increase in the sediment density with depth.

Woodward and Wood (2000) introduced an innovative approach to analyse satellite gravity data for assessing sedimentary structures in frontier basins. Their method involved simultaneously inverting for water, sediment and crustal thicknesses, offering valuable insights into the sediment thickness and basin structures, particularly in regions with limited data coverage. Later, Wood and Woodward (2002a, 2002b) utilised 3-D modelling of satellite gravity data to predict seafloor depths, basement structure, and Moho depth west of New Zealand. Sari and Şalk (2002) employed gravity anomalies with hyperbolic density contrast to estimate depths to the metamorphic basement in sedimentary basins, using gravity anomalies and hyperbolic density functions to identify structural features in West Anatolia. This study highlighted the potential for improved accuracy with density/depth functions and emphasised the importance of incorporating density gradients in modelling deep sedimentary basins. Engen et al. (2006a, 2006b) explored the use of altimetry-derived gravity data to predict sediment thickness in the Norwegian-Greenland Sea, offering a method applicable to simpler crustal areas for mapping sedimentary patterns. Braitenberg et al. (2006) analysed basement structures in the South China Sea using satellite-derived gravity data, challenging previous assumptions about the spreading centre's orientation. Braitenberg and Ebbing (2009) studied the basement structure of the West Siberian Basin, utilising GRACE satellite gravity data to map geological structures in remote basins, with implications for similar regions worldwide. Jung et al. (2013a, 2013b) conducted aero-geophysical surveys over Afghanistan, predicting gravity and sediment thickness in challenging terrains and providing valuable insights into gravity prediction and sediment thickness estimation. Kaban et al. (2021a, 2021b) investigated the sedimentary thickness of the Congo basin, creating a comprehensive map using decompensative gravity anomalies, revealing previously undiscovered deep depressions like the Salonga Basin. Elmas (2022) used the Bouguer gravity data to investigate sediment thickness in the Tuz Gölü Basin, employing various methods to estimate sediment thickness and identify discontinuity boundaries.

Eshagh (2020) employed various density contrast datasets to model the gravitational potential of the sediments. However, if an average and constant density is assumed for sediments, the following approximate formula can be utilised to determine the sediment thickness, e.g., (Eshagh, 2021),

$$d_S = \frac{\rho^S}{-4\pi GR} \sum_{n=0}^{\infty} \left( -\frac{1}{2n+1} + \Delta\rho \Gamma_n^{-1} \beta_n^* C_n^{-1} \right)^{-1} \sum_{m=-n}^n (t_{nm} - v_{nm}^{\text{BC/Iso}}) Y_{nm}(\theta\lambda) \quad (14a)$$

where  $\Delta\rho^I$  is the density contrast between the upper crust and ice,  $\rho^I$  stands for the density of ice, and

$$v_{nm}^{BC/iso} = -(v_{nm}^B + v_{nm}^C) + 4\pi GR \Delta\rho \Gamma_n^{-1} \beta_n^* C_n^{-1} \left[ (\rho^B H)_{nm} + (\rho^C d_c)_{nm} \right] \quad (14b)$$

Again, the  $T_e$  of the lithosphere is needed to apply Eq. (14a).

#### 4.1.7. Lithospheric stress modelling

In the 1960s, early satellite missions provided crucial data that led to the development of the first low-degree EGMs. These models were instrumental in various scientific investigations, shedding light on the global mantle convection pattern and its intricate connection with tectonic plate configurations and lithospheric stresses.

**4.1.7.1. Sub-lithospheric stress.** Kaula (1963) pioneered a groundbreaking approach focused on minimising the strain energy. His methodology leveraged low-degree gravitational and topographic harmonics to unveil the subtlest stresses within the Earth's elastic structure. Runcorn (1967) contributed a pivotal functional relationship connecting stress and gravity fields. His method, based on solving the Navier–Stokes equations, adopted a two-layered Earth model with a lithosphere overlying a mantle of uniform viscosity. Runcorn's work harnessed low-degree spherical harmonics of the Earth's gravity field to unveil a profound correlation with plate tectonic theory's convergent and divergent zones. McKenzie (1967) delved into mantle dynamics by studying heat flow within the mantle, using gravity anomalies as a vital source of information. Marsh and Marsh (1976) made significant strides in the field by developing a 2-D mantle convection model that integrated global gravity anomalies, enhancing our understanding of the Earth's internal processes. Liu (1978) extended Runcorn's theory, constructing detailed stress maps that elucidated the impact of convection-generated stresses on the movement of tectonic plates. McNutt (1980) contributed to the field by interpreting stresses within the Earth's crust and upper mantle, utilising regional gravity data. Fu and Huang (1983) further refined Runcorn's work, extending the definition of the stress tensor. Ricard et al. (1984) investigated the relationship between lithospheric stresses and geoid heights, providing valuable insights into Earth's dynamic processes. Eshagh (2014) modified Runcorn's theory to accommodate

satellite gradient data, continuing the tradition of refining our understanding of Earth's complex systems.

However, the direct modelling of mantle convection pattern or stresses solely from gravity data faces significant challenges due to the lack of a unique solution. Furthermore, criticisms have been raised regarding certain approximations in Runcorn's theory, such as the omission of the toroidal component in mantle flow. To address these issues, Hager and O'Connell (1981) developed a solution for mantle flow that considered plate velocity models, radially variable viscosity, and both poloidal and toroidal flows in the mantle. Steinberger et al. (2001) applied this method to investigate global lithospheric stress patterns driven by global mantle circulation, while Medvedev (2016) inferred stress patterns within the African tectonic plate by combining methods for modelling thermal processes and gravitational potential energy. Hager and O'Connell's solution, based on mantle flow equations, requires information on mantle density anomalies typically inferred from seismic tomography. Ricard et al. (1984) and Richards and Hager (1984) proposed the use of the global geoid model to constrain radial viscosity structures for solving Hager and O'Connell's theory, effectively incorporating gravity information into mantle flow solutions.

In the light of these developments, a novel approach has been proposed that combines Runcorn's gravimetric solutions with Hager and O'Connell's mantle flow solutions. This approach, employing a least-squares method, jointly solves both types of observation equations, promising further insights into the complex interplay of Earth's internal dynamics.

The study of mantle convection can be facilitated through the analysis of the long-wavelength structure of the Earth's gravity field. By solving the Navier-Stokes equations of convection under certain assumptions, such as constant viscosity, negligible toroidal flow, and a Newtonian mantle, Runcorn (1967) derived mathematical relationships that express the shear stress at the base of the lithosphere resulting from mantle convection.

$$\begin{pmatrix} \tau_{xx} \\ \tau_{yy} \end{pmatrix} = \frac{g}{4\pi G(R - D_{Lith})} \sum_{n=2}^{\infty} \frac{2n+1}{n+1} \left( \frac{R}{R - D_{Lith}} \right)^{n+1} \sum_{m=-n}^n t_{nm} \begin{pmatrix} \frac{\partial Y_{nm}(\theta, \lambda)}{\partial \theta} \\ \frac{\partial Y_{nm}(\theta, \lambda)}{\sin\theta \partial \lambda} \end{pmatrix} \quad (15a)$$

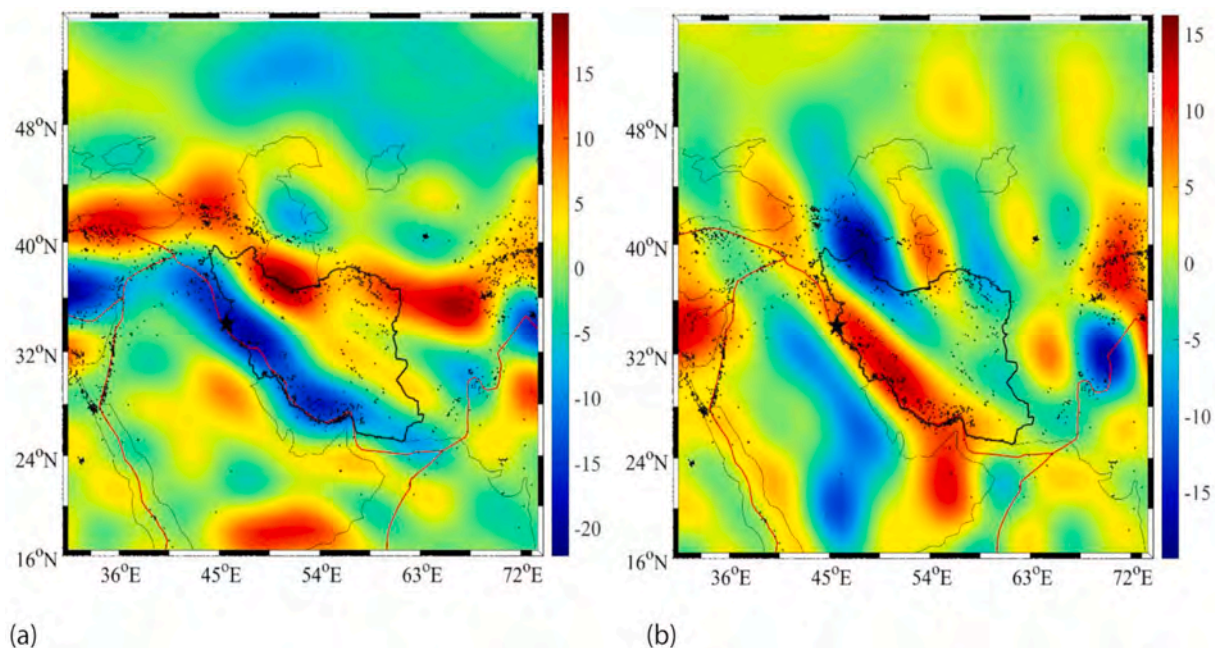


Fig. 7. The sub-lithospheric shear stresses components: a)  $\tau_{xx}$  and b)  $\tau_{yy}$  [MPa] (Eshagh et al., 2020a, 2020b).

where  $\tau_{zx}$  and  $\tau_{zy}$  are the shear-stresses at the base of the lithosphere toward north and east, respectively, and  $D_{\text{Lith}}$  is the depth of the boundary between the lithosphere and mantle.

In Liu (1978), the harmonic degrees between 13 and 25 were suggested to reduce the contributions from the core and lithosphere. However, Stewart and Watts (1997) considered the harmonic degrees below 15 to be contributions from the sub-lithosphere.

Eshagh et al. (2018) compared two sub-lithospheric stress modelling approaches: one following Hager and O'Connell's mantle flow equations and the other based on Runcorn's theory with gravity data, using a least-squares analysis focused on the South American lithosphere. Their findings showed Hager and O'Connell's method pinpointing maximum stress under the northern Andes, while Runcorn's highlighted stress along subduction zones and margins. Combining these methods yielded results closely aligned with Hager and O'Connell's approach.

Eshagh (2020) applied GRACE and GRACE-FO satellite gravity data to study lithospheric deformations, exemplified by analysing the Sar-e-Pol Zahab 2018 earthquake stress redistribution in Iran; see Fig. 7a and b. The study included maps of sub-lithospheric shear stresses computed at lithospheric depths based on the Conrad and Lithgow-Bertelloni model (Conrad and Lithgow-Bertelloni, 2006) over Iran, demonstrating the method's practicality. One issue in applying Eq. (18a) is the choice of a maximum degree of expansion based on the lithospheric depth. When the base of the lithosphere is deeper, this degree should be lower and vice versa.

4.1.7.2. *Stress propagation through the lithosphere from its base.* By considering the lithosphere as an elastic shell, one can utilise the solution to the spherical boundary-value problem in elasticity to describe how stress is distributed within the lithosphere (Liu, 1983; Fu and Huang, 1990). While it is possible to derive a general solution for displacement within the lithospheric shell, the strain tensor can be deduced from this displacement field, enabling the determination of overall stress tensor solutions. To find specific solutions, it was assumed that shear stresses exist at the base of the lithospheric shell as lower boundary values, while stress at the upper boundary is negligible. The stress tensor components, derived using this approach, are defined as follows:

$$\tau_{zz} = \frac{1}{r} \sum_{n=2}^{\infty} (\tilde{\lambda}K_n^1 + 2\tilde{\mu}K_n^2) \sum_{m=-n}^n t_{nm} Y_{nm}(\theta, \lambda) \quad (16a)$$

$$\tau_{xx} = \frac{1}{r} \sum_{n=2}^{\infty} \sum_{m=-n}^n t_{nm} \left[ (\tilde{\lambda}K_n^1 + 2\tilde{\mu}K_n^3) Y_{nm}(\theta, \lambda) + 2\tilde{\mu}K_n^5 \frac{\partial^2 Y_{nm}(\theta, \lambda)}{\partial \theta^2} \right] \quad (16b)$$

$$\tau_{yy} = \frac{1}{r} \sum_{n=2}^{\infty} \sum_{m=-n}^n t_{nm} \left\{ (\tilde{\lambda}K_n^1 + 2\tilde{\mu}K_n^3) Y_{nm}(\theta, \lambda) + 2\tilde{\mu}K_n^5 \left[ \frac{1}{\sin^2 \theta} \frac{\partial^2 Y_{nm}(\theta, \lambda)}{\partial \lambda^2} + \cot \theta \frac{\partial Y_{nm}(\theta, \lambda)}{\partial \theta} \right] \right\} \quad (16c)$$

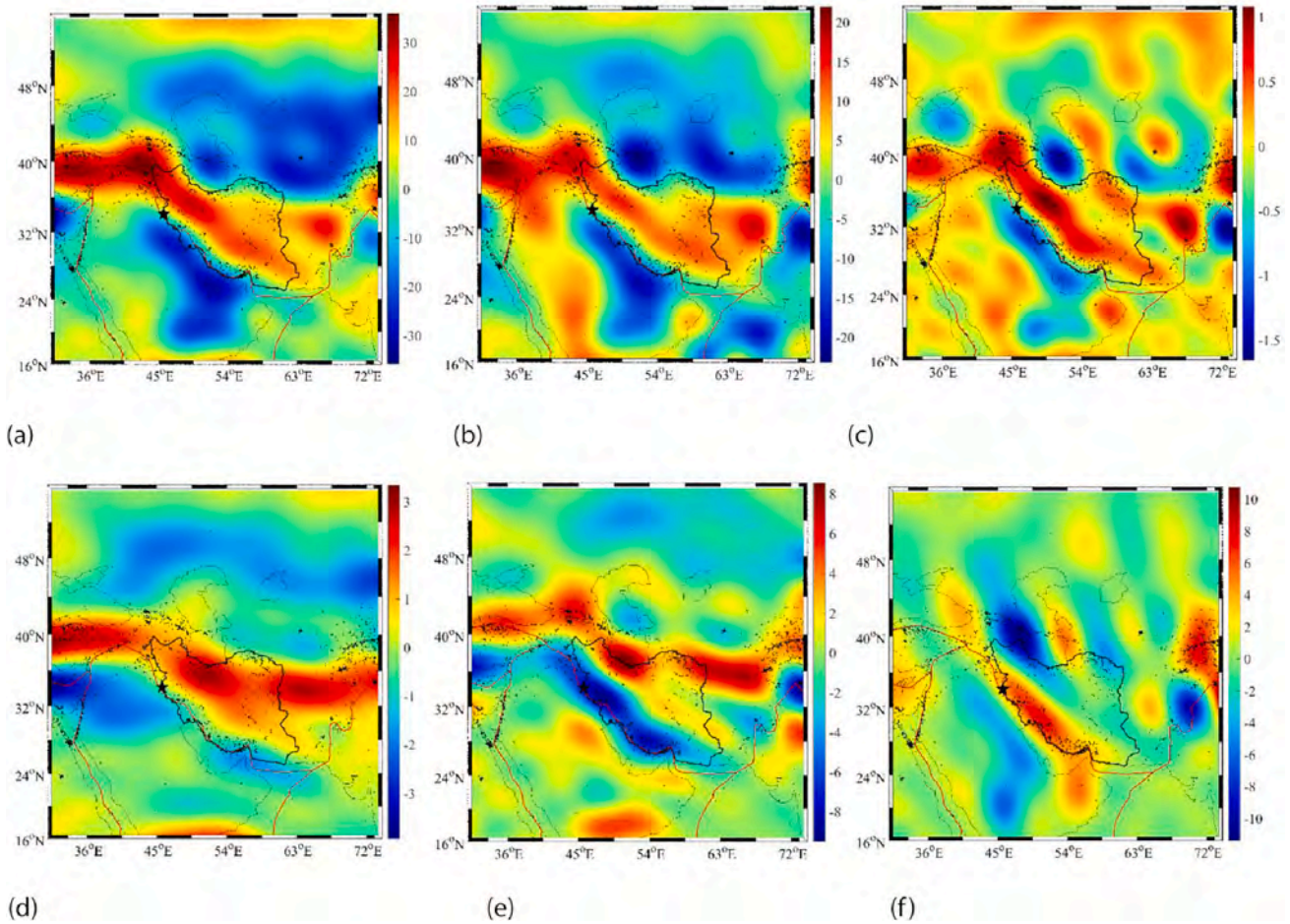


Fig. 8. The stress tensor components of the earthquake at the depth of 10 km occurred in 25th of November 2018 with the magnitude of 6.3, the epicentre (34.361° N, 45.744° E) near the town Sar-e-Pol Zahab in West Iran: a)  $\tau_{xx}$  b)  $\tau_{yy}$  c)  $\tau_{zz}$  d)  $\tau_{zx}$  e)  $\tau_{yz}$  and f)  $\tau_{xy}$  [MPa]. The star is the earthquake epicentre and the small dots are the distribution of seismic points.

$$\tau_{xz} = \frac{\tilde{\mu}}{r} \sum_{n=2}^{\infty} \sum_{m=-n}^n t_{nm} K_n^4 \frac{\partial Y_{nm}(\theta, \lambda)}{\partial \theta} \quad (16d)$$

$$\tau_{yz} = \frac{\tilde{\mu}}{r \sin \theta} \sum_{n=2}^{\infty} \sum_{m=-n}^n t_{nm} K_n^4 \frac{\partial Y_{nm}(\theta, \lambda)}{\partial \lambda} \quad (16e)$$

$$\tau_{xy} = \frac{\tilde{\mu}}{r \sin \theta} \sum_{n=2}^{\infty} \sum_{m=-n}^n t_{nm} K_n^4 \left( \frac{\partial^2 Y_{nm}(\theta, \lambda)}{\partial \theta \partial \lambda} - \cot \theta \frac{\partial Y_{nm}(\theta, \lambda)}{\partial \lambda} \right) \quad (16f)$$

where  $\tilde{\mu}$  and  $\tilde{\lambda}$  are the elasticity coefficients, which can be determined from seismic data. More details on computation of the coefficients can be found in, e.g., (Eshagh, 2020).

Fig. 8 shows the stress tensor components computed based on the above theory and using the GRACE-FO data for an earthquake at the depth of 10 km occurred in 25th of November 2018 with the magnitude of 6.3, the epicentre (34.361° N, 45.744° E) near the town Sar-e-Pol Zahab in West Iran close to the border with Iraq. The stress tensor has been determined from the GRACE-FO monthly solution in October 2018 (Eshagh et al., 2020a, 2020b).

#### 4.1.8. Earth's centre of mass and dipole moment

The Earth's centre of mass and its associated dipole moment play crucial roles in understanding our planet's gravitational field. The centre of mass represents the balance point of Earth's mass distribution, and it is typically located at the geometric centre of the Earth, very close to its physical centre. Surface mass redistribution within the Earth system, especially in the atmosphere, oceans, continents, and ice sheets, causes the position of the centre of mass to vary in a reference frame attached to the solid Earth.

Decades of research have significantly enhanced our understanding of geocentre motion, impacting Earth's geodesy and reference frames. Initial studies, such as Dong et al. (1997), identified annual and semi-annual geocentre variations influenced by atmospheric, oceanic, and groundwater changes. Subsequent research, including Wu et al. (1999) using satellite laser ranging and Bouillé et al. (2000) combining DORIS and laser data, pinpointed these variations with increasing precision and linked them to mass redistributions. Lavallée et al. (2006) improved modelling accuracy using GPS, while Guo et al. (2008) and Swenson et al. (2008) furthered this understanding through CHAMP and GRACE satellite data, respectively. Wu et al. (2012) emphasised advances in geophysical modelling impact on the International Terrestrial Reference Frame (ITRF). Cheng et al. (2013) showed SLR-observed geocentre variations align with multiple data sources, including GPS and GRACE. Enhanced methods by Wu et al. (2017) and Rzeghi et al. (2019) integrated various satellite data for improved geocentre motion estimation and its implications, notably in water storage dynamics and global mass shifts.

The concept of the dipole moment arises from the uneven Earth's mass distribution. This non-uniform distribution creates variations in the gravitational field strength across the planet's surface. As a result, the Earth's gravitational field can be approximated as a dipole field, akin to the field generated by a bar magnet with the North and South Pole. In the case of Earth, one pole of this gravitational dipole aligns approximately with the North Pole, while the other aligns with the South Pole. It helps us understand variations in Earth's gravitational field, which in turn reveal information about the planet's interior structure and dynamic processes.

The first-degree harmonics have a direct connection to the Earth's centre of mass. The spherical harmonic expansion of the gravitational field only for degree  $n = 1$  reads

$$V_1 = \sum_{m=-1}^1 \left( \frac{R}{r} \right)^2 v_{1m} Y_{1m}(\theta, \lambda) = \frac{GMR}{r^2} (\bar{C}_{10} \cos \theta + \bar{C}_{11} \sin \theta \cos \lambda + \bar{S}_{11} \sin \theta \sin \lambda) \quad (17a)$$

where  $\bar{C}_{10}$ ,  $\bar{C}_{11}$ , and  $\bar{S}_{10}$  are the fully-normalised spherical harmonic

coefficients of the Earth's gravitational field.

The coordinates of the Earth's centre of mass  $X_0$ ,  $Y_0$ , and  $Z_0$  are functionally related with the first-degree spherical harmonic coefficients  $\bar{C}_{10}$ ,  $\bar{C}_{11}$ , and  $\bar{S}_{10}$  as follows (Guo et al., 2008)

$$(X_0 \ Y_0 \ Z_0) = R\sqrt{3}(\bar{C}_{11} \ \bar{S}_{11} \ \bar{C}_{10}) \quad (17b)$$

However, in practice, when a geocentric coordinate system is considered in modelling of the gravitational potential, there is no shift from the centre of the mass of the Earth. This means that the first-degree spherical harmonic coefficients are zero.

This dipole component arises from the Earth's uneven mass distribution. Essentially, it is as if Earth's masses were slightly shifted toward one end, creating a gravitational dipole. The dipole moment for  $r = R$  is defined by (Vermeer, 2020; p. 67)

$$V_1 = \frac{GM}{R^2} [\bar{C}_{11} \ \bar{S}_{11} \ \bar{C}_{10}] \begin{bmatrix} R \sin \theta \cos \lambda \\ R \sin \theta \sin \lambda \\ R \cos \theta \end{bmatrix} = \frac{GM}{R^2} \mathbf{d} \cdot \begin{bmatrix} R \sin \theta \cos \lambda \\ R \sin \theta \sin \lambda \\ R \cos \theta \end{bmatrix} \quad (17c)$$

$\mathbf{d}$  is the dipole moment  $\mathbf{d} = (\bar{C}_{11} \ \bar{S}_{11} \ \bar{C}_{10})$ , which means that the first-degree spherical harmonic coefficients  $\bar{C}_{10}$ ,  $\bar{C}_{11}$ , and  $\bar{S}_{10}$  represent the dipole moments of the Earth's gravitational field.

#### 4.1.9. Earth's tensor of inertia

The Earth's tensor of inertia is a valuable tool for understanding how mass is distributed within our rotating planet. Marchenkov and Schwintzer (2003) undertook an ambitious project to estimate the Earth's dynamic figure, which encompasses essential parameters like the principal axes and principal moments of inertia. To achieve this, they leveraged satellite-derived gravitational harmonic coefficients, specifically those of the second degree, which are crucial components of global Earth gravity models. Additionally, they incorporated data on the dynamic ellipticity, obtained from the precession constant observed through the very long-baseline interferometry (VLBI). Their approach involved the development of precise mathematical formulas for calculating these parameters, with a strong emphasis on solving the eigenvalue-eigenvector problem accurately while rigorously addressing error propagation.

Chen and Shen (2010), on the other hand, set out to construct a comprehensive theory that could describe the intricate rotational dynamics of our planet. Their approach began with a re-evaluation of the Earth's inertia tensor, drawing data from two gravity models, European Improved Gravity model of the Earth by New techniques-GRACE/LAGEOS 05 Combined (EIGEN-GL05C, Förste et al., 2008) and Earth Gravity Model 2008 (EGM2008, Pavlis et al., 2012). They proceeded to formulate dynamic equations and deduce the normal modes for an Earth model that took into the account several perturbing factors. This model featured a triaxial anelastic mantle, a triaxial fluid core, and dissipative oceans. Their calculations successfully retrieved the periods of significant phenomena such as the Chandler wobble and the free core nutation, which amounted to approximately 433 and 430 mean solar days, respectively. Beyond this, the researchers ventured into deriving Liouville equations and their general solutions for the triaxial nonrigid Earth. These equations were characterised by intricate, frequency-dependent transfer functions that encompassed the influences of triaxialities, deformations in the mantle and core, mantle anelasticity, equilibrium, and dissipative ocean tides.

Zhang and Shen (2020) introduced a rigorous approach aimed at calculating the principal inertia moments (PIMs) of different layers within a triaxial three-layered Earth. This approach marked a departure from previous methods that made the simplifying assumption of alignment among principal inertia axes. Instead, they embraced a tensor transformation rule to conduct precise calculations. These newly estimated PIMs were then integrated into the theory of Earth rotation for a triaxial three-layered Earth, accounting for various coupling effects.

Their numerical calculations yielded intriguing results: the periods of the Chandler Wobble (CW), Free Core Nutation (FCN), Free Inner Core Nutation (FICN), and Inner Core Wobble (ICW) were approximately 433.0, 430.8, 943.9, and 2735.9 mean solar days, respectively. Remarkably, these findings closely paralleled accepted values within the geoscience community. This more accurate estimation of PIMs holds significant promise for refining our understanding of critical physical parameters within the Earth's interior.

It is defined as a function of the second-degree spherical harmonic coefficients of the Earth's gravitational field, so that

$$V_2 = \sum_{m=-2}^2 v_{2m} Y_{2m}(\theta, \lambda) = \frac{GMR^2}{r^3} \sum_{m=0}^2 (\bar{C}_{2m} \cos m\lambda + \bar{S}_{2m} \sin m\lambda) \bar{P}_{2m}(\cos\theta) \quad (18a)$$

These second-degree harmonics have the major role in the determining the Earth's tensor of inertia (Vaníček, 1976)

$$I = \begin{bmatrix} A & -D & -E \\ -D & B & -F \\ -E & -F & C \end{bmatrix} \quad (18b)$$

The diagonal components of the Earth's inertia tensor in Eq. (18b), called the principal moments of inertia, are defined by (Marchenkov and Schwintzer, 2003)

$$A = \frac{\sqrt{15}}{2} \left( \Lambda_3 - \frac{\Lambda_3}{H_D} - \frac{\Lambda_1 - \Lambda_2}{3} \right) \quad (18c)$$

$$B = \frac{\sqrt{15}}{2} \left( \Lambda_3 - \frac{\Lambda_3}{H_D} + \frac{\Lambda_1 - \Lambda_2}{3} \right) \quad (18d)$$

$$C = -\frac{\sqrt{15}}{2H_D} \Lambda_3 \quad (18e)$$

where

$$\Lambda_i = (-1)^{i+1} 2 \sqrt{\frac{\bar{C}_{20}^2 + \bar{C}_{21}^2 + \bar{S}_{21}^2 + \bar{C}_{22}^2 + \bar{S}_{22}^2}{3}} \sin\left(\frac{\phi + \theta}{3}\right), \text{ for } \theta = \begin{cases} \pi & i = 1 \\ 0 & i = 2 \\ -\pi & i = 3 \end{cases} \quad (18f)$$

$$\phi = \sin^{-1} \left( \frac{3}{2} \sqrt{3} (\bar{C}_{20}^2 + \bar{C}_{21}^2 + \bar{S}_{21}^2 + \bar{C}_{22}^2 + \bar{S}_{22}^2)^{-\frac{3}{2}} q \right) \quad (18g)$$

$$q = \frac{2\bar{C}_{20}^3}{3\sqrt{3}} + \frac{\bar{C}_{20}}{\sqrt{3}} (\bar{C}_{21}^2 + \bar{S}_{21}^2 - 2\bar{C}_{22}^2 - 2\bar{S}_{22}^2) + \bar{C}_{22} (\bar{C}_{21}^2 - \bar{S}_{21}^2) + 2\bar{C}_{21} \bar{S}_{21} \bar{S}_{22} \quad (18h)$$

The off-diagonal elements or shear moments of the Earth's inertia read (Vaníček, 1976)

$$D = -\frac{2R^3}{G} \bar{S}_{22}, E = -\frac{R^3}{G} \bar{C}_{21} \text{ and } F = -\frac{R^3}{G} \bar{S}_{21} \quad (18i)$$

As Eqs. (18c)-(18i) show for computing the Earth's tensor of inertia only the second-degree spherical harmonic coefficients of the Earth's gravitational field are needed. In Eq. (18f),  $i$  means the number of axes of the three direction of the Earth's natural coordinate system, which are defined by the direction of the principle moments of inertia of the Earth.  $\phi$  and  $q$  are constants and do not depend on the directions. Note that for computing  $A$ ,  $B$  and  $C$  the dynamic ellipticity of the Earth  $H_D = 0.0032737875 \pm 0.0000000005$  (Mathews, 2000) or  $0.0032737634 \pm 0.0000000032$  (Chen and Shen, 2010) is needed, which can be obtained from other space geodetic methods like Very Long Baseline Interferometry (VLBI). Chen and Shen (2010) estimated  $A = 8.0100829 \pm 0.0000084$ ,  $B = 8.0102594 \pm 0.0000084$ ,  $C = 8.0364807 \pm 0.0000084$

in unit of  $10^{-37} \text{ kg m}^2$  using zero-tide EGM2008 (Pavlis et al., 2012).

The orientations of axes of the Earth's inertia coordinate system are defined by the spherical position of the points through, which these axes pass through (Chen et al., 2016a, 2016b)

$$\lambda_i = \tan^{-1} \frac{m_i}{l_i} \quad (19a)$$

$$\theta_i = \tan^{-1} \frac{n_i}{\sqrt{l_i^2 + m_i^2}} \quad (19b)$$

where  $\theta_i, \lambda_i$  are the coordinates of the point that the  $i$ -th axis of the inertia coordinate system passes through, and

$$n_i = \left[ 1 + u_i^2 + \left( \frac{\bar{S}_{21} - A_i + \frac{2}{\sqrt{3}} \bar{C}_{20}}{\bar{C}_{21}} \right)^2 \right]^{\frac{1}{2}} \quad (19c)$$

$$u_i = \frac{\bar{C}_{21} \bar{S}_{21} + \bar{S}_{22} \left( A_i - \frac{2}{\sqrt{3}} \bar{C}_{20} \right)}{\bar{S}_{21} \bar{S}_{22} + \bar{C}_{21} \left( A_i + \bar{C}_{22} + \frac{1}{\sqrt{3}} \bar{C}_{20} \right)} \quad (19d)$$

$$l_i = \frac{n_i}{C_{21}} \left( A_i - \frac{2}{\sqrt{3}} \bar{C}_{20} - \bar{S}_{21} u_i \right) \quad (19e)$$

$$m_i = u_i n_i \quad (19f)$$

where  $i = A, B$  or  $C$ .

Zhang and Shen (2020) estimated the latitude and longitudes of the directions of moment of inertia of the Earth using EIGEN-6C4 (Förste et al., 2014):

$$\lambda_A = -14.928962 \pm 0.000004, \varphi_A = -0.00004796 \pm 0.00000002$$

$$\lambda_B = 75.071038 \pm 0.000004, \varphi_B = 0.00009093 \pm 0.00000002$$

$$\lambda_C = -77.115266 \pm 0.0123557, \varphi_C = 89.99989720 \pm 0.00000002$$

The average coordinate of the North Pole, or in fact its deviation from the 3rd axis of the inertia coordinate system, can be derived from the second-degree spherical harmonic coefficients as follows (Marchenkov and Schwintzer, 2003).

$$\bar{x}_p = \frac{(\sqrt{3} \bar{C}_{20} + \bar{C}_{22}) \bar{C}_{21} + \bar{S}_{22} \bar{S}_{21}}{3\bar{C}_{20}^2 - \bar{C}_{22}^2 - \bar{S}_{22}^2} \quad (19g)$$

$$\bar{y}_p = -\frac{(\sqrt{3} \bar{C}_{20} - \bar{C}_{22}) \bar{S}_{21} + \bar{S}_{22} \bar{C}_{21}}{3\bar{C}_{20}^2 - \bar{C}_{22}^2 - \bar{S}_{22}^2} \quad (19h)$$

#### 4.1.10. Precision-nutation angles

The precision-nutation angles are critical parameters in studies of the Earth's rotation, and they play a fundamental role in geodetic and astrometric applications. These angles describe the subtle wobbling and oscillation of the Earth's rotational axis, which occur due to various factors, including gravitational interactions with celestial bodies and an uneven distribution of masses within the Earth. Precision-nutation angles are crucial for accurately tracking and predicting positions of celestial objects and for understanding Earth's rotational behaviour. One of the methods for determining these angles involves utilising information from the Earth's gravity field.

Bourda and Capitaine (2004) investigated how the Earth's precession and nutation are influenced by variations in the geopotential's second-degree zonal coefficient  $C_{20}$ . These variations have been observed through precise satellite measurements. Their study explored how the  $C_{20}$  variations impact precession and nutation models, aiming

for micro-arc-second accuracy, as required by current Earth's orientation determinations by VLBI. However, they acknowledged uncertainties in theoretical models of the second-degree zonal coefficient, which can limit the accuracy of precession-nutation predictions. To address this, they used data collected by the Groupe de Recherches en Géodésie Spatiale (GRGS) from 1985 to 2002 to assess the effects of  $C_{20}$  variations on the Earth's dynamical flattening and discuss their incorporation into precession-nutation modelling. They stipulated that monitoring of the periodic  $C_{20}$  variations can help predict their impact on periodic precession-nutation motions, though comprehensive observations are essential for accurate  $C_{20}$  rate estimation.

The precision-nutation angles can be determined from the second zonal spherical harmonic coefficient  $C_{20}$ . Generally, the precision angles can be derived by solving the following differential equations (Capitaine et al., 2003; Bourda and Capitaine, 2004)

$$\sin\omega_A\dot{\psi}_A = r_\psi \sin\epsilon_A \cos\chi_A - r_\psi \sin\chi_A \quad (20a)$$

$$\dot{\omega}_A = r_\epsilon \cos\chi_A - r_\psi \sin\epsilon_A \sin\chi_A \quad (20b)$$

where  $r_\psi$  and  $r_\epsilon$  are, respectively, the precision rates in longitude and obliquity of the ecliptic,  $\epsilon_A$  is the obliquity of the ecliptic, and  $\chi_A$  is the planetary precision angle determining the precision of ecliptic.

The solution of differential equations in Eqs. (20a) and (20b) is provided in terms of the  $\psi_A$  and  $\omega_A$  angles. The precision rate in longitude and obliquity are defined by (see Capitaine et al., 2003 for details)

$$r_\psi = r_0 + r_1 t + r_2 t^2 + r_3 t^3 \quad (20c)$$

$$r_\epsilon = u_0 + u_1 t + u_2 t^2 + u_3 t^3 \quad (20d)$$

where  $\{r_i; i = 0, 1, 2, 3\}$  are constant coefficients (Capitaine et al., 2003), and  $r_0$  is significantly larger than the rest of them. The first luni-solar term of Eq. (20c) can be approximately defined as follows:

$$r_\psi \approx f_{LS} \cos\epsilon_0 \quad (20e)$$

where the obliquity of the ecliptic  $\epsilon_0$  is defined at the Julian epoch at J2000. The parameter  $f_{LS}$  in Eq. (20e) is given by

$$f_{LS} = \frac{3H^*}{\bar{\omega}} \left( \frac{M_M M_0}{M_M + M_S} \frac{n_M^2}{F_2^2} + \frac{M_S S_0 n_S^2}{M_M + M_S + M} \right) \quad (20f)$$

where  $\bar{\omega}$  is the Earth's rotation rate,  $H^*$  is the dynamic flattening,  $M_M$  and  $M_S$  are the masses of the Moon and the Sun, respectively,  $n_M$  is the mean motion of the Moon around the Earth,  $n_S$  is the mean motion of the Earth around the Sun,  $M_0 = 496,303.66 \times 10^{-6}$ ,  $S_0 = 500,210.62 \times 10^{-6}$  (Souhay and Kinoshita, 1996; Bourda and Capitaine, 2004), and  $F_2 = 0.999093142$  (Kinoshita, 1977) is the factor for the mean distance of the Moon.

The relationship between the dynamic flattening of the Earth and the fully-normalised second-degree zonal spherical harmonic coefficient of the Earth's gravitational field reads (Lambeck, 1988)

$$H^* = -\sqrt{5} \frac{MR^2}{C} \bar{C}_{20} \quad (20g)$$

and

$$\frac{MR^2}{C} = \frac{3}{2} \left( 1 - \frac{2}{5} \sqrt{1 + \eta} \right)^{-1} \quad (20h)$$

where  $\eta = 5q/2f - 2$  and  $q = \bar{\omega}^2 R^3 / GM$ .

The computational procedure of deriving the angles  $\psi_A$  and  $\omega_A$  is following: first, the dynamic flattening of the Earth is computed according to Eqs. (20h) and (20g), and then inserted into Eq. (20f). After computing  $r_0$ , it is inserted to the differential Eqs. (20a) and (20b) to get the angles  $\psi_A$  and  $\omega_A$ .

We understand that polynomial expressions based on time exist for

these parameters. However, our objective was to demonstrate how these angles can be calculated using gravity data. Notably,  $\bar{C}_{20}$  plays a crucial role in determining the dynamic flattening of the Earth. This dynamic flattening is then instrumental in calculating the longitudinal precession rate, which is referenced in the differential Eqs. (20a) and (20b). It is also important to note that for the remaining parameters in these equations, there are polynomial expressions in time.

#### 4.1.11. Orbit determination

The static gravitational field of the Earth plays a crucial role in determination of satellite orbits, particularly for computing the acceleration vector of a satellite as shown in Eq. (3c). Satellites experience various forces in space, stemming from both gravitational and non-gravitational sources. For detailed mathematical models of these perturbing forces, we refer readers to Seeber (2003), Eshagh and Najafi-Alamdari (2007), and Hofmann-Wellenhof et al. (2011). In an inertial frame, the satellite acceleration vector should be integrated twice with respect to time. This means that the following system of differential equations should be solved:

$$\begin{cases} \dot{\mathbf{r}} = \frac{\partial \mathbf{r}}{\partial t} = [\dot{x} \ \dot{y} \ \dot{z}]^T = [f_1(x, y, z, \Delta t) \ f_2(x, y, z, \Delta t) \ f_3(x, y, z, \Delta t)]^T \\ \ddot{\mathbf{r}} = \frac{\partial \dot{\mathbf{r}}}{\partial t} = [\ddot{x} \ \ddot{y} \ \ddot{z}]^T = [f_4(x, y, z, \Delta t) \ f_5(x, y, z, \Delta t) \ f_6(x, y, z, \Delta t)]^T \end{cases} \quad (21a)$$

where  $f_i(x, y, z, \Delta t)$ ,  $i = 1, 2, 3, 4, 5, 6$  are the functions presenting the velocity and acceleration.  $f_1(x, y, z, \Delta t)$ ,  $i = 4, 5, 6$  contain the gravitational acceleration of satellites as well as all gravitational and non-gravitational perturbations acting on a satellite. In the absence of these perturbations, the acceleration vector is computed in the LNOF, according to Eq. (6b), and later transferred to the CRF. Such a well-known transformation is available in many textbooks e.g. Seeber (2003), Hofmann-Wellenhof et al. (2011). These transformations are because of the effect of precession, nutation, polar motion and rotation around the z-axis to coincide the x-axes of TRF and CRF by a rotation of Greenwich Apparent sidereal Time (GAST). The mathematical models of the orientation angles of these transformations are given in terms of time with respect to J2000 in the aforementioned textbook or International Earth Rotation Service (IERS) technical notes (Petit and Luzum, 2013).

To initiate the integration process, the a priori values for the position and velocity vectors of the satellite are required, which can be derived from other space geodetic techniques. Numerous numerical integration methods exist for solving the system of six differential equations for example, methods of Runge-Kutta, Runge-Kutta-Nyström, Runge-Kutta Fehlberg, which are known as single step approaches, meaning that for predicting the satellite state vector for the next epoch only the previous state vector is needed. Multi-steps methods, which are so-called predictor-corrector methods, use state vectors of previous epochs for predicting the next epoch state vector, e.g. methods of Adam-Bashforth and Adam-Moulton.

In order to show how the integration process is done, we selected the simple method of Runge-Kutta of 4th order, but the principle of applying other integrators is similar. The position and velocity vector elements are computed by:

$$r_i^{k+1} = r_i^k + (K_{1i} + 2K_{2i} + 2K_{3i} + K_{4i})/6 \quad (21b)$$

$$\dot{r}_i^{k+1} = \dot{r}_i^k + (K_{1,i+3} + 2K_{2,i+3} + 2K_{3,i+3} + K_{4,i+3})/6 \quad (21c)$$

where  $r_i^k$ ,  $i = 1, 2, 3$  are the satellite coordinates  $x, y$  and  $z$ , respectively in the CRF at epoch  $k$ , and  $\dot{r}_i^k$ ,  $i = 4, 5, 6$  are the satellite velocities,  $k$  is the epoch number.  $K_{ji,j} = 1, 2, 3$  and 4 are the four coefficients of the integrator. These coefficients can be derived from the following formulae:

$$K_{1i} = \begin{cases} \mathbf{r}^k \Delta t & i = 1, 2, 3 \\ f_i(\mathbf{r}^k, \Delta t) & i = 4, 5, 6 \end{cases} \quad (21d)$$

$$K_{2i} = \begin{cases} \left( \dot{r}_i^k + K_{1,i+3}/2 \right) \Delta t & i = 1, 2, 3 \\ f_i(\mathbf{r}^k + [K_{1,i-3} \ K_{1,i-2} \ K_{1,i-1}]^T / 2, \Delta t) & i = 4, 5, 6 \end{cases} \quad (21e)$$

$$K_{3i} = \begin{cases} \left( \dot{r}_i^k + K_{2,i+3}/2 \right) \Delta t & i = 1, 2, 3 \\ f_i(\mathbf{r}^k + [K_{2,i-3} \ K_{2,i-2} \ K_{2,i-1}]^T / 2, \Delta t) & i = 4, 5, 6 \end{cases} \quad (21f)$$

$$K_{4i} = \begin{cases} \left( \dot{r}_i^k + K_{3,i+3} \right) \Delta t & i = 1, 2, 3 \\ f_i(\mathbf{r}^k + [K_{3,i-3} \ K_{3,i-2} \ K_{3,i-1}]^T, \Delta t) & i = 4, 5, 6 \end{cases} \quad (21g)$$

where  $\mathbf{r} = [r_1 \ r_2 \ r_3]^T = [x \ y \ z]^T$ .

Note that these coefficients depend on the satellite's acceleration vectors, calculated from an EGM and transformed into the CRF. By solving the differential equations presented in Eq. (21a), we estimate the satellite's position and velocity vectors for the next epoch. These estimated vectors are then converted back to the TRF to allow for the use of the EGM in calculating the acceleration. Subsequently, the acceleration vector is transformed into the CRF and numerically integrated. This iterative process is repeated to generate the satellite's complete orbit trajectory.

#### 4.2. Applications of time-variable gravity field

The Earth's gravitational field exhibits variations due to various phenomena. By analysing time-variable gravity data, these phenomena can be studied and analysed. Satellite missions such as GRACE and GRACE-FO (Kornfeld et al., 2019) have been instrumental in this regard. In the following subsections, we present and discuss some phenomena that can be studied by using gravity field variations.

##### 4.2.1. Earthquakes

The detectability of earthquakes using time-variable gravity data relies on factors such as earthquake magnitude, gravimetry resolution, and sensitivity. Monthly gravitational models derived from missions like GRACE and GRACE-FO are essential for examining significant earthquakes. These models enable the visualisation of geoid, gravity, gravity gradients, stress, strain, and even displacements following seismic events. Notably, it is crucial to eliminate or minimise non-earthquake variations, like hydrological signals, from the gravity data/models before conducting earthquake analyses. McCaffrey and Nabelek (1987) investigated the Bali Basin, revealing its formation due to crustal thrusting along the Flores back arc thrust zone. They determined earthquake depths ranging from 10 to 18 km, indicating plate convergence between the Sunda arc and the Indian Ocean plate, resembling early forelands in regions like the Andes. Panet et al. (2007) employed GRACE satellite data to identify co-seismic and post-seismic signatures of Sumatra's 2004 December and 2005 March earthquakes. They observed gravity field reductions over the Andaman Sea and explained them as density changes in the Earth's crust and upper mantle, shedding light on the mantle's viscoelastic response. Hussain et al. (2016) examined changes in gravitational parameters resulting from the October 2005 Kashmir earthquake using time-variable GRACE data. They focused on the gravity anomaly, the geoid, and gravity gradients over the Indo-Pak plate, emphasising the Kashmir earthquake. The study utilised spherical harmonic coefficients of monthly gravity solutions from the GRACE satellite mission, analysed from August to November 2005 after removing hydrological signals. Their results indicated stress accumulation in the northeast direction, closely related to regional geological features and the earthquake. Horizontal gravity gradients

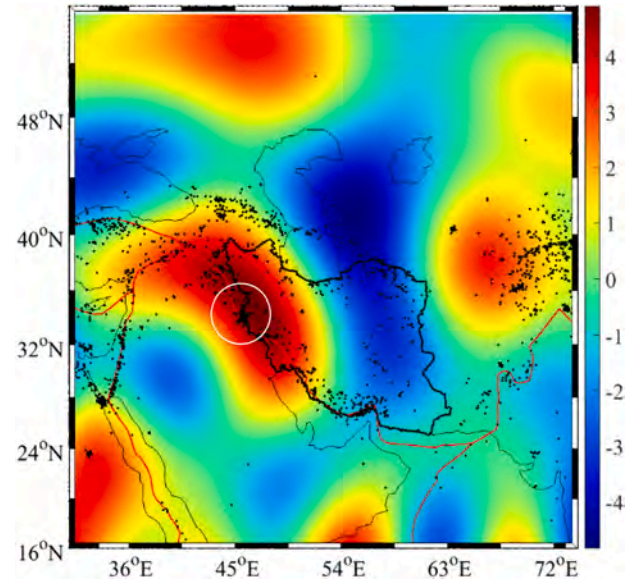


Fig. 9. Changes of the gravity anomalies before and after the Sar-e-Pol Zahab earthquake on 25th November 2018, determined by the GRACE-FO gravity models in December 2018 and January 2019, [ $\mu\text{Gal}$ ]. Black dots are active seismic points and the start the Earthquake epicentre (Eshagh et al., 2020a, 2020b).

proved particularly useful in capturing co-seismic gravity signatures from seismic activity in the region. Chao and Liao (2019) successfully detected earthquake-induced gravity variations using GRACE satellite data, even for earthquakes as low as magnitude Mw 8.3. Their empirical orthogonal function (EOF) analysis unveiled spatial and temporal aspects of seismic events. Anselmi et al. (2020) explored the detectability of earthquake gravity signatures using the Next-Generation Gravity Mission (NGGM), which provided comprehensive Earth coverage. NGGM could estimate earthquake amplitudes for approximately two-thirds of events, including those as low as magnitude 7, highlighting its potential for co- and post-seismic earthquake signatures, particularly for events with a magnitude of at least 7.8.

Additionally, Eshagh et al. (2020a, 2020b) explored the potential of temporal fluctuations in the Earth's gravity field, observed through satellite missions such as GRACE and GRACE-FO, for monitoring lithospheric deformations. While a global network of continuously operating gravity stations remains limited, satellite gravity observations provide valuable insights into long-wavelength lithospheric deformations. To demonstrate the practical applicability of their theoretical model, they applied it to estimate stress and strain redistributions resulting from the 2018 Sar-e-Pol Zahab earthquake in Iran, utilising the GRACE-FO monthly data solutions. Fig. 9 visually represents changes in gravity anomalies they obtained before and after the Zar-e-Pol Zahab Earthquake in the western part of Iran. Positive values are evident across the area, with a particular focus around the earthquake's epicentre indicated by a circle, signifying an increase in gravity. The black dots on the figure correspond to earthquake locations.

##### 4.2.2. Epicentre of shallow earthquakes

Fatolazadeh et al. (2019) delved into the application of GRACE satellite data for pinpointing earthquake epicentres, drawing inspiration from the gravity strain method originally developed by Dermanis and Livireratos (1983). Their research involved a meticulous examination of monthly spherical harmonic coefficients extracted from GRACE observations, which have been adjusted to account for hydrological influences. In their pioneering study introduced the concept of deformation within the Earth's gravity field to estimate invariant components of strain tensors. This innovative approach enabled them to

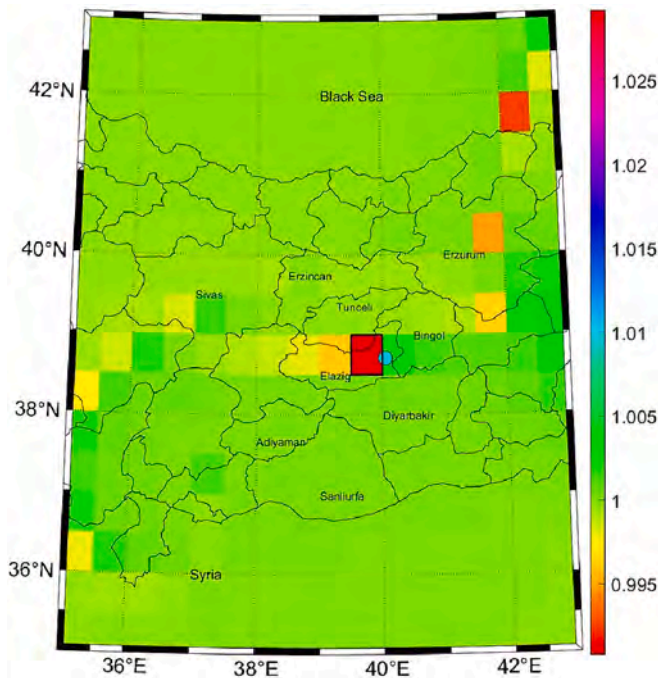


Fig. 10. The position of the eastern Turkey earthquake epicentre detected by the gravity strain approach and USGS.

effectively determine the epicentres of earthquakes that occurred in Iran, China, Turkey, and Nepal between 2003 and 2015. They established a crucial link between the maximum shear strain of the gravity strain tensor and the epicentre locations of shallow earthquakes, building upon the theoretical foundation laid by [Dermanis and Livireratos \(1983\)](#) and treated the geoid as a dynamic surface undergoing deformations, calculating strain values based on its temporal variations. This computed strain is precisely referred to as the gravity strain tensor and is mathematically defined as follows ([Dermanis and Livireratos, 1983](#))

$$\mathbf{S} = \frac{1}{2} (\mathbf{B}^{-1} \mathbf{b} \mathbf{B}^{-1} - \mathbf{I}) \quad (22a)$$

$$\mathbf{B} = \begin{bmatrix} V_{xx}(t_1) & V_{xy}(t_1) & V_{xz}(t_1) \\ V_{xy}(t_1) & V_{yy}(t_1) & V_{yz}(t_1) \\ V_{xz}(t_1) & V_{yz}(t_1) & V_{zz}(t_1) \end{bmatrix}, \quad \mathbf{b} = \begin{bmatrix} V_{xx}(t_2) & V_{xy}(t_2) & V_{xz}(t_2) \\ V_{xy}(t_2) & V_{yy}(t_2) & V_{yz}(t_2) \\ V_{xz}(t_2) & V_{yz}(t_2) & V_{zz}(t_2) \end{bmatrix}. \quad (22b)$$

In fact,  $\mathbf{B}$  and  $\mathbf{b}$  are the gravitational tensors in the LNOF at two epochs of  $t_1$  before and  $t_2$  after deformation.

The dilatation and maximum shear strain of the gravity strain tensor are  $\Delta^* = \lambda_{\max}^{\text{eig}} + \lambda_{\min}^{\text{eig}}$ , and  $\gamma^* = \lambda_{\max}^{\text{eig}} - \lambda_{\min}^{\text{eig}}$ , where  $\lambda_{\max}^{\text{eig}}$  and  $\lambda_{\min}^{\text{eig}}$  are the largest and smallest eigenvalues of the gravity strain tensor.

The gravity strain approach can be used to detect the earthquake location. The situation is illustrated in [Fig. 10](#), where this approach was applied to detect the earthquake that occurred in the eastern Turkey on 2010-03-08 at 7:41:41 UTC and depth of 10 km. The coordinates of its epicentre were 38.709°N and 40.051°E according to the United States Geological Survey (USGS). The map of the maximum shear strain determined from the GRACE monthly gravity models, which was computed from two years of gravity models before and after the earthquake in [Fig. 10](#). The red rectangle is the approximate position of the epicentre estimated from the shear strain maps, which is close to the reported epicentre coordinates by the USGS.

#### 4.2.3. Post-glacial rebound and mantle viscosity

During the ice age, vast glaciers covered the Earth's surface. As the

planet's atmospheric temperature increased, these glaciers began to melt, initiating a process known as a post-glacial rebound or the glacial isostatic adjustment. This phenomenon led to the gradual uplift of the land as it sought to reach an isostatic equilibrium, and these land uplift changes can be tracked by observing shifts in gravity data.

[Ekman and Mäkinen \(1996\)](#) investigated recent postglacial rebound in Fennoscandia, using various data sources such as sea-level data, levelling data, and gravity data. They primarily focused on analysing repeated measurements taken along the Fennoscandian land-uplift gravity line at latitude 63°. Their findings revealed the mass-flow parameter of approximately 0.8, suggesting that uplift models based solely on decompression were inadequate. Instead, they proposed that a viscous inflow of mantle played a critical role in the ongoing uplift process. [Larson and van Dam \(2000\)](#) compared vertical deformation rates obtained from continuous the Global Positioning System (GPS) observations to episodic absolute gravity measurements at four North American sites undergoing postglacial rebound. They recommended continuous GPS observations as a cost-effective and more accurate means of estimating vertical deformation rates compared to periodic gravity measurements. [Velicogna and Wahr \(2002\)](#) explored the potential of the GRACE mission to isolate the postglacial rebound signal, crucial for estimating the Earth's viscosity structure. The study revealed that GRACE data could determine the viscosity of Earth's mantle layers and lithospheric thickness with an accuracy range of  $\pm 30\text{--}40\%$  and  $\pm 15\text{--}20\%$ , respectively. Combining GRACE data with traditional measurements had the potential to significantly enhance worldwide viscosity estimates, especially in the lower mantle. [Paulson et al. \(2007\)](#) used GRACE data to study long-term gravity changes near Hudson Bay and geological measurements of relative sea level (RSL) changes over the past 10,000 years. They found that both the GRACE and RSL data used lacked the capacity to provide insights into mantle viscosity below a depth of 1800 km. The study concluded that the combined GRACE and RSL data could effectively resolve, at most, two layers within the upper 1800 km of the mantle.

By computing the geoid rate from time-variable gravitational models, the rate of land uplift caused by this rebound can be determined as follows (e.g., [Eshagh, 2020](#))

$$\dot{h}(\theta, \lambda) = \frac{\gamma}{4\pi GR} \sum_{n=0}^{\infty} \frac{2n+1}{\kappa_n^*} \sum_{m=-n}^n \Delta \dot{N}_{nm} Y_{nm}(\theta, \lambda) \quad (23a)$$

where  $\Delta \dot{N}_{nm}$  are the spherical harmonic coefficients of the geoid rate, which can be derived by a simple regression to the time-variable geoid models,  $\gamma$  stands for the normal gravity, and

$$\kappa_n^* = \rho^c + \Gamma_n^{-1} \Delta \rho \quad (23b)$$

All parameters in Eq. (23b) have been presented in [Section 4.1.3](#).

Removal of the effect of hydrological signal from the time-variable gravity models prior of applying Eq. (23a) is mandatory. [Fig. 11a](#) shows the geoid rates, ranging from  $-0.6$  to  $0.4$  mm/yr, obtained from the GRACE time-variable gravitational models, reduced for the hydrological signals by using the Global Land data Assimilation System (GLDAS) ([Rodell et al., 2004](#)) model over Fennoscandia. The uplift rate computed according to Eq. (23a) is shown in [Fig. 11b](#). It shows that the land uplift ranges from  $-4$  to  $9$  mm/yr with the maximum around the centre of Gulf of Bothnia. Filtering the results is of vital importance to obtain meaningful results. This land uplift model has a good agreement with a similar model computed from GNSS data over Fennoscandia ([Vestøl et al., 2019](#)).

[Bjerhammar et al. \(1980\)](#) introduced techniques of estimating the mantle viscosity from geodetic observations by identifying the highest correlation between the land uplift information and the geoid computed within a degree range from 10 to 70 ([Sjöberg, 1983](#)). Building upon this, [Sjöberg and Bagherbandi \(2013\)](#) expanded the analysis by considering spherical harmonic degrees up to 23 instead of 70. Specifically, they focused on degree 23, establishing a correlation between the geoid,

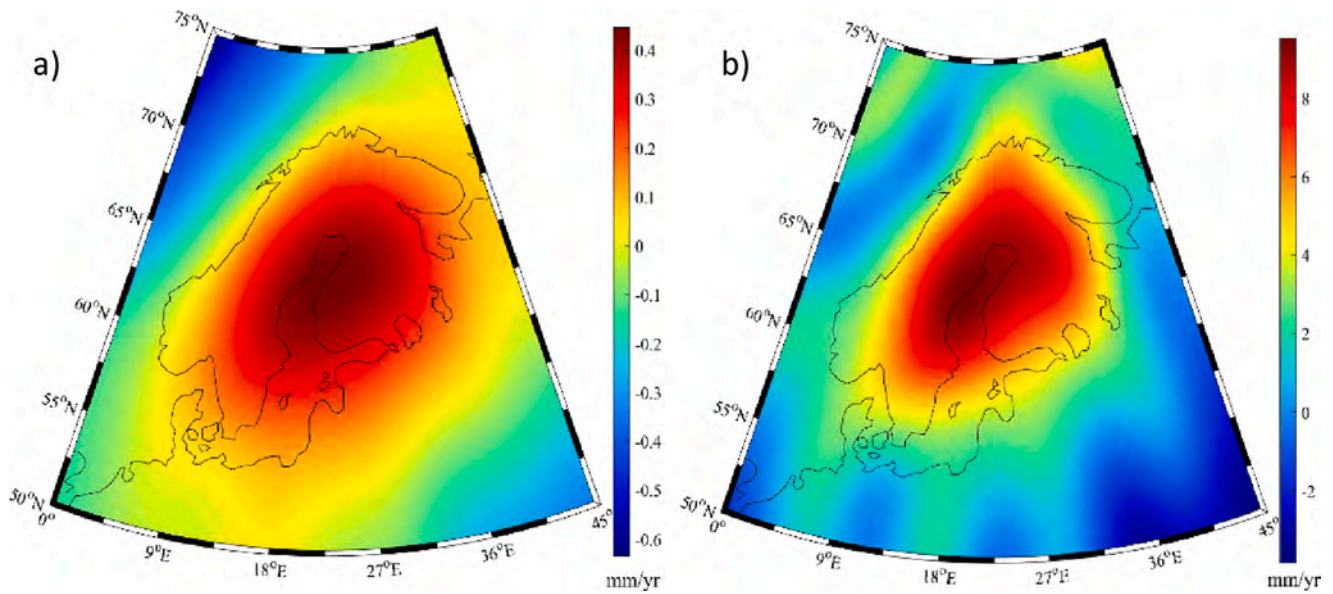


Fig. 11. a) Geoid trend during 15 years of GRACE mission, b) land uplift model determined from the geoid rate of change (Eshagh, 2021).

calculated at various maximum degrees, and the land uplift model derived from GNSS measurements. Furthermore, Shafiei Joud et al. (2017) delved into the frequency range of the geoid signal influenced by the post-glacial rebound. Their research suggested that this frequency range is confined to degrees ranging from 10 to 23. If we accept this hypothesis, the method proposed by Eshagh (2020) can be employed to determine the viscosity of the upper mantle. This method can be summarised as follows:

$$\tilde{\eta} = -\frac{\gamma^2 \rho_m}{4\pi G \dot{h}(\theta, \lambda)} \sum_{n=10}^{23} \frac{2n+1}{\kappa_n^* \left(2n+4+\frac{3}{n}\right)} \sum_{m=-n}^n N_{nm} Y_{nm}(\theta, \lambda) \quad (23c)$$

where  $\rho_m$  is the upper mantle density, taken, e.g., from the CRUST1.0 model. The mean viscosity of the upper mantle is  $5.0 \pm 0.2 \times 10^{21}$  Pa, and in the case of using Eq. (23c), this value is  $6.0 \pm 0.3 \times 10^{21}$  Pa over Fennoscandia (Eshagh, 2020).

#### 4.2.4. Earth rotation and length-of-day excitation

The Earth Orientation Parameters (EOP), including the polar motion ( $X$  and  $Y$ ) and the length-of-day (LOD) are changing from seconds to decades of years. For time scales of a few years or less, the Earth's rotational changes are mainly driven by the mass redistribution in the atmosphere, oceans, and hydrosphere. However, accurate estimation of the Earth's surface fluids mass contributions to the polar motion and length-of-day variations remains unclear due mainly to the lack of global accurate in-situ observations (Jin et al., 2012). Nowadays, satellite gravimetry provides new observations of global fluids mass changes and time-varying gravity field.

Greiner-Mai et al. (2003) explored core processes that influenced the Earth's rotation and the gravity field on decadal timescales. The Earth's core-mantle coupling was considered a factor in decadal length-of-day (LOD) variations, although debates surrounded its role in polar-motion variations. Electromagnetic-coupling torques relied on assumed electrical conductivity in the lower mantle, while topographic torques depended on the core-mantle boundary (CMB) topography. With no comprehensive theoretical framework for CMD parameters, coupling torques were evaluated for consistency with the observed Earth's rotation and geomagnetic field variations. The relative core angular momentum was linked to observed geomagnetic field and LOD variations, but the polar motion variations posed challenges. Mound and Buffett (2006) studied 42 years of LOD data and identified a  $5.8 \pm 0.8$ -

year oscillation caused by gravitational interactions between the mantle and inner core. To match the observed period, the mantle's density distribution and core-mantle boundary deformations played a crucial role, resulting in a gravitational coupling strength of  $\sim 3.0 \times 10^{20}$  N m. This finding implied that the inner core experienced a solid-body rotation over several years, setting a lower limit for its viscosity at around  $10^{17}$  Pa s. Jin et al. (2011) investigated Earth's LOD variations driven by mass movements in the atmosphere, oceans, and hydrosphere. They used data sources like the ECCO model, NCEP/NCAR reanalysis, ECMWF ERA-Interim, GRACE-derived mass data, and SLR-based  $C_{20}$  coefficient to study LOD changes at different time scales. Their findings showed that GRACE and combined GRACE+SLR solutions provided better explanations for geodetic residual LOD changes at annual and semi-annual scales, while SLR data was more effective at sub-annual scales. The combined GRACE+SLR solutions greatly improved our understanding of geodetic residual changes at intra-seasonal scales. Xu et al. (2014) introduced analytical formulas based on the spherical Earth dislocation theory for calculating co-seismic changes in Earth's rotation (including the polar motion and the length-of-day) and low-degree gravity field coefficients. They applied these formulas to assess co-seismic alterations caused by the four largest earthquakes since 1960, but their method lacked observational validation. Analysing the 2011 Tohoku-Oki earthquake (Mw 9.0), they discovered that the co-seismic Earth rotation changes varied with the earthquake magnitude and source parameters, highlighting differences between point source and finite fault models. They also investigated the impact of seawater redistribution on co-seismic Earth rotation changes, concluding that this influence was minimal and negligible.

A linear relationship between the second-degree gravitational changes (described by the spherical harmonic coefficients  $\Delta C_{21}$ ,  $\Delta S_{21}$ , and  $\Delta C_{20}$ ) and the polar motion mass excitations ( $\chi_1^{\text{mass}}$ ,  $\chi_2^{\text{mass}}$ ) as well as the length-of-day excitation ( $\chi_3^{\text{mass}}$ ) can be obtained from the Earth's rotational theory (Eubanks, 1993) and by using the Earth's gravity field spherical harmonic expansion in the following form (Chen et al., 2016a, 2016b):

$$\chi_1^{\text{mass}} = -\frac{1.098R^2M}{(1+k_2)(C-A)} \sqrt{\frac{5}{3}} \Delta \bar{C}_{21} \quad (24a)$$

$$\chi_2^{\text{mass}} = -\frac{1.098R^2M}{(1+k_2')(C-A)}\sqrt{\frac{5}{3}}\Delta\bar{S}_{21} \quad (24b)$$

$$\chi_3^{\text{mass}} = -\frac{0.753R^2M}{(1+k_2')C_m}\frac{2\sqrt{5}}{3}\Delta\bar{C}_{20}, \quad (24c)$$

where  $M$  and  $R$  are respectively the mass and mean radius of Earth,  $C$  and  $A$  are the two principal inertia moments of the Earth,  $C_m = 7.1236 \times 10^{37} \text{ kg m}^2$  is the principal moment of inertia of the mantle (Eubanks, 1993), and  $k_2'$  is the second-degree load Love number ( $-0.301$ ) (Wahr et al., 1998).

#### 4.2.5. Hydrological signal

The gravity field and hydrological modelling play interconnected roles in understanding of the Earth's water distribution and movement. The gravity field, as measured by satellites like GRACE, provides essential data on changes in terrestrial water storage. This data is used in hydrological modelling to improve our understanding of groundwater, soil moisture, snowpack, and other components of the water cycle. Hydrological models, such as the Global Land Data Assimilation System (GLDAS, Rodell et al., 2004), incorporate gravity data to enhance the accuracy of water-related simulations. Together, these tools help scientists monitor water resources, predict droughts and floods, and study the impacts of climate change on Earth's hydrology.

Günter (2008) highlighted how data from the GRACE satellite mission has advanced our understanding of global water storage changes. Werth et al. (2009) improved hydrological simulations by incorporating GRACE data into the WaterGAP Global Hydrology Model, showing significant accuracy enhancements in the Amazon, Mississippi, and Congo Basins. Kusche et al. (2009) introduced a decorrelation

technique for GRACE data, validating it against global hydrological models and showing improved reliability. Jin et al. (2012) investigated the hydrological effects on polar motion using GRACE data, despite challenges in data processing. Soltani et al. (2021) reviewed the integration of GRACE Terrestrial Water Storage (TWS) data into hydrological models, highlighting the critical role of this integration in understanding water storage changes amid global climate change. Fatolazadeh et al. (2022a) proposed a novel approach for downscaling GRACE's Terrestrial Water Storage Anomalies (TWSA) to daily resolutions, improving hydrological analyses. Following this, Fatolazadeh et al. (2022b) advanced the use of GRACE data for terrestrial and groundwater storage estimation with a spectral combination approach, contributing to more accurate hydrological models and better water resource management. Hydrological signals represent dynamic changes in Earth's gravity field, originating from factors such as groundwater storage (GWS), snow water equivalent (SWE), solid moisture (SM), and canopy (CAN). To capture these signals, various models have been developed, with the Global Land Data Assimilation System (GLDAS) model being among the most widely used (Rodell et al., 2004). The GLDAS model demonstrates a good agreement with the temporal variations of the gravity field observed by GRACE. However, the GRACE models provide information about the total water content, the equivalent water height, or combinations of SM, SWE, CAN, and GWS.

Hence, if specific hydrological signals are required, they can be determined through a combination of GRACE and hydrological models. For instance, the GWS is computed by using the following formula:

$$\delta h_{nm}^{\text{GWS}} = \sum_{n=2}^{\infty} \sum_{m=-n}^n \left[ \frac{1}{4\pi G R \gamma} \frac{2n+1}{1+k_n} \delta v_{nm} - \frac{1}{\rho_w} (\delta \rho_{nm}^{\text{SM}} + \delta \rho_{nm}^{\text{SWE}} + \delta \rho_{nm}^{\text{CAN}}) \right] Y_{nm}(\theta, \lambda) \quad (25)$$

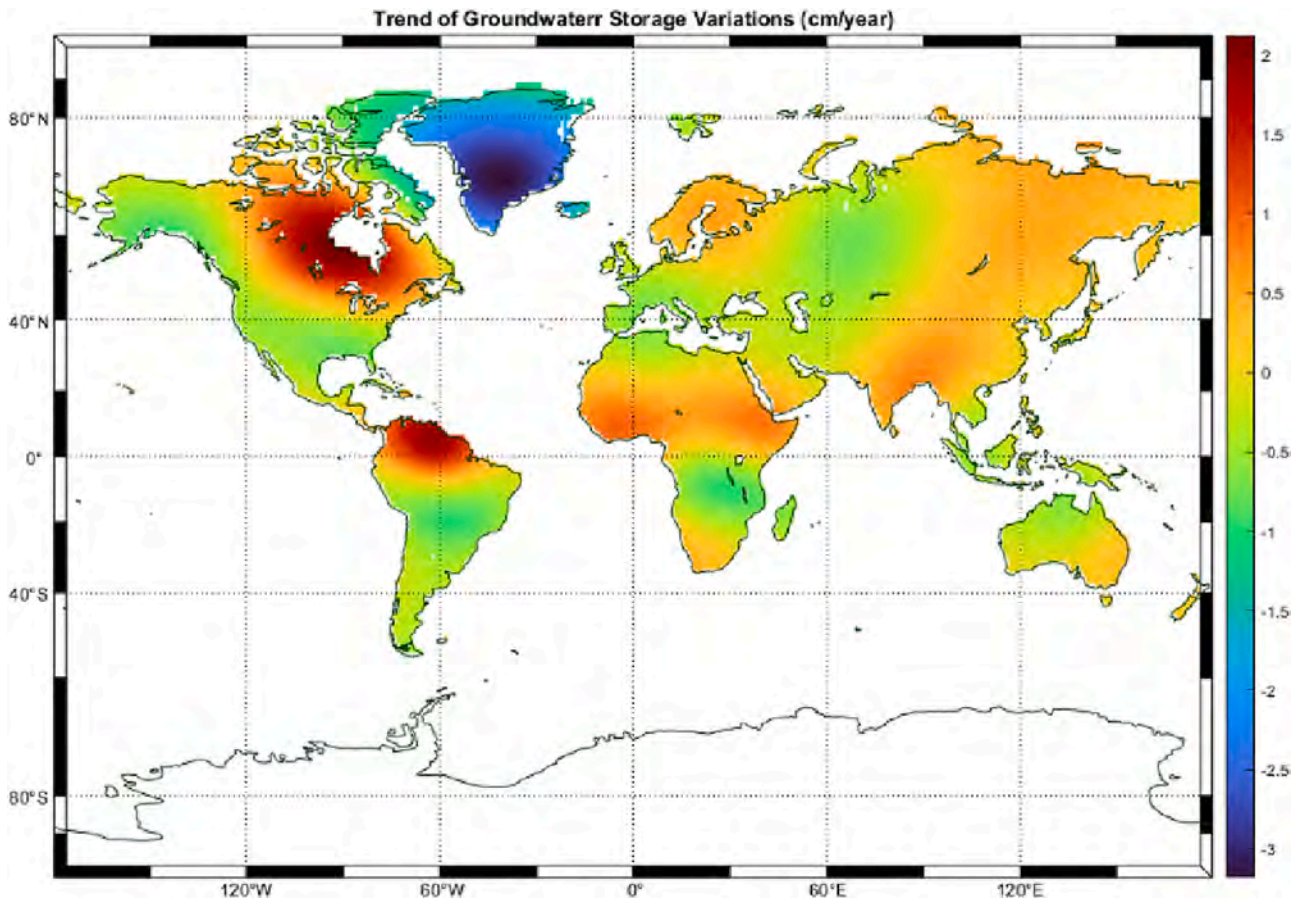


Fig. 12. Global groundwater storage (GWS) rate as determined from 15 years of GRACE and GLDAS.

where  $\rho_w$  is the density of water;  $\delta v_{nm}$  describe changes of the gravitational potential;  $k_n$  are the Love numbers; and  $\delta\rho_{nm}^{SM}$ ,  $\delta\rho_{nm}^{SWE}$ , and  $\delta\rho_{nm}^{CAN}$  define the spherical harmonic coefficients of the densities of SM, SWE, and CAN, respectively.

Fig. 12 displays the trend in global groundwater storage (GWS) derived from GRACE monthly solutions from 2002 to 2017, after the hydrological signal effects were removed using the GLDAS model. This trend was determined through simple regression analysis of each monthly GWS measurement during the specified period. The GLDAS data, which are presented in grid format, cover only terrestrial regions. To calculate the spherical harmonic coefficients of each hydrological parameter requiring global coverage, zero values were assigned to parameters over oceans. It is crucial to mention that these calculations do not account for post-glacial rebound and earthquake signals.

#### 4.2.6. Glacier changes

Polar and mountain glaciers significantly influence Earth's entire system variations (Jin et al., 2013). While satellite altimetry and other remote sensing techniques monitor glacier changes, they predominantly focus on estimating glacier height variations. GRACE monthly solutions enable the assessment of glacier mass changes. For instance, the surface mass change in Alaska was computed from GRACE gravitational RL05 solutions, revealing a substantial mass loss. Due to filtering and truncation effects inherent in GRACE data processing, the glacier mass loss signal spreads across an extensive area with an attenuating trend. Following corrections for leakage effects using the forward modelling approach, the results aligned closely with magnitudes measured by ICESat (Jin et al., 2017). Greenland ice-sheet loss is estimated at  $-171.56 \pm 19.24$  Gt/year, after accounting for leakage effects from September 2003 to March 2008, closely mirroring ICESat findings of  $-184.8 \pm 28.2$  Gt/year (Jin and Zou, 2015). Furthermore, the study unveiled the profound influence of leakage signals on seasonal and acceleration variations in glacier mass loss in Greenland, revealing an even more accelerated loss rate of glacier mass by  $-12.11$  Gt yr<sup>-2</sup> after correcting for leakage effects. Chen et al. (2007) employed recently reprocessed gravity solutions derived from GRACE models to assess ice loss rates within the Patagonia Icefield (PIF) in South America. Their

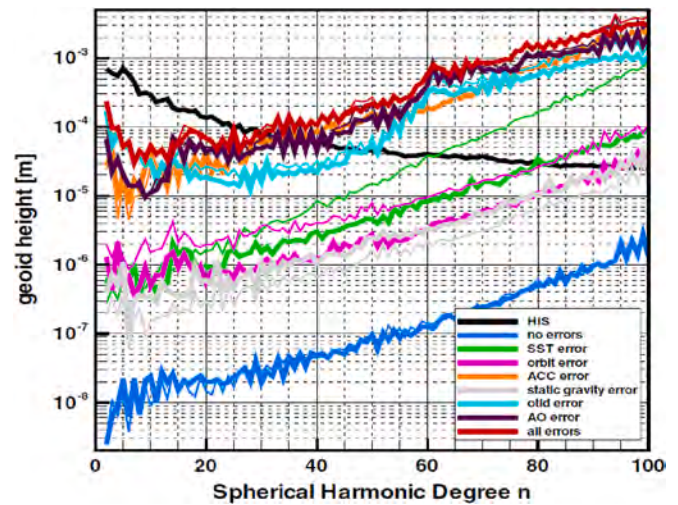


Fig. 14. Degree amplitudes in terms of the geoid height error for May 2021 for different individual instrument and model errors (see legend). The blue curve shows the numerical accuracy of the full-scale simulations (no errors applied) which is about three orders of magnitude below the current GRACE-FO error level. The black line depicts the monthly mean HIS signal (Flechtner et al., 2016). (For interpretation of the references to colour in this figure legend, the reader is referred to the web version of this article.)

study spanned from April 2002 to December 2006. After meticulous adjustments for postglacial rebound and hydrological influences, the researchers estimated an annual ice loss rate of approximately  $-27.9 \pm 11$  km<sup>-3</sup> for the Patagonia Icefield. This equates to an average yearly reduction in ice thickness of around  $-1.6$  m, assuming uniform distribution across the entire PIF area. The computed contribution of this ice loss to the global sea level rise amounted to  $0.078 \pm 0.031$  mm per year. This study not only independently confirmed earlier findings indicating substantial melting rates in the Patagonia Icefield but also underscored the profound impact of ice loss in this region on global sea levels. Root et al. (2015) conducted a comprehensive investigation in the Barents

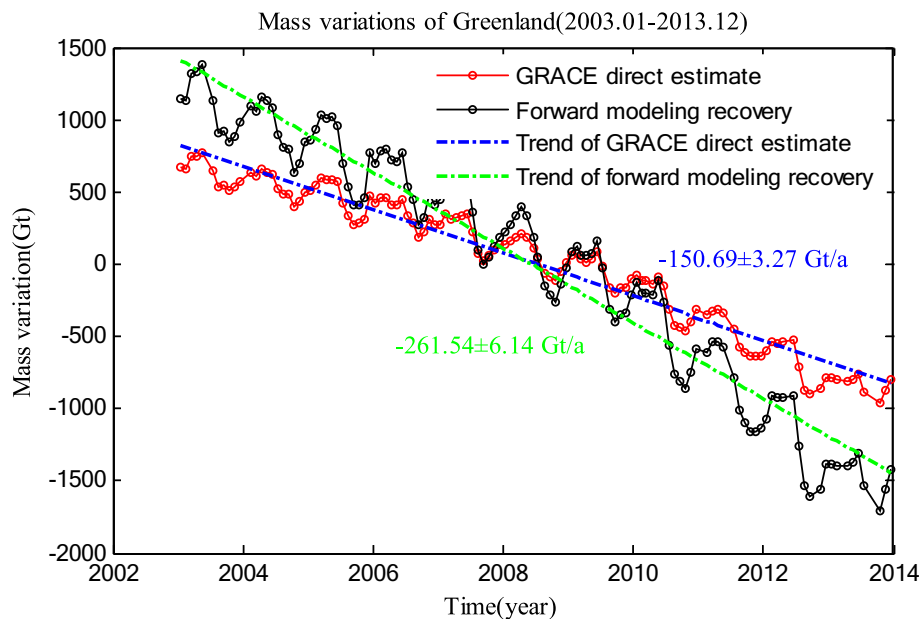
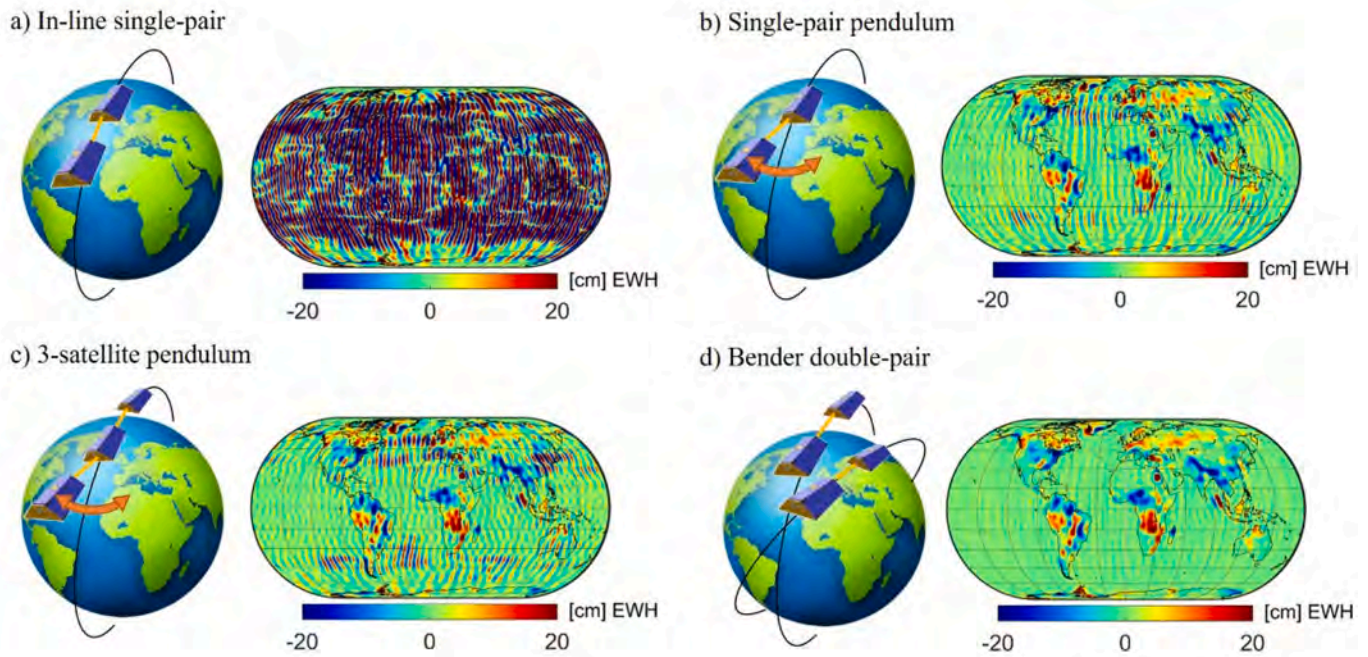


Fig. 13. GRACE-derived glacier mass variations in Greenland from January 2003 to December 2013. The red dot shows the direct estimates from GRACE measurements, the black dot represents the reconstructed mass estimates after correcting the leakage effects, the blue line shows the trend of direct GRACE estimates, and the green line presents the trend of reconstructed 'true' mass variation in Greenland. (For interpretation of the references to colour in this figure legend, the reader is referred to the web version of this article.)



**Fig. 15.** Various future gravity mission constellations and their gravity retrieval performance, shown in terms of temporal gravity variations superimposed by retrieval errors: a) in-line single polar pair; b) single-pair pendulum with opening angle  $30^\circ$ , c) 3-satellite pendulum, d) Bender double pair (from: [Torge et al., 2023](#)).

Sea, which has been subject to postglacial uplift following the retreat of the Weichselian ice sheet that once enveloped the area. Determining the historical thickness of the regional ice sheet has posed challenges due to limited data availability, primarily located at the periphery of the former ice sheet, near Franz Joseph Land, Svalbard, and Novaya Zemlya.

[Fig. 13](#) provides a comprehensive view of GRACE-derived glacier mass variations in Greenland, spanning from January 2003 to December 2013. Within the figure, key elements are highlighted: the red dot signifies direct estimates obtained from GRACE measurements, while the black dot represents the reconstructed mass estimates after meticulous correction for leakage effects. Additionally, the blue line tracks the trend of direct GRACE estimates, while the green line illustrates the trend of the reconstructed true mass variation in Greenland.

## 5. Challenges and prospective of satellite gravimetry

Although past and current satellite gravity missions have made a huge impact on many fields of geosciences, they still encounter several shortcomings and limitations. During the last couple of years, several conceptual studies for future gravity missions have been performed, with the goal to significantly improve spatial and temporal resolutions and accuracy as requested by the wide international user communities ([Pail et al., 2015](#)). Analysing the error contributors of current GRACE-type single in-line pair missions, it can be concluded that the main instrument errors, which are related to the inter-satellite ranging system, the accelerometer for directly measuring the non-conservative forces acting on the satellite, and GNSS-derived orbits are not the dominant error contributors. As it is shown in [Fig. 14](#) the total error is dominated by temporal aliasing, i.e. the fact that short-term mass change signals, which are mainly associated with high-frequency atmosphere and ocean variations and ocean tides, cannot be adequately captured by a single-pair mission due to its limited temporal resolution. Therefore, the performance of a future mission will not scale linearly with the improvement in instrumentation, but the main objective of a future gravity mission concept will be to reduce temporal aliasing.

In combination with the anisotropic error behaviour due to the inter-satellite ranging only in the flight direction, temporal aliasing leads to the typical striping patterns in temporal gravity solutions, see [Fig. 15a](#).

In general, satellite constellations that are different from the GRACE-type in-line tracking, but also extended constellations of several satellites or satellite pairs, are the preferred method to improve to increase the spatial-temporal resolution and to reduce aliasing. Theoretically, the isotropy of the error characteristics could be improved by modifying the orbit design of the two satellites from an in-line pair concept. Examples are the pendulum, see [Fig. 15b](#), Cartwheel or Helix type formations ([Elsaka et al., 2014](#)), where the two satellites perform a specific relative motion with respect to each other. However, the main technological limitation is that inter-satellite ranging has to be done multi-directionally due to the continuously changing relative position of two satellites, which move with rather high relative velocities.

In [Panet et al. \(2012\)](#) a single-pair mission in pendulum configuration was investigated and proposed as candidate mission in response to the ESA Earth Explorer 8 call. The pendulum formation, see [Fig. 15b](#), where the trailing satellite performs a relative cross-track motion with respect to the leading one, allows, therefore, also the observation of the cross-track component, thus improving the error characteristics of this mission concept and reducing significantly striping errors. A constellation being composed of an in-line single pair with an added third satellite flying in pendulum, see [Fig. 15c](#), was investigated by the French national space agency CNES. [Bender et al. \(2008\)](#), [Wiese et al. \(2012\)](#), and [Daras and Pail \(2017\)](#) analysed the possibility of flying, in addition to an in-line pair in polar orbit, a second satellite pair in an inclined orbit with an inclination of  $I = 65^\circ$  to  $70^\circ$  (Bender configuration); see [Fig. 15d](#). In this constellation the isotropy of the error behaviour is significantly improved due to the two different orbit planes. In [Hauk et al. \(2017\)](#) a mission concept based on high-precision inter-satellite tracking among satellites in Medium Earth Orbits (MEOs) and Low Earth Orbiters (LEOs) was investigated, leading to the mission proposal MOBILE in response to ESA's Earth Explorer 10 call ([Pail et al., 2019](#); [Hauk and Pail, 2019](#)).

Various mission concepts, with specific focus on the double-pair constellation, are currently investigated. As an example, the Mass-change And Geoscience International Constellation (MAGIC) is a joint effort within NASA's Mass Change (MC) project and ESA's Next-Generation Gravity Mission (NGGM) project as part of the Future EO Programme ([Massotti et al., 2021](#)). It is composed of a polar pair (MC) with a target launch date in 2028 in order to facilitate a continuation of

GRACE-FO, which will be complemented by an inclined pair (NGGM) with target launch date 2031. Beyond the significant reduction of temporal aliasing errors and improved accuracy, spatial and temporal resolution (Heller-Kaikov et al., 2023), the main focus of this double-pair mission concept is to enable fast-track gravity products with short latency serving operational service applications, such as drought and flood monitoring and forecasting, or water management.

Recent studies also investigate the feasibility of using very small satellites down to CubeSats in extended multi-satellite constellations for gravity field monitoring (Pfaffenzeller and Pail, 2023). They form a compromise of miniaturised payload with reduced measurement accuracy and the improved temporal resolution achievable with multiple satellites. Ideally, the investigation and realisation of future mission constellations shall initiate the establishment of a sustained gravity field and mass transport observing system from space.

## 6. Summary

This article elucidates the process of determining Earth Gravitational Models (EGMs) through spherical harmonic coefficients derived from satellite gravimetry observations. The precision and resolution of these models are pivotal for a wide range of geoscientific applications and are influenced by factors such as the satellite's orbital characteristics, the sensitivity of onboard instruments, and the methodologies used in data processing and analysis. Specifically, the GOCE mission, known for its capacity to map the Earth's gravitational field up to the degree and order of 300, encountered challenges in accurately determining low-degree harmonics. These challenges were primarily due to the limitations in the gradiometer's sensitivity and the complexities involved in distinguishing the gravitational signal from noise. This situation highlights the critical need for advanced data processing techniques and the integration of data from multiple sources to enhance the quality of EGMs. Similarly, the GRACE mission's innovative use of line-of-sight measurements in its low-low satellite-to-satellite tracking model showcases the potential to detect higher frequencies of the gravitational field more accurately than traditional inter-satellite range rates. This capability is particularly relevant for a variety of applications, including but not limited to geodetic applications such as geoid and physical height determination, orbit integration, and oceanographic applications like the determination of geostrophic velocities and eddy currents.

Moreover, the long-wavelength portion of the Earth's gravitational field, captured by these measurements, plays a crucial role in modelling and studying various geophysical phenomena. Importantly, the first-degree spherical harmonic coefficients, critical when the chosen coordinate system is not geocentric, facilitate the study of changes in the Earth's centre of mass or dipole moment. Additionally, the first- and second-degree spherical harmonic coefficients are instrumental in determining the Earth's inertia tensor and coordinate system, as well as the precession-nutation angles. Further, by analysing the temporal variations in these spherical harmonics coefficients, insights into changes in pole excitations and the length-of-the-day can be garnered. Spherical harmonic coefficients between degrees 13–25 prove to be suitable for modelling lithospheric stress and its temporal changes, highlighting the diverse applications of these coefficients. For assessments of the Earth's inner density structure and interfaces—such as Moho depth, sediment basement morphology, or glacier thickness—higher-degree harmonics, up to degree 180, are utilised. These measurements are also pivotal in estimating additional geophysical parameters, such as the effective elastic thickness, which describes the lithosphere's strength and its relationship with tectonic, geological, and volcanic processes.

Despite the advancements made by recent satellite missions, challenges remain, particularly in improving the spatial and temporal resolution of time-variable EGMs. Future satellite missions are expected to focus on overcoming these limitations, employing advanced technologies and methodologies to capture the Earth's gravity field with unprecedented accuracy. This progress is anticipated to enhance our

understanding of geodynamic processes significantly, enabling more precise modelling and offering new insights into the Earth's changing environment.

By addressing the technical specifics, the factors affecting resolution and accuracy, and providing a clearer picture of the applications and implications of spherical harmonic coefficients, we gain a more comprehensive understanding of the importance of satellite gravimetry in geosciences and the ongoing efforts to refine these crucial measurements in the future.

## Declaration of competing interest

The authors declare that they have no conflict of interest. The results presented in this manuscript have not been influenced by any financial or personal relationships with individuals or organisations. All sources of funding for this study are disclosed, and there are no relationships or activities that could be perceived as biasing the research reported in this manuscript.

## Data availability

Data will be made available on request.

## Acknowledgments

Shuanggen Jin was supported by the National Key Research and Development Program of China Project (Grant No. 2018YFC0603502). Pavel Novák was supported by the project GA21-13713S of the Czech Science Foundation. Mehdi Eshagh is thankful to University of West Bohemia for supporting his study visit.

## References

- Abbaszadeh, M., Sharifi, M.A., Nikkhoo, M., 2013. A comparison of the estimated effective elastic thickness of the lithosphere using terrestrial and satellite-derived data in Iran. *Acta Geophys.* 61, 638–648.
- Abrehdary, M., Sjöberg, L.E., 2023. Recovering Moho constituents from satellite altimetry and gravimetric data for Europe and surroundings. *J. App. Geod.* 13 (4), 291–303. <https://doi.org/10.1515/jag-2019-0011>.
- Airy, G.B., 1855. On the computations of the effect of the attraction of the mountain masses as disturbing the apparent astronomical latitude of stations in geodetic surveys. *Trans. R. Soc. Lond. Ser. B Biol. Sci.* 145, 101–104.
- Anselmi, A., Cambiotti, G., Cesare, S., Douch, K., Haagmans, R., Marotta, A.M., Sabadini, R., 2020. On earthquake detectability by the next-generation gravity mission. *Surv. Geophys.* 41, 1049–1074. <https://doi.org/10.1007/s10712-020-09632-y>.
- Audet, P., Mareschal, J.C., 2004. Variations in elastic thickness in the Canadian Shield. *Earth Planet. Sci. Lett.* 226 (1–2), 17–31.
- Balmino, G., Reigber, C., Moynot, B., 1976. A geopotential model determined from recent satellite observing campaigns (GRIM1). *Manuscr Geodaet* 1 (1), 41–69.
- Barzaghi, R., 2016. The remove-restore method. In: Grafarend, E.W. (Ed.), *Encyclopedia of Geodesy*. Springer.
- Barzaghi, R., Reguzzoni, M., Borghi, A., De Gaetani, C., Sampietro, D., Marotta, A.M., 2016. Global to local Moho estimate based on GOCE geopotential model and local gravity data. In: VIII Hotine-Marussi Symposium on Mathematical Geodesy: Proceedings of the Symposium in Rome, 17–21 June, 2013. Springer International Publishing, pp. 275–282.
- Bender, P.L., Wiese, D., Nerem, R.S., 2008. A possible Dual-GRACE mission with 90 degree and 63 degree inclination orbits. In: Proc. 3<sup>rd</sup> Int. Symp. Formation Flying, Missions and Technologies, ESA/ESTEC, Noordwijk, 23–25 April 2008, pp. 1–6.
- Bjerhammar, A., 1968. On the Energy Integral for Satellites. The Royal Institute of Technology (KTH). Division of Geodesy, Stockholm, Sweden.
- Bjerhammar, A., Stocki, S., Svensson, L., 1980. A Geodetic Determination of Viscosity. The Royal Institute of Technology, Stockholm.
- Bouillé, F., Cazenave, A., Lemoine, J.M., Crétaux, J.F., 2000. Geocentre motion from the DORIS space system and laser data to the Lageos satellites: comparison with surface loading data. *Geophys. J. Int.* 143 (1), 71–82. <https://doi.org/10.1046/j.1365-246x.2000.00196.x>.
- Bourda, G., Capitaine, N., 2004. Precession, nutation, and space geodetic determination of the Earth's variable gravity field. *Astron. Astrophys.* 428 (2), 691–702.
- Braitenberg, C., Ebbing, J., 2009. New insights into the basement structure of the West Siberian Basin from forward and inverse modelling of GRACE satellite gravity data. *J. Geophys. Res. Solid Earth* 114 (B6). <https://doi.org/10.1029/2008JB005799>.
- Braitenberg, C.A.R.L.A., Zadro, M.A.R.I.A., Fang, J., Wang, Y., Hsu, H.T., 2000. The gravity and isostatic Moho undulations in Qinghai-Tibet plateau. *J. Geodyn.* 30 (5), 489–505.

- Braitenberg, C., Ebbing, J., Götze, H.J., 2002. Inverse modelling of elastic thickness by convolution method—the eastern Alps as a case example. *Earth Planet. Sci. Lett.* 202, 387–404.
- Braitenberg, C., Wienecke, S., Wang, Y., 2006. Basement structures from satellite-derived gravity field: South China Sea ridge. *J. Geophys. Res. Solid Earth* 111 (B5). <https://doi.org/10.1029/2005JB003938>.
- Bull, C., Hardy, J.R., 2017. *The Determination of the Thickness of a Glacier from Measurements of the Value of Gravity*. Cambridge University Press.
- Burov, E.B., Diament, M., 1995. The effective elastic thickness ( $T_e$ ) of continental lithosphere: what does it really mean? *J. Geophys. Res.* 100 (B3), 3905–3927.
- Calmant, S., Baudry, N., 1996. A gravity-derived free-air anomaly grid for the global ocean and marginal seas. *J. Geophys. Res. Solid Earth* 101 (B2), 3227–3246.
- Calmant, S., Francheteau, J., Cazenave, A., 1990. Elastic layer thickening with age of the oceanic lithosphere: a tool for prediction of the age of volcanoes or oceanic crust. *Geophys. J. Int.* 100 (1), 59–67.
- Capitaine, N., Chapront, J., Lambert, S., Wallace, P.T., 2003. Expressions for the Celestial Intermediate Pole and Celestial Ephemeris Origin consistent with the IAU 2000A precession-nutation model. *Astron. Astrophys.* 400 (3), 1145–1154.
- Carton, X., 2001. Hydrodynamical modeling of oceanic vortices. *Surv. Geophys.* 22, 179–263.
- Chaigneau, A., Gizolme, A., Grados, C., 2008. Mesoscale eddies off Peru in altimeter records: Identification algorithms and eddy spatio-temporal patterns. *Prog. Oceanogr.* 79 (2–4), 106–119. <https://doi.org/10.1016/j.pocean.2008.10.013>.
- Chao, B.F., Liao, J.R., 2019. Gravity changes due to large earthquakes detected in GRACE satellite data via empirical orthogonal function analysis. *J. Geophys. Res. Solid Earth* 124 (2), 2304–2319. <https://doi.org/10.1029/2018JB016862>.
- Chelton, D.B., Schlax, M.G., Samelson, R.M., 2011. Global observations of nonlinear mesoscale eddies. *Prog. Oceanogr.* 91 (2), 167–216.
- Chen, W., Shen, W., 2010. New estimates of the inertia tensor and rotation of the triaxial nonrigid Earth. *J. Geod.* 76, 495–509. <https://doi.org/10.1029/2009JB007094>.
- Chen, B., Kaban, M.K., El Kherpy, S., Al-Arif, N., 2015. Effective elastic thickness of the Arabian plate: weak shield versus strong platform. *Geophys. Res. Lett.* 42, 3298–3304.
- Chen, J., Kok, A., Rummel, G.J., Gross, J.J., Bruckmaier, R.M., Kemp, B., van Kneusel, A.T.M., 2016a. Effects of dry period length and dietary energy source on lactation curve characteristics over 2 subsequent lactations. *J. Dairy Sci.* 99 (11), 9287–9299. <https://doi.org/10.3168/jds.2016-11253>.
- Chen, J.L., Wilson, C.R., Ries, J.C., 2016b. Broad-band assessment of degree-2 gravitational changes from GRACE and other estimates, 2002–2015. *J. Geophys. Res. Solid Earth* 121, 2112–2128. <https://doi.org/10.1029/2015JB012708>.
- Chen, J.L., Wilson, C.R., Tapley, B.D., Blankenship, D.D., Ivins, E.R., 2007. Patagonia icefield melting observed by gravity recovery and climate experiment (GRACE). *Geophysical Research Letters* 34, L22501.
- Cheng, M.K., Ries, J.C., Tapley, B.D., 2013. Geocenter variations from analysis of SLR data. In: Altamimi, Z., Collilieux, X. (Eds.), *Reference Frames for Applications in Geodesy*. International Association of Geodesy Symposia, vol. 138. Springer, Berlin, Heidelberg. [https://doi.org/10.1007/978-3-642-32998-2\\_4](https://doi.org/10.1007/978-3-642-32998-2_4).
- Conrad, C.P., Lithgow-Bertelloni, C., 2006. Influence of continental roots and asthenosphere on plate-mantle coupling. *Geophys. Res. Lett.* 33 (5).
- Cui, W., Wang, W., Zhang, J., Yang, J., 2019. Multicore structures and the splitting and merging of eddies in global oceans from satellite altimeter data. *Ocean Sci.* 15, 413–430. <https://doi.org/10.5194/os-15-413-2019>.
- Daras, I., Pail, R., 2017. Treatment of temporal aliasing effects in the context of next-generation satellite gravimetry missions. *J. Geophys. Res.* 22 (9), 7343–7362.
- Dermanis, A., Liviratos, E., 1983. Applications of deformation analysis in geodesy and geodynamics. *Rev. Geophys. Space Phys.* 21, 41–50.
- Ditmar, P., van der Sluijs Eck, 2004. A technique for modelling the Earth's gravity field on the basis of satellite accelerations. *J. Geodyn.* 78, 12–33.
- Dong, D., Dickey, J.O., Chao, Y., Cheng, M.K., 1997. Geocenter variations caused by atmosphere, ocean and surface ground water. *Geophys. Res. Lett.* 24 (15), 1867–1870.
- Dong, C., Xu, G., Han, G., Chen, N., He, Y., Chen, D., 2018. Identification of tidal mixing fronts from high-resolution along-track altimetry data. *Remote Sens. Environ.* 209, 489–496.
- Douglas, B.C., Palmeter, M.T., 1967. Resonant satellite geodesy study Final report (No. TRW-09128-6001-R000).
- Drinkwater, M.R., Floberghagen, R., Haagmans, R., et al., 2003. GOCE: ESA's first earth explorer core mission. In: Beutler, G., Drinkwater, M.R., Rummel, R., von Steiger, R. (Eds.), *Earth Gravity Field from Space – From Sensors to Earth Sciences*, Space Sciences Series of ISSI, vol. 17. Kluwer Academic Publishers, Dordrecht, The Netherlands, pp. 419–432.
- Ekman, M., Mäkinen, J., 1996. Recent postglacial rebound, gravity change, and mantle flow in Fennoscandia. *Geophys. J. Int.* 126 (1), 229–234. <https://doi.org/10.1111/j.1365-246X.1996.tb05281.x>.
- Elmas, A., 2022. Estimating sediment thickness in the Tuz Gölü Basin using various methods. *Arab. J. Geosci.* 15 (2), 189.
- Elsaka, B., Raimondo, J.-C., Brieden, P., et al., 2014. Comparing seven candidate mission configurations for temporal gravity retrieval through full-scale numerical simulation. *J. Geodyn.* 88, 31–43.
- Engen, O., Digranes, P., Elvebakk, H., 2006a. Predicting sediment thickness by inversion of altimetry-derived gravity data in the Norwegian–Greenland Sea. *Geophysics* 71 (6), L49–L56.
- Engen, Ø., Frazer, L.N., Wessel, P., Faleide, J.I., 2006b. Prediction of sediment thickness in the Norwegian–Greenland Sea from gravity inversion. *J. Geophys. Res. Solid Earth* 111 (B11). <https://doi.org/10.1029/2005JB003924>.
- Eshagh, M., 2014. From satellite gradiometry data to subcrustal stress due to mantle convection. *Pure Appl. Geophys.* 171 (9), 2391–2406.
- Eshagh, M., 2016. On Vening Meinesz–Moritz and flexural theories of isostasy and their comparison over Tibet Plateau. *J. Geod. Sci.* 6, 1. <https://doi.org/10.1515/jogs-2016-0013>.
- Eshagh, M., 2017. On the approximations in formulation of the Vening Meinesz–Moritz theory of isostasy. *Geophys. J. Int.* 210 (1), 500–508. <https://doi.org/10.1093/gji/ggx179>.
- Eshagh, M., 2018. Elastic thickness determination based on Vening Meinesz–Moritz and flexural theories of isostasy. *Geophys. J. Int.* 213 (3), 1682–1692. <https://doi.org/10.1093/gji/ggy075>.
- Eshagh, M., 2020. *Satellite Gravimetry and the Solid Earth*, Mathematical Foundations. Elsevier.
- Eshagh, M., 2021. The Earth's Gravity Field Role in Geodesy and Large-Scale Geophysics. In: Erol, B., Erol, S. (Eds.), *Geodetic Sciences - Theory, Applications and Recent Developments*. IntechOpen. <https://doi.org/10.5772/intechopen.97459>.
- Eshagh, M., Hussain, M., 2016. An approach to Moho discontinuity recovery from on-orbit GOCE data with application over Indo-Pak region. *Tectonophysics* 690, 253–262.
- Eshagh, M., Najafi-Alamdari, M., 2007. Perturbations in orbital elements of a low Earth orbiting (LEO) satellite. *J. Earth Space Phys.* 33 (1), 1–12.
- Eshagh, M., Pitoňák, M., 2019. Elastic thickness determination from on-orbit GOCE data and CRUST1.0. *Pure Appl. Geophys.* 176 (2), 685–696.
- Eshagh, M., Tenzer, R., 2021. The temporal viscoelastic model of flexural isostasy for estimating the elastic thickness of the lithosphere. *Geophys. J. Int.* 227 (3), 1700–1714. <https://doi.org/10.1093/gji/ggab292>.
- Eshagh, M., Hussain, M., Tenzer, R., Roshkani, M., 2016. Moho density contrast in Central Eurasia from GOCE gravity gradients. *Remote Sens.* 8 (5), 418.
- Eshagh, M., Steinberger, B., Tenzer, R., Tassara, A., 2018. Comparison of gravimetric and mantle flow solutions for sub-lithospheric stress modelling and their combination. *Geophys. J. Int.* 213 (2), 1013–1028.
- Eshagh, M., Pitoňák, M., Tenzer, R., 2019. Lithospheric elastic thickness estimates in Central Eurasia. *Terr. Atmos. Ocean. Sci.* 30 (1), 73–84.
- Eshagh, M., Fatolazadeh, F., Tenzer, R., 2020a. Lithospheric stress, strain and displacement changes from GRACE-FO time-variable gravity: case study for Sar-e-Pol Zahab Earthquake 2018. *Geophys. J. Int.* 223, 379–397.
- Eshagh, M., Tenzer, R., Eshagh, M., 2020b. Elastic thickness of the Iranian lithosphere from gravity and seismic data. *Tectonophysics* 774, 228186. <https://doi.org/10.1016/j.tecto.2019.228186>.
- Eubanks, T.M., 1993. Variations in the orientation of the Earth. In: Smith, D., Turcotte, D. (Eds.), *Contributions of Space Geodesy to Geodynamic: Earth Dynamics, Geodyn. Ser.* vol. 24. AGU, Washington, D. C., pp. 1–54.
- Fatolazadeh, F., Kalifa, G., Javadi, Azar R., 2019. Determination of earthquake epicenter based on invariant quantities of GRACE strain gravity tensor. *Sci. Rep.* 10, 7636.
- Fatolazadeh, F., Eshagh, M., Goita, K., 2022a. New spectro-spatial downscaling approach for terrestrial and groundwater storage variations estimated by GRACE models. *J. Hydrol.* 615, 128635.
- Fatolazadeh, F., Eshagh, M., Goita, K., Wang, S., 2022b. A New Spatiotemporal Estimator to Downscale GRACE Gravity Models for Terrestrial and Groundwater Storage Variations Estimation. *Remote Sens.* 14 (23), 5991.
- Filmer, P.E., McNutt, M.K., Wolfe, C.J., 1993. Elastic thickness of the lithosphere in the Marquesas and Society Islands. *J. Geophys. Res.* 98 (B11), 19565–19577.
- Fischell, R.E., Pisacane, V.L., 1978. A drag-free lo-lo satellite system for improved gravity field measurements. In: *Proceedings of the 9<sup>th</sup> GEOP Conference, An International Symposium on the Applications of Geodesy to Geodynamics*, October 2–5, 1978. Department of Geodetic Science, Report No. 280. The Ohio State University, Columbus, the USA.
- Flechtner, F., et al., 2016. What can be expected from the GRACE-FO laser ranging interferometer for earth science applications? In: Cazenave, A., Champollion, N., Benveniste, J., Chen, J. (Eds.), *Remote Sensing and Water Resources*, Space Sciences Series of ISSI, vol. 55. Springer, Cham. [https://doi.org/10.1007/978-3-319-32449-4\\_11](https://doi.org/10.1007/978-3-319-32449-4_11).
- Flechtner, F., Reigber, C., Rummel, R., et al., 2021. Satellite gravimetry: a review of its realization. *Surv. Geophys.* 42, 1029–1074. <https://doi.org/10.1007/s10712-021-09658-0>.
- Forsberg, R., Skourup, H., 2005. Retrieval of sea ice and freeboard over the Arctic Ocean from ICESat laser altimetry. *Geophys. Res. Lett.* 32 (4), L04503. <https://doi.org/10.1029/2004GL021947>.
- Förste, C., Flechtner, F., Schmidt, R., Stubenvoll, R., Rothacher, M., Kusche, J., Meyer, U., 2008. EIGEN-GL05C-A new global combined high-resolution GRACE-based gravity field model of the GFZ-GRGS cooperation. In: *General Assembly European Geosciences Union (Vienna, Austria 2008)*.
- Förste, C., Bruinsma, S., Abrikosov, O., Lemoine, J., Schaller, T., Götze, H., Biancale, R., 2014. EIGEN-6C4. The latest combined global gravity field model including GOCE data up to degree and order, 2190. <http://icgem.gfz-potsdam.de/Foerste-et-al-EIGE-N-6C4.pdf>.
- Forsyth, D.W., 1985. Subsurface loading and estimates of the flexural rigidity of continental lithosphere. *J. Geophys. Res. Solid Earth* 90 (B14), 12623–12632.
- Freedman, W., Gervens, T., Schreiner, M., 1998. *Constructive Approximation on the Sphere with Applications to Geomathematics*. Oxford University Press, New York.
- Fu, R.S., Huang, P.H., 1983. The global stress field in the lithosphere obtained from the satellite gravitational harmonics. *Phys. Earth Planet. Inter.* 31 (3), 269–276.
- Fu, R.S., Huang, J.H., 1990. Global stress pattern constrained on deep mantle flow and tectonic features. *Phys. Earth Planet. Inter.* 60 (1–4), 314–323.
- Galán, R.A., Casallas, I.F., 2010. Determination of effective elastic thickness of the Colombian Andes using satellite-derived gravity data. *Earth Sci. Res. J.* 14 (1), 7–16.

- Gedamu, A.A., Eshagh, M., Bedada, T.B., 2020. Moho determination from GOCE gradiometry data over Ethiopia. *J. Afr. Earth Sci.* 163, 103741.
- Gómez-Ortiz, D., Tejero, R., Ruiz, J., Babin-Vich, R., González-Casado, J.M., 2005. Estimating the effective elastic thickness of lithosphere of the Iberian Peninsula based on multi-taper spectral analysis. *Geophys. J. Int.* 160, 729–735.
- Greiner-Mai, H., Jochmann, H., Barthelmes, F., Ballani, L., 2003. Possible influences of core processes on the Earth's rotation and the gravity field. *J. Geodyn.* [https://doi.org/10.1016/S0264-3707\(03\)00054-1](https://doi.org/10.1016/S0264-3707(03)00054-1).
- Gruber, T., Bode, A., Reigber, C., Schwintzer, P., Balmino, G., Biancale, R., Lemoine, J. M., 2000. GRIM5-C1: Combination solution of the global gravity field to degree and order 120. *Geophys. Res. Lett.* 27 (24), 4005–4008.
- Güntner, A., 2008. Improvement of global hydrological models using GRACE data. *Surv. Geophys.* 29, 375–397.
- Guo, J., Han, Y., Hwang, C., 2008. Analysis on motion of Earth's center of mass observed with CHAMP mission. *Sci. China, Ser. G* 51 (10), 1597–1606.
- Guo, X., Ditmar, P., Zhao, Q., Klees, R., Farahani, H., 2017. Earth's gravity field modelling based on satellite accelerations derived from onboard GPS phase measurements. *J. Geod.* 91 (9), 1049–1068.
- Haagmans, R., de Min, E., Gelderen, M., 1993. Fast evaluation of convolution integrals on the sphere using 1D FFT, and a comparison with existing methods for Stokes' integral, *manuscripta geodaetica*, 18, pp. 227–241.
- Hager, B.H., O'Connell, R.J., 1981. A simple global model of plate dynamics and mantle convection. *J. Geophys. Res.* 86 (B6), 4843–4867.
- Hauk, M., Pail, R., 2019. Gravity field recovery using high-precision, high-low inter-satellite links. *Remote Sens.* 11 (5), 537.
- Hauk, M., Schlicht, A., Pail, R., Murböck, M., 2017. Gravity field recovery in the framework of a Geodesy and Time Reference in Space (GETRIS). *Adv. Space Res.* 59 (8), 2032–2047.
- Heiskanen, W.A., 1931. New isostatic tables for the reduction of the gravity values calculated on the basis of Airy's hypothesis, 2. Publications of the Isostatic Institute of the International Association of Geodesy (IAG), p. 1931.
- Heiskanen, W., Moritz, H., 1967. *Physical Geodesy*. W.H. Freeman and Co., San Francisco-London.
- Heller, B., Siegmund, F., Pail, R., Gruber, T., Haagmans, R., 2020. Temporal gravity signals in reprocessed GOCE gravitational gradients. *Remote Sens.* 12 (21), 3483. <https://doi.org/10.3390/rs12213483>.
- Heller-Kaikov, B., Pail, R., Daras, I., 2023. Mission design and processing aspects for the Mass Change and Geoscience International Constellation (MAGIC). *Geophys. J. Int.* 235 (1), 718–735.
- Hofmann-Wellenhof, B., Lichtenegger, H., Wasle, E., 2011. *GNSS – Global Navigation Satellite Systems*. Springer.
- Hussain, M., Eshagh, M., Ahmad, Z., Sadiq, M., Fatolazadeh, F., 2016. Changes in gravitational parameters inferred from time-variable GRACE data – A case study for October 2005 Kashmir earthquake. *J. Appl. Geophys.* <https://doi.org/10.1016/j.jappgeo.2016.07.008>.
- Hwang, C., 2010a. A bathymetric model for the South China Sea from satellite altimetry and depth data. [Published online on October 29, 2010]. Retrieved from. <https://doi.org/10.1080/014904199273597>.
- Hwang, C., 2010b. Bathymetric mapping of the South China Sea using satellite altimetry, shipborne depth soundings, and a remotely sensed gravity field. *Mar. Geophys. Res.* 31 (1), 1–11.
- Hwang, C., Kao, R., Wu, C.-R., 2002. The kinematics of Mesoscale Eddies from TOPEX/Poseidon altimetry over the subtropical counter currents. In: Hwang, C., Shum, C., Li, J. (Eds.), *Satellite altimetry for Geodesy, Geophysics and Oceanography*, vol. 1. International Association of Geodesy Symposia, pp. 183–190.
- Ihde, J., Sánchez, L., Barzaghi, R., Drewes, H., Förste, C., Gruber, T., Liesch, G., Marti, U., Pail, R., Sideris, M., 2017. Definition and proposed realization of the International Height Reference System (IHRs). *Surv. Geophys.* 38 (3) <https://doi.org/10.1007/s10712-017-9409-3>.
- International Height Reference System (IHRs), July 2015. IAG Resolution No. 1, Prague, p. 1. <https://office.iag-ig.org/doc/5d7b8fd9d31dc.pdf>.
- Jekeli, C., 1999. The determination of gravitational potential differences from satellite-to-satellite tracking. *Celest. Mech. Dyn. Astron.* 75 (2), 85–101.
- Jekeli, C., Rapp, R., 1980. Accuracy of the Determination of Mean Anomalies and Mean Geoid Undulations from a Satellite Gravity Field Mapping Mission. Report No. 307., Department of Geodetic Science, Ohio State University, Columbus, USA.
- Jin, S.G., Zou, F., 2015. Re-estimation of glacier mass loss in Greenland from GRACE with correction of land-ocean leakage effects. *Glob. Planet. Chang.* 135, 170–178. <https://doi.org/10.1016/j.gloplacha.2015.11.002>.
- Jin, S.G., Zhang, L.J., Tapley, B.D., 2011. The understanding of length-of-day variations from satellite gravity and laser ranging measurements. *Geophys. J. Int.* 184 (2), 651–660. <https://doi.org/10.1111/j.1365-246X.2010.04869.x>.
- Jin, S.G., Hassan, A.A., Feng, G.P., 2012. Assessment of terrestrial water contributions to polar motion from GRACE and hydrological models. *J. Geodyn.* 62, 40–48. <https://doi.org/10.1016/j.jog.2012.01.009>.
- Jin, S.G., van Dam, T., Wdowinski, S., 2013. Observing and understanding the Earth system variations from space geodesy. *J. Geodyn.* 72, 1–10. <https://doi.org/10.1016/j.jog.2013.08.001>.
- Jin, S.G., Zhang, T., Zou, F., 2017. Glacial density and GIA in Alaska estimated from ICESat, GPS, and GRACE measurements. *J. Geophys. Res. Earth Surf.* 122 (1), 76–90. <https://doi.org/10.1002/2016JF003926>.
- Johnson, C.L., Solomon, S.C., Head III, J.W., Phillips, R.J., Smith, D.E., Zuber, M.T., 2000. Lithospheric loading by the northern polar cap on Mars. *Icarus* 144 (2), 313–328.
- Jordan, T.A., Watts, A.B., 2005. Gravity anomalies, flexure, and the elastic thickness structure of the India-Eurasia collisional system. *Earth Planet. Sci. Lett.* 236, 732–750.
- Jung, W., Brozena, J., Peters, M., 2013a. Predicting gravity and sediment thickness in Afghanistan. *Geophys. J. Int.* 192 (2), 586–601. <https://doi.org/10.1093/gji/ggs038>.
- Jung, W.Y., Park, K.H., Kim, B.K., Kim, D.C., Kim, J.W., Park, S.K., Kim, S. S., 2013b. Predicting gravity and sediment thickness over Afghanistan. *Geophys. J. Int.* 195 (3), 1497–1511.
- Kaban, M.K., Delvaux, D., Maddaloni, F., Tesauro, M., Braitenberg, C., Petrunin, A.G., El Khrepy, S., 2021a. Thickness of sediments in the Congo basin based on the analysis of decompensative gravity anomalies. *J. Afr. Earth Sci.* 184, 104201 <https://doi.org/10.1016/j.jafrearsci.2021.104201>.
- Kaban, M.K., Abot, A., Vassallo, R., 2021b. Sedimentary thickness estimation of the Congo basin from decompensative gravity anomalies. *Geophys. J. Int.* 225 (2), 1245–1258.
- Kaula, W.M., 1963. Elastic models of the mantle corresponding to variations in the external gravity field. *J. Geophys. Res.* 68 (17), 4967–4978.
- Kaula, W., 1966. *Theory of Satellite Geodesy*. Blaisdell Publishing Company, Waltham, Massachusetts, USA.
- Kinoshita, H., 1977. Theory of the rotation of the rigid Earth. *Celest. Mech.* 16, 277–326.
- Kirby, J.F., 2014. Estimation of the effective elastic thickness of the lithosphere using inverse spectral methods: the state of the art. *Tectonophysics* 631, 87–116.
- Klokočnik, J., Gooding, R.H., Wagner, C.A., Kostecky, J., A. Bezděk J., 2013. The use of Resonant Orbits in Satellite Geodesy: A Review. *Surv. Geophys.* 34 (1), 43–72.
- Koop, R., 1993. *Global Gravity Field Modelling Using Satellite Gravity Gradiometry*. Netherlands Geodetic Commission. Report No. 38.
- Kornfeld, R.P., Arnold, B.W., Gross, M.A., Dahya, N.T., Klipstein, W.M., Gath, P.F., Bettadpur, S., 2019. GRACE-FO: the gravity recovery and climate experiment follow-on mission. *J. Spacecr. Rocket.* 56 (3).
- Krarup, T., 1969. A contribution to the mathematical foundation of physical geodesy. Publ. No. 44. Danish Geodetic Institute, Copenhagen.
- Kryński, J., 1979. Improvement of the geoid in local areas by satellite-to-satellite tracking. *Bull. Géod.* 53, 19–36. <https://doi.org/10.1007/BF02521636>.
- Kryński, J., Schwarz, K.-P., 1977. Application of satellite gradiometry measurements to local geoid determination. *Geodezja Kartografia* 26 (2), 87–10.
- Kusche, J., Schmidt, R., Petrovic, S., Rietbroek, R., 2009. Decorrelated GRACE Time-Varyable Gravity Solutions by GFZ, and their Validation using a Hydrological Model. *J. Geod.* 83, 903–913. <https://doi.org/10.1007/s00190-009-0308-3>.
- Lambeck, K., 1988. *Geophysical Geodesy: The Slow Deformation of the Earth*. Oxford Science Publication.
- Larson, K.M., van Dam, T., 2000. Measuring postglacial rebound with GPS and absolute gravity. *Geophys. Res. Lett.* 27 (23), 3925–3928. <https://doi.org/10.1029/2000GL011946>.
- Laske, G., Masters, G., Ma, Z., Pasyanos, M., 2013. Update on CRUST1.0 – A 1-degree global model of Earth's crust. In: *Geophysical Research Abstracts* (Vol. 15, No. 15, p. 2658). EGU General Assembly 2013, Vienna, Austria.
- Lavallée, D.A., Van Dam, T., Blewitt, G., Clarke, P.J., 2006. Geocenter motions from GPS: A unified observation model. *J. Geophys. Res. Solid Earth* 111 (B5).
- Liu, H.S., 1978. Mantle convection pattern and subcrustal stress field under Asia. *Phys. Earth Planet. Inter.* 16 (3), 247–256.
- Liu, H.S., 1983. A dynamical basis for crustal deformation and seismotectonic block movements in Central Europe. *Phys. Earth Planet. Inter.* 32, 146–159.
- Liu, Q., Schmidt, M., Sanchez, L., Willberg, M., 2020. Regional gravity field refinement for (quasi-) geoid determination based on spherical radial basis functions in Colorado. *J. Geod.* 94, 99.
- Marchenkov, A., Schwintzer, P., 2003. Estimation of the Earth's tensor of inertia from recent global gravity field solutions. *J. Geod.* 76, 495–509. <https://doi.org/10.1007/s00190-002-0280-7>.
- Marsh, B.D., Marsh, J.G., 1976. On global gravity anomalies and two-scale mantle convection. *J. Geophys. Res.* 81 (29), 5267–5280.
- Martinez, Z., 2003. Green's function solution to spherical gradiometric boundary-value problems. *J. Geod.* 77, 41–49.
- Massotti, L., Siemes, C., March, G., Haagmans, R., Silvestrin, P., 2021. Next generation gravity mission elements of the mass change and geoscience international constellation: from orbit selection to instrument and mission design. *Remote Sens.* 13 (19), 3935. <https://doi.org/10.3390/rs13193935>.
- Mathews, P.M., 2000. Improved models for precession and nutation. In: Johnston, K.J., DD, McCarthy, Luzum, B.J., Kaplan, G.H. (Eds.), *Towards Models and constants for Sub-Microarcsecond Astronomy*. Proc IAU Colloquium 180. U.S. Naval Observatory Special Publications, USNO Washington, pp. 212–222.
- McCaffrey, R., Nabelek, J., 1987. Earthquakes, gravity, and the origin of the Bali Basin: an example of a Nascent Continental Fold-and-Thrust Belt. *J. Geophys. Res. Solid Earth* 92 (B1), 441–455. <https://doi.org/10.1029/JB092iB01p00441>.
- McGovern, P.J., Solomon, S.C., Smith, D.E., Zuber, M.T., Simons, M., Wiecezorek, M.A., Phillips, R.J., Neumann, G.A., Aharonson, O., 2002. Localized gravity/topography admittance and correlation spectra on Mars: Implications for regional and global evolution. *J. Geophys. Res.* 107 (E-12), 5136.
- McKenzie, D.P., 1967. Some remarks on heat flow and gravity anomalies. *J. Geophys. Res.* 72 (24), 6261–6273.
- McKenzie, D., 2003. Estimating  $T_e$  in the presence of internal loads. *J. Geophys. Res.* 108 (B), 2438. <https://doi.org/10.1029/2002JB001766>.
- McKenzie, D., 2010. The influence of dynamically supported topography on estimates of  $T_e$ . *Earth Planet. Sci. Lett.* 295, 127–138.

- McKenzie, D., Fairhead, D., 1997. Estimates of the effective elastic thickness of the continental lithosphere from Bouguer and free air gravity anomalies. *J. Geophys. Res.* 102 (B12), 27523–27552.
- McNutt, M., 1980. Implication of regional gravity for state of stress in the Earth's crust and upper mantle. *J. Geophys. Res.* 85 (B11), 6377–6396. <https://doi.org/10.1029/JB085iB11p06377>.
- Medvedev, S., 2016. Understanding lithospheric stresses: systematic analysis of controlling mechanisms with applications to the African Plate. *Geophys. J. Int.* 207 (1), 393–413.
- Molodensky, M.S., Eremeev, V.G., Yurkina, M.I., 1962. Methods for Study of the External Gravitational Field and figure of the Earth. Israel Program for Scientific Translations (Translation from Russian), Jerusalem, Israel.
- Moritz, H., 1980a. Advanced Physical Geodesy. Herbert Wichmann Verlag, Karlsruhe.
- Moritz, H., 1980b. Geodetic reference system 1980. *Bull. Géod.* 54 (3).
- Moritz, H., 1990. The Figure of the Earth. H. Wichmann.
- Morrow, R., Fu, L.L., Arduhin, F., Benkiran, M., Chapron, B., Cosme, E., d'Ovidio, F., Farrar, J.T., Gille, S.T., Lapeyre, G., Le Traon, P.-Y., Pascual, A., Ponte, A., Qiu, B., Rascle, N., Ubelmann, C., Wang, J., Zaron, E.D., 2019. Global observations of fine-scale ocean surface topography with the Surface Water and Ocean Topography (SWOT) Mission. *Front. Mar. Sci.* 6 <https://doi.org/10.3389/fmars.2019.00232>. Article 232.
- Moulton, F.R., 1914. An Introduction to Celestial Mechanics. Dover Publications Inc., New York.
- Mound, J.E., Buffett, B.A., 2006. Detection of a gravitational oscillation in length-of-day. *Earth Planet. Sci. Lett.* <https://doi.org/10.1016/j.epsl.2006.01.043>.
- National Geophysical Data Center, 1993. 5-minute Gridded Global Relief Data (ETOPO5). National Geophysical Data Center, NOAA. <https://doi.org/10.7289/V5D798BF>.
- Oldenburg, D.W., 1974. The inversion and interpretation of gravity anomalies. *Geophysics* 39, 526–536.
- Pail, R., Bingham, R., Braitenberg, C., et al., 2015. Science and user needs for observing global mass transport to understand global change and to benefit society. *Surv. Geophys.* 36 (6), 743–772.
- Pail, R., Bamber, J., Biancale, R., et al., 2019. Mass variation observing system by high low inter-satellite links (MOBILE) – a new concept for sustained observation of mass transport from space. *J. Geod. Sci.* 9 (1), 48–58.
- Panet, I., Flury, J., Biancale, R., et al., 2012. Earth system mass transport mission (e. motion): a concept for future earth gravity field measurements from space. *Surv. Geophys.* 34 (2), 141–163.
- Panet, S., Mikhailov, V., Diamant, M., Pollitz, F., King, G., De Viron, O., Holschneider, M., Biancale, R., Lemoine, J.M., 2007. Coseismic and post-seismic signatures of the Sumatra 2004 December and 2005 March earthquakes in GRACE satellite gravity. *Geophys. J. Int.* 171 (1), 177–190. <https://doi.org/10.1111/j.1365-246X.2007.03525.x>.
- Parker, R.L., 1972. The rapid calculation of potential anomalies. *Geophys. J. R. Astron. Soc.* 31, 447–455.
- Paulson, A., Zhong, S., Wahr, J., 2007. Inference of mantle viscosity from GRACE and relative sea level data. *Geophys. J. Int.* 171, 497–508. <https://doi.org/10.1111/j.1365-246X.2007.03556.x>.
- Pavlis, N.K., Holmes, S.A., Kenyon, S.C., Factor, J.K., 2012. The development and evaluation of the Earth Gravitational Model 2008 (EGM2008). *J. Geophys. Res. Solid Earth* 117 (B4).
- Pérez-Gussinyé, M., Watts, A.B., 2005. The long term strength of Europe and its implications for plate forming processes. *Nature* 436, 381–384.
- Pérez-Gussinyé, M., Lowry, A.R., Watts, A.B., 2007. Effective elastic thickness of South America and its implications for intracontinental deformation. *Geochim. Geophys. Geosyst.* 8 (5), Q05009. <https://doi.org/10.1029/2006GC001511>.
- Pérez-Gussinyé, M., Swain, C.J., Kirby, J.F., Lowry, A.R., 2009. Spatial variations of the effective elastic thickness ( $T_e$ ) using multitaper spectral estimation and wavelet methods: examples from synthetic data and application to South America. *Geochim. Geophys. Geosyst.* 10 <https://doi.org/10.1029/2008GC002229>. Article Q04005.
- Petit, G., Luzum, B., 2013. The 2010 reference edition of the IERS conventions. In: Reference Frames for Applications in Geosciences. Springer, Berlin Heidelberg, pp. 57–61.
- Pfaffenzeller, N., Pail, R., 2023. Small satellite formations and constellations for observing sub-daily mass changes in the earth system. *Geophys. J. Int.* 234 (3), 1550–1567. <https://doi.org/10.1093/gji/ggad132>.
- Pratt, J.H., 1854. On the attraction of Himalayan mountain and of the elevated regions beyond them, upon the plumb line in India. *Philos. Trans. R. Soc. Lond.* 146, 53–100.
- Qiu, B., Chen, S., 2005. Eddy-Induced Heat Transport in the Subtropical North Pacific from Argo, TMI, and Altimetry Measurements. *J. Phys. Oceanogr.* 35 (4), 458–473. <https://doi.org/10.1175/JPO2696.1>.
- Rapp, R.H., 1998. In: Forsberg, et al. (Eds.), Past and future developments in geopotential modelling, pp. 58–78.
- Razeghi, M., Han, S.C., McClusky, S., Sauber, J., 2019. A joint analysis of GPS displacement and GRACE geopotential data for simultaneous estimation of geocenter motion and gravitational field. *J. Geophys. Res. Solid Earth* 124 (11), 12241–12263.
- Reed, G., 1973. Application of Kinematical Geodesy for Determining the Short Wavelength Components of the Gravity Field by Satellite Gradiometry. Report No. XX. The Ohio State University, Columbus.
- Reguzzoni, M., Sampietro, D., 2012. Moho estimation using GOCE data: a numerical simulation. In: International Association of Geodesy Symposium, vol. 136, pp. 205–214.
- Reguzzoni, M., Sampietro, D., Sanso, F., 2013. Global Moho from the combination of the CRUST2.0 model and GOCE data. *Geophys. J. Int.* 195 (1), 222–237.
- Reigber, C., Balmino, G., Schwintzer, P., et al., 2002. A high-quality global gravity field model from CHAMP GPS tracking data and accelerometry (EIGEN-1S). *Geophys. Res. Lett.* 29, 14.
- Ricard, Y., Fleitout, L., Froidevaux, C., 1984. Geoid heights and lithospheric stresses for a dynamic Earth. *Ann. Geophys.* 2 (3), 267–286.
- Richards, M.A., Hager, B.H., 1984. Geoid anomalies in a dynamic Earth. *J. Geophys. Res.* 89 (B7), 5987–6002.
- Rodell, M., Houser, P.R., Jambor, U., Gottschalk, J., Mitchell, K., Meng, C.J., Arsenault, K., Cosgrove, B., Radakovich, J., Bosilovich, M., Entin, J.K., Walker, J.P., Lohmann, D., Toll, D., 2004. The Global Land Data Assimilation System. *Bull. Am. Meteorol. Soc.* 85, 381–394.
- Root, B.C., Tarasov, L., van der Wal, W., 2015. GRACE gravity observations constrain Weichselian ice thickness in the Barents Sea. *Geophys. Res. Lett.* 42 (8), 2898–2905. <https://doi.org/10.1002/2015GL063769>.
- Rosborough, G.W., 1986. Satellite Orbit Perturbations Due to the Geopotential. Technical Report CRS-86-1. University of Texas Austin.
- Rummel, R., 1980. Geoid Heights, Geoid Height Differences, and Mean Gravity Anomalies from Low-Low Satellite-to-Satellite Tracking – An Error Analysis. Report No. 306. Department of Geodetic Science, Ohio State University, Columbus, USA.
- Rummel, R., 2012. Height modelling using GOCE. *J. Geod. Sci.* 2 (4), 355–362. <https://doi.org/10.2478/v10156-011-0047-2>.
- Rummel, R., Teunissen, P., 1988. Height datum definition, height datum connection and the role of the geodetic boundary value problem. *Bull. Géod.* 62, 477–498.
- Rummel, R., Gruber, T., Ihde, J., Liebsch, G., Rülke, A., Schäfer, U., Sideris, M., Rangelova, E., Woodworth, P., Hughes, C., Gerlach, C., 2014. STSE – GOCE+Height System Unification with GOCE. Report of the ESA project GO-HSU-PL-0016.
- Runcorn, S.K., 1967. Flow in the mantle inferred from the low degree harmonics of the geopotential. *Geophys. J. Int.* 14 (1–4), 375–384.
- Sánchez, L., Cunderlík, R., Dayoub, Mikula, K., Minarechová, Z., Šfma, Z., Vatrt, V., Vojtíšková, M., 2016. A conventional value for the geoid reference potential  $W_0$ . *J. Geod.* 90, 815–835.
- Sari, C., Şalk, M., 2002. Estimation of depth to the metamorphic basement by using gravity data: A case study from the West Anatolia. *Geophys. J. Int.* 148 (1), 72–82.
- Schrama, E.J.O., 1986. A study of a satellite to satellite tracking configuration by application of linear perturbations theory. Report 86.3. In: Mathematical and Physical Geodesy, 7. Department of Geodesy, TU Delft, also published in *Quaterniones Geodesiae*, pp. 101–142, 2.
- Schwarz, C.R., 1970. Gravity field refinement by satellite to satellite Doppler tracking. OSURF Project no. 2514. The Ohio State University, Columbus, USA.
- Seeber, G., 2003. Satellite Geodesy, 2nd ed. Walter de Gruyter, Berlin. 589 pp.
- Shafiei Joud, M.S., Sjöberg, L.E., Bagherbandi, M., 2017. Use of GRACE data to detect the present land uplift rate in Fennoscandia, 209, pp. 909–922, 2.
- Shin, Y.H., Shum, C.K., Braitenberg, C., Lee, S.M., Na, S.H., Choi, K.S., Lim, M., 2015. Moho topography, ranges and folds of Tibet by analysis of global gravity models and GOCE data. *Sci. Rep.* 5 (1), 11681.
- Sideris, M.G., 1995. Fourier geoid determination with irregular data. *J. Geod.* 70 (1), 2–12.
- Sideris, M.G., 2016. The FFT in local gravity field determination. In: Grafarend, E.W. (Ed.), *Encyclopedia of Geodesy*. Springer.
- Sjöberg, L.E., 1982. On the recovery of geopotential coefficients using satellite-to-satellite range-rate data on a sphere. *B. Geod.* 56, 27–39.
- Sjöberg, L.E., 1983. Land uplift and its implications on the geoid in Fennoscandia. *Tectonophysics* 97, 97–101.
- Sjöberg, L.E., 1984. Least-Squares modification of Stokes' and Vening-Meinesz formula by accounting for truncation and potential coefficients errors. *Manuscr. Geodaet.* 9, 209–229.
- Sjöberg, L.E., 2009. Solving Vening Meinesz-Moritz inverse problem in isostasy. *Geophys. J. Int.* 179 (3), 1527–1536. <https://doi.org/10.1111/j.1365-246X.2009.04397.x>.
- Sjöberg, L.E., Bagherbandi, M., 2013. A study on the Fennoscandian post-glacial rebound as observed by present-day uplift rates and gravity field model GOCO02S. *Acta Geod. Geophys. Hungarica* 48 (3), 317–331.
- Smith, W.H.F., Sandwell, D.T., 2006. Global sea floor topography from satellite altimetry and ship depth soundings. *Science* 314 (5806), 65–67.
- Soltani, S.S., Ataie-Ashtiani, B., Simmons, C.T., 2021. Review of assimilating GRACE terrestrial water storage data into hydrological models: advances, challenges and opportunities. *Earth Sci. Rev.* 213, 103487.
- Somodi, B., Földvary, L., 2011. Application of numerical integration techniques for orbit determination of state-of-the-art LEO satellites. *Per. Pol. Civil Eng.* 55 (2), 99–106.
- Souchay, J., Kinoshita, H., 1996. Corrections and new developments in rigid earth nutation, I. Lunisolar influence including indirect planetary effects. *Astron. Astrophys.* 312, 1017–1030.
- Steinberger, B., Schmeling, H., Marquart, G., 2001. Large-scale lithospheric stress field and topography induced by global mantle circulation. *Earth Planet. Sci. Lett.* 186 (1), 75–91.
- Stewart, J., Watts, A.B., 1997. Gravity anomalies and spatial variations of flexural rigidity at mountain ranges. *J. Geophys. Res.* 102 (B3), 5327–5352.
- Stokes, G.G., 1849. On the variation of gravity at the surface of the Earth. *Trans. Camb. Phil. Soc. Math. Phys. Sci.* 8, 672.
- Sünkel, H., 1985. An Isostatic Earth Model. Report 367. Department of Geodetic Science and Surveying, Ohio State University, Columbus, Ohio.
- Swain, C.J., Kirby, J.F., 2003a. The effect of noise on estimates of effective elastic thickness of the continental lithosphere by the coherence method. *Geophys. Res. Lett.* 30 (11), 1574.

- Swain, C.J., Kirby, J.F., 2003b. An effective elastic thickness map of Australia from wavelet transforms of gravity and topography using Forsyth's method. *Geophys. Res. Lett.* 30, L02314.
- Swenson, S., Chambers, D., Wahr, J., 2008. Estimating geocenter variations from a combination of GRACE and ocean model output. *J. Geophys. Res. Solid Earth* 113 (B8).
- Tapley, B.D., Bettadpur, S., Watkins, M., Reigber, C., 2004. The gravity recovery and climate experiment: mission overview and early results. *Geophys. Res. Lett.* 31, 1–4.
- Tassara, A., 2005. Interaction between the Nazca and South American plates and formation of the Altiplano-Puna plateau: review of a flexural analysis along the Andean margin (15°–34° S). *Tectonophysics* 399, 39–57.
- Tassara, A., Swain, C., Hackney, R., Kirby, J., 2007. Elastic thickness structure of South America estimated using wavelets and satellite-derived gravity data. *Earth Planet. Sci. Lett.* 253, 17–36.
- Tesaro, M., Kaban, M.K., Clotting, S.A.P.L., 2013. Global model for the lithospheric strength and effective elastic thickness. *Tectonophysics* 602, 78–86.
- Torge, W., Müller, J., Pail, R., 2023. *Geodesy*, 5th edition. De Gruyter Oldenbourg (ISBN 978-3-11-072329-8).
- Tozer, B., Sandwell, D., Smith, W.H.F., Wessel, P., 2019. Global bathymetry and topography at 15 arc seconds: SRTM15+. *Earth Space Sci.* 6 (10), 1847–1864.
- Tscherning, C.C., Rapp, R.H., 1974. Closed Covariance Expressions for Gravity Anomalies, Geoid Undulations, and Deflections of the Vertical Implied by Anomaly Degree Variance Models. Scientific Interim Report Ohio State Univ.
- Vaníček, P., 1976. *Physical Geodesy*. In: Lecture Notes 43. University of New Brunswick, Canada. LN43.pdf (unb.ca).
- Vaníček, P., Martinec, Z., 1994. Stokes-Helmert scheme for the evaluation of a precise geoid. *Manusc. Geodaet.* 19, 119–128.
- Varga, M., Pitoňák, M., Novák, P., Basic, T., 2021. Contribution of GRAV-D airborne gravity to improvement of regional gravimetric geoid modelling in Colorado, USA. *J. Geod.* 95, 53.
- Velicogna, I., Wahr, J., 2002. Postglacial rebound and Earth's viscosity structure from GRACE. *J. Geophys. Res. Solid Earth* 107 (B12). <https://doi.org/10.1029/2001JB001735>. ETG 17-1-ETG 17-12.
- Vening Meinesz, F.A., 1931. Une nouvelle methode pour la reduction isostatique regionale de "intensite de la pesanteur". *Bull. Géod.* 29 (1), 33–51.
- Vermeer, M., 2020. *Physical Geodesy*. Aalto University Press.
- Vestøl, O., Ågren, J., Steffen, H., Kierulf, H., Tarasov, L., 2019. NKG2016LU: a new land uplift model for Fennoscandia and the Baltic Region. *J. Geod.* 93, 1759–1779.
- Visser, P.N.A.M., 1992. *The Use of Satellites in Gravity Field Determination and Adjustment*. PhD Dissertation. Delft University Press, Delft, Netherlands.
- Wahr, J., Molenaar, M., Bryan, F., 1998. Time variability of the Earth's gravity field: Hydrological and oceanic effects and their possible detection using GRACE. *J. Geophys. Res.* 103, 30,229–32,205.
- Walter, H.J., Sandwell, D.T., 1994. Flexural isostatic compensation and the origin of the free-air gravity anomaly over the ocean. *J. Geophys. Res. Solid Earth* 99 (B6), 11409–11427.
- Wang, Y.M., Huang, J., Jiang, T., Sideris, M.G., 2016. Local Geoid Determination. In: Grafarend, E.W. (Ed.), *Encyclopedia of Geodesy*. Springer.
- Wang, Y.M., et al., 2021. Colorado geoid computation experiment: overview and summary. *J. Geod.* 95, 127.
- Werth, S., Güntner, A., Petrovic, S., Schmidt, R., 2009. Integration of GRACE mass variations into a global hydrological model. *Earth Planet. Sci. Lett.* 277 (1–2), 166–173.
- Wessel, P., Smith, W.H.F., 1998. New, improved version of Generic Mapping Tools released. *Eos Trans. AGU* 79 (47), 579.
- Wiese, D., Nerem, R., Lemoine, F., 2012. Design considerations for a dedicated gravity recovery satellite mission consisting of two pairs of satellites. *J. Geodyn.* 86, 81–98.
- Wood, R., Woodward, D., 2002a. Sediment thickness and crustal structure of offshore western New Zealand from 3D gravity modelling. *Explor. Geophys.* 31 (2), 243–255. <https://doi.org/10.1080/00288306.2002.9514971>.
- Wood, R., Woodward, J., 2002b. Satellite gravity modelling of basement structure and Moho depth west of New Zealand. *J. Geophys. Res. Solid Earth* 107 (B8). ETG 1-1-ETG 1-15.
- Woodward, J., Wood, R., 2000. Simultaneous inversion of satellite gravity data for water, sediment, and crustal thickness variations in frontier basins. *Geophys. J. Int.* 142 (1), 1–16.
- Wu, B., Pen, B., Xu, H., 1999. Determination of geocenter variations. *Chin. Sci. Bull.* 44, 1517–1519.
- Wu, X., Ray, J., van Dam, T., 2012. Geocenter motion and its geodetic and geophysical implications. *J. Geodyn.* 58, 44–61.
- Wu, X., Kusche, J., Landerer, F.W., 2017. A new unified approach to determine geocentre motion using space geodetic and GRACE gravity data. *Geophys. J. Int.* 209 (3), 1398–1402.
- Xu, C., Sun, W., Chao, B.F., 2014. Formulation of coseismic changes in Earth rotation and low-degree gravity field based on the spherical Earth dislocation theory. *J. Geophys. Res. Solid Earth* 119 (12), 9031–9041.
- Zamani, J., Samiee, J.F., Kirby, J.F., 2014. The effective elastic thickness of the lithosphere in the collision zone between Arabia and Eurasia in Iran. *J. Geodyn.* 81, 30–40.
- Zhang, W., Shen, W., 2020. New estimation of triaxial three-layered Earth's inertia tensor and solutions of Earth rotation normal modes. *Geodesy. Geodyn.* 11 (5), 307–315. <https://doi.org/10.1016/j.geog.2020.03.005>.